Department of Human Biology
Division of Biomedical Engineering

DEVELOPMENT OF A DEVICE FOR MULTI-MODAL MECHANICAL MANIPULATION OF CELLS IN 2D AND 3D ENGINEERING ENVIRONMENTS

DISSERTATION

submitted to

THE UNIVERSITY OF CAPE TOWN

in fulfilment of the requirements for the degree of

MASTER OF SCIENCE IN BIOMEDICAL ENGINEERING

AUTHOR:

Jerry Sam

SUPERVISOR:

Prof Thomas Franz

Plagiarism Declaration

I, Jerry Sam, hereby declare that the work on which this dissertation is based is my original work (except where acknowledgements indicate otherwise) and that neither the whole work nor any part of it has been, is being, or is to be submitted for another degree in this or any other university.

I empower the university to reproduce for the purpose of research either the whole or any portion of the contents in any manner whatsoever.

Signature: Signed by candidate

Date: 31 January 2018

Abstract

All organisms from bacteria to cells within the human body experience some form of mechanical stimuli. The biochemical response from mechanical stimuli is known as mechanotransduction. Cell manipulation devices provide an understanding of mechanotransduction and the various signalling mechanisms that take place.

The objective of this Master's thesis was to develop a device for multi-modal mechanical manipulation of cells in 2D and 3D environments. The device is to mimic the stress conditions or the mechanical environment of the cells *in vitro*. The mechanical cell loading device will be used to perform cellular mechanical experiments to assist in other future biophysical research and investigate the mechanics of cells under various degrees of tension, compression and shear so that a better understanding of mechanotransduction can be obtained. Cells are seeded in a biocompatible medium and their force response is observed. The incorporation of tension, compression and shear stress in a single device constitutes the uniqueness of this designed device.

A cell manipulator device was designed and assembled with different modular attachments for the various kinds of stress loading. The dimensions of the device were selected in a manner to enable the device to be mountable on a microscope for live cell imaging. The Carl Zeiss LSM510 Confocal Microscope was the microscope available for the experimentation.

In this project, live cell imaging is only possible with tensile strain. Thus, the tension system was the predominant focus. Live cell imaging during tension provides accurate information about cellular morphology. Three different types of PDMS membranes were designed, manufactured and tested by applying a tensile load from the designed device. The three types of PDMS membranes produced were: 20 mm x 20 mm, 20 mm x 20 mm with 1mm thickness dividers (dividers divided the PDMS membrane into 4 even sized quadrants), and 10 mm x 10 mm.

Strain characterisation of the three types of PDMS membrane was performed. The PDMS membranes are marked with ink from a permanent marker which serves as a frame of reference for strain measurement. Using the permanent marker, dots were marked in grid format. The PDMS membranes were subjected to tensile stress from the designed device under a confocal microscope. Length deformation of the markers along the stretch axis was measured and recorded during the practical experimentation.

Using FEA software, FEA models of each type of PDMS membrane was simulated. The purpose of the FEA models is to facilitate the future studies of researchers. FEA simulations provide feedback to guide actual cellular experimentation for researchers. The FEA models of the various types of PDMS membranes were validated against the practical experimentation of strain characterisation.

From the analysis and discussion of the results of FEA and practical experimentation, the designed device satisfies the objectives of this project. The device was most successful with the 20 mm x 20 mm PDMS membrane type since it showed close correlation to the ideal strain output. FEA simulation of the 20 mm x 20 mm PDMS membrane also showed close correlation to the experimental results. But, in the instance of the 10 mm x 10 mm PDMS membrane, experimental results of the strain output did not correspond with the user strain due to the clamping mechanism unable to grapple PDMS membrane appropriately. Thus, validation of the FEA 10 mm x 10 mm PDMS membrane was not successful.

Acknowledgements

Thank you to the National Research Foundation (NRF) of South Africa for funding this research. It was truly a well spent period time of my life at the University of Cape Town; making possible the remarkable experiences and enfolding more opportunities in my life journey.

Thank you to Professor Thomas Franz, for your supervision and feedback on this project. This work would not have been possible without your input and expertise. I am truly grateful for the opportunity to have you as a supervisor, for steering this project into the right direction and helping me to develop my presentation skills.

Thank you to my parents, Tim Sam and Shu-Mei Sam for their everlasting love, support and sacrifices to enable the opportunities for me to learn, build and grow. I am truly grateful for my best friend and my partner in crime, Ai-Ting Wong for her words of encouragement and for proof-reading and editing this document. A great appreciation goes to Nicholas Skeen for his invaluable input and suggestions for this project. Thank you for being a true friend throughout all the years.

Much appreciation goes to Susan Cooper, Dirk Lang and Carla van Niekerk from the Microscope Imaging Facility, for having the patience to facilitate me through the long hours of imaging. The help of manufacturing of the components for the device from the UCT Mechanical Engineering Workshop is greatly appreciated. Thank you to Pierre Smith for taking the time and effort to help me, despite your busy schedule.

My gratuity extends to the peers I have met and friends I have made, who are part of the biomedical engineering journey. I truly wish you all the best with the future endeavours. Good luck to you all.

Contents

List of Tables

List of Figures

List of Abbreviations

PDMS – Polydimethylsiloxane
CSK – Cytoskeleton
BAECs – Bovine Aortic Endothelial Cells
AFM – Atomic Force Microscopy
BMSCs – Bone-marrow Mesenchymal Stem Cells
LSM – Laser Scanning Microscope
3D – 3 Dimensional
2D – 2 Dimensional
ABS plastic – Acrylonitrile Butadiene Styrene plastic
CAD – Computer Aided Design
FEA – Finite Element Analysis
UTM – Universal Testing Machine

1 Background to Study

1.1 Introduction

1.1.1 Purpose of Study

The purpose of the research was to develop a unique mechanical cell loading device for the University of Cape Town Cell and Tissue Mechanobiology Laboratory to perform cellular mechanical experiments. This study was aimed to develop a low-cost device which provides 2D uniaxial stretch, compressing and shearing of cells in a 3D environment. This outcome of the project will assist in other research to investigate the mechanics of cells and matrix samples such as polydimethylsiloxane (PDMS) and various types of hydrogel under various degrees of tension, compression and shear. Along with the design and manufacturing of the device; strain and stress characterisation of the PDMS tension substrates were investigated.

1.1.2 Importance of Study

All organisms from bacteria to cellular organisms within the human body experience some form of mechanical stimuli. Through recent studies in Mechanobiology, external forces are increasingly recognised to be a major influence on cellular structure and function. What is largely undetermined is the fundamental reactions of cells to sense different forces and transduce these forces into biochemical signals and other behavioural responses (Mann et al. 2012).

Being able to mimic the local mechanical forces of the cellular environment leads to a better understanding of the fundamental cellular mechanisms and creates prospects for tissues engineering and advancements in drug development. In the study of Khanafer et al. (2009), mechanical properties of PDMS substrates are investigated to help design *in vitro* experiments of arterial walls to understand the complex interaction with blood flow.

1.1.3 Research Approach

The project includes design and testing aspects. The design aspect was more predominant and involves the iteration of CAD design on Solidworks® before manufacturing at the UCT Mechanical Engineering Workshop. The testing component of the mechanical cell loading device characterises the strain fields on the PDMS tension samples. Tension membrane samples were marked with ink stains and subsequently stretched under a confocal microscope to acquire live imaging of the strain performed.

Investigations of the stress-strain curve through experimentation and computational modelling of PDMS membranes using Abaqus® were additionally conducted. The strain characteristics from the practical experimentation of the device on the various PDMS membranes were compared with the computational model. This comparison was conducted to validate the FEA models of the various types of designed PDMS membranes.

1.1.4 Dissertation Overview

This document entails the research, design and testing methodologies, discussion of the results, and further recommendations of the dissertation project. Chapter 1 further provides an overall and an understanding of the importance of the study, the different cell mechanical manipulation devices currently available, gel substrates where cells are seeded, and different imaging techniques used for cellular imaging. Chapter 2 discusses the method of approach to the design and experimentation. The

results are presented and discussed in Chapter 3. In the final chapter, Chapter 4, concluding remarks are drawn and further recommendations for the mechanical cell manipulator device are discussed.

1.2 Cell Mechanics

Animal cells, in general, contain a cytoplasm, nucleus, and cytoskeleton which are surrounded by the cell membrane. The cytosol is the suspension fluid within the cell membrane which binds the cell organelles together. The network of filamentous proteins, which include microtubules, intermediate filaments, actin filaments and other cellular proteins contained within the cytoplasm form a structural framework known as the cytoskeleton (Unal et al. 2014). The cytoskeleton (CSK) provides the cell with its shape and motility.

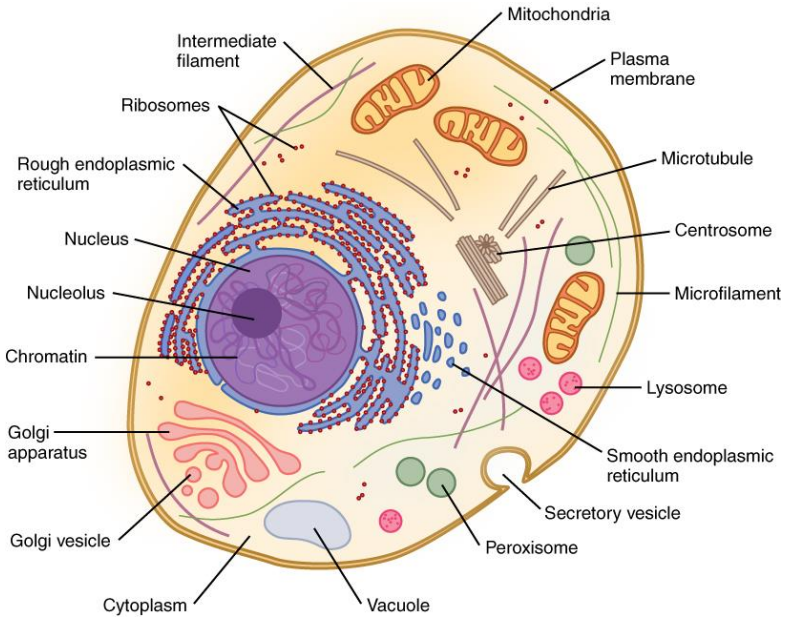

Figure 1: A generalized human cell showing the principal organelles (from Surekha (2016))

Mechanical stresses such as tension, compression and shear play a pivotal role in cell physiology. Metabolically active cells are always subject to various kinds of mechanical stimuli in diverse environments. External forces are increasingly recognised to be major contributors of regulators to cell structure and function (Janmey and McCulloch 2007). From mechanical stimuli, cells can either stiffen their cytoskeleton to create a stronger surface adhesion or reduce the structural stiffness and become more fluid-like in response to changes from its surrounding environment (Krishnan et al. 2009).

The system of biochemical response from mechanical stimuli is known as mechanotransduction (Shao et al. 2013). Cell stretcher devices and suitable methods of cell imaging *in vitro* can provide an understanding of the investigation of mechanotransduction and the various signalling mechanisms that take place. Cells generally respond to mechanical stimuli in two different ways: physical response and biochemical response (Unal et al. 2014).

The physical response includes the reshaping of the cell and realignment of the cytoskeleton on anisotropic surfaces (Bausch and Kroy 2006). In a study conducted by Naruse et al. (1998), endothelial cells from the human umbilical cord were stretched to determine the role of calcium and the orientating response of stretch-activated channels. Morphological changes were observed when the cells were subject to a sinusoidal cyclic stretch of 20% at 1Hz. The cells began to orient perpendicularly to the stretch axis 15 minutes after the onset of the stimulus. After 120 minutes of stretch, 90% of

endothelial cells aligned almost perpendicular to the stretch axis. This change in orientation suggests the reorganization of cytoskeletal structures of the cells (Naruse et al. 1998).

In Figure 2, the phase contrast of the cells in response to the cyclic stretch is shown. Image A shows cultured endothelial cells without any external forces applied and have no specific orientation. Image B shows cells stretched after 30 minutes, Image C shows cells stretched after 60 minutes and Image D shows cells stretched after 120 minutes (Naruse et al. 1998). The transition from Image A to D shows the perpendicular rearrangement of the cells.

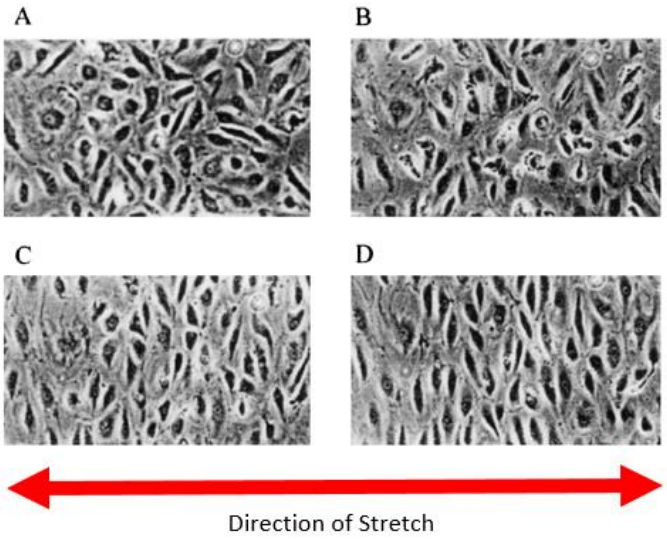

Figure 2: Stretch-induced morphological changes of endothelial cells (image adapted from Naruse et al. (1998))

A biochemical response includes the activation of intercellular or extracellular signalling cascades (Chien 2007). For example, a study conducted by Takeda et al. (2006), investigated the intercellular signalling mechanism of stretch-induced nitric oxide production in bovine arterial endothelial cells (BAECs) as seen in Figure 3. The BAECs were subject to a uniaxial cyclic stretch of 20% at 1 Hz. Nitric oxide production was noticed to increase, with peaks at 5 minutes and 20 minutes of stretching. Takeda et al. (2006) suggested that the early peak was mediated by Ca^{2+} influx and the 20^{th} minute peak was due to the activation of Akt. Akt, also known as protein kinase B (PKB) is responsible for many cellular processes, such as glucose metabolism and cell proliferation and migration (Brazil and Hemmings 2001).

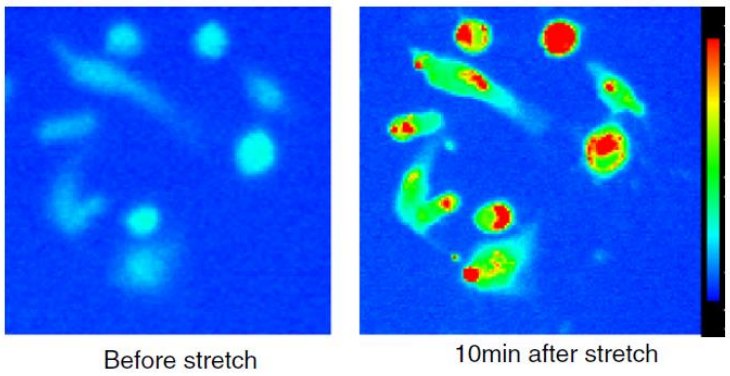

Figure 3: Nitric oxide measured with fluorescent reagent DAF-2 (with permission from Takeda et al. (2006))

These physical and biochemical responses may lead to many cellular events, such as the stiffening, softening, maturation, calcium influx, morphological changes, generation of traction forces or focal adhesions. These events can be further applied to clinical practices, such as in various disease processes, including cancer, osteoporosis, osteoarthritis, asthma and malaria (Unal et al. 2014).

Currently, the devices used to elicit these responses on the cell can be differentiated between active and passive. Active cell mechanics refers to the cell being manipulated by a loading device, such as a cell stretcher device that loads tension onto a cell to stretch its structure. Passive cell mechanics refers to the cell acting upon a device. This involves the measuring of forces generated by the cells. An example of a passive cell device is micro-pillars. Micro-pillars essentially act as microscopic force sensors that can be used to measure traction forces (Jacobs et al. 2012).

1.3 Mechanical Manipulation and Cell Loading Approaches

Mechanical manipulation and characterization of biological cells are one of the major topics of research as the fundamental mechanism of cells to sense the external forces and respond to these forces by biochemical behaviours and signals is still largely unknown (Mann et al. 2012). As mentioned above, external forces are increasingly recognised to be a major influence in cell activity. From the physiological functions of various organs of the human body, these cells are continuously subjected to cyclic mechanical strain. Cells have the ability to sense and respond to mechanical stimuli and this process is known as mechanotransduction. Through a better understanding of the workings of cell behaviour, it can help researchers to improve clinical diagnosis and acquire a better understanding of various medical pathologies.

Determining the mechanical properties and behaviour of cells has been studied through a variety of methods. This following section gives a brief overview of the different approaches to cell mechanical manipulation. These approaches include Atomic-force Microscopy (AFM), magnetic tweezers, optical tweezers and cell stretching devices.

1.3.1 Atomic-force Microscopy (AFM)

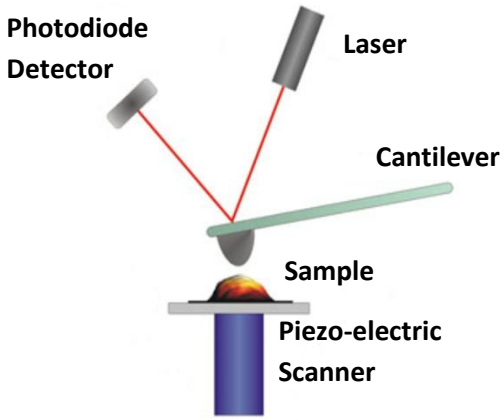

Figure 4: Basic atomic force microscopy diagram (with permission from Roos (2011))

As seen in Figure 4, AFM is a type of scanning probe microscopy. The basic components of an AFM are a cantilever system with a sharp tip attached, a laser and force detector. The sample is controlled and manoeuvred by piezoelectric actuators to the tip of the cantilever. When the sample surface approaches the tip, the force between the tip and sample surface causes a deflection. This deflection is quantified by the use of the laser which measures the beam reflection (Hoh and Hansma 1992). In this imaging modality, the reaction force between probe and surface can be used to formulate height differences forming an image of a three-dimensional shape and can thus be used to measure the mechanical properties of the cell.

In a study conducted by Wu et al. (1998), AFM was used to investigate the cytoskeleton structure of L929 cells. Mechanical properties such as the elasticity, viscoelasticity and plasticity were able to be measured on these cells which outlined the extensive capabilities of AFM (Wu et al. 1998).

1.3.2 Magnetic Tweezers

The basic set up of a magnetic tweezer consist of a pair of permanent magnets placed above the microscope objective and a magnetic bead. A CCD camera is outfitted to observe the biological material. The superparamagnetic bead is coated with the biological entity. By turning on the electromagnet and adjusting the amplitude and phase of the current for the magnet, a specific force can be exerted on the bead. This gives the user the ability to control the exact magnitude and direction of an applied force. The exerted magnetic forces are recorded and used to determine mechanical properties of various biological molecules and chemical bonds. Magnetic tweezers are ideally suited for the study of deoxyribonucleic acid (DNA) topology and topoisomerases (Neuman and Nagy 2008).

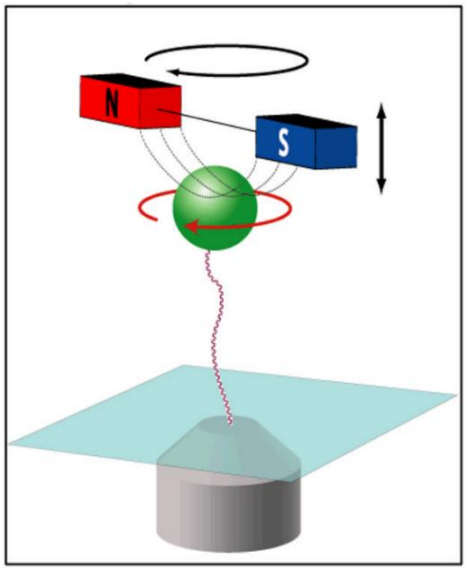

Figure 5: Layout of magnetic tweezers - A superparamagnetic bead (green) is attached to the surface of the trapping chamber by a single molecule of DNA (red and blue) (with permission from Neuman and Nagy (2008))

In Figure 5, a pair of small permanent magnets (red and blue) produces a magnetic field, which results in an upward force on the bead (green). The force is controlled by moving the permanent magnets in an up and down motion, thus rotation of the magnets results in a rotation of the magnetic bead.

1.3.3 Optical Tweezers

Optical tweezers, formally known as *"single-beam gradient force trap"*, use a highly-focused laser-beam to provide an attractive or repulsive force. A laser beam is focused by a high-quality microscope objective lens. The radiation pressure from the focused laser beam is able to trap small particles at its centre. The forces experienced by the particle comprises of the light scattering and gradient forces due to the interaction of the particles with the light.

By focusing a laser to a diffraction-limited point through the microscope objective that has a numerical aperture, the dielectric particles within the vicinity of the focused region are manipulated to experience a three-dimensional restoring force directed toward the focal point (Neuman and Nagy 2008).

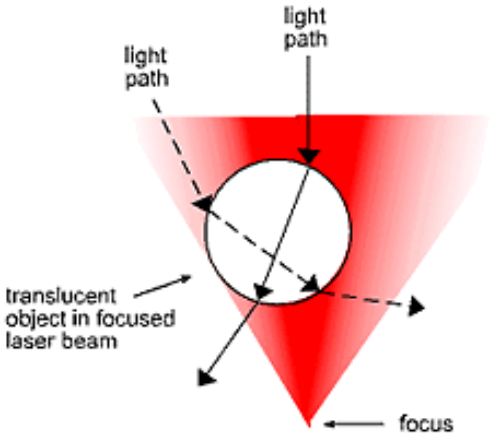

Figure 6: Basic form of an optical trap – trapped sphere (from PhysicsCentral (2016))

Figure 6 depicts two light paths in the optical tweezer laser beam passing through a translucent object. The light path that originates closer to the centre of the beam will have a greater number of photons per second as it is less diffracted. The changes in momentum of the photons of the diffracted light paths give the sphere momentum towards the beam axis and also towards the beam focus (PhysicsCentral 2016).

Optical tweezers have commonly been used in the biological field of study in the recent years. The size of the particle which the optical tweezers can trap ranges from 20 nm to several micrometres, such as organelles and cells (Unal et al. 2014). Forces exerted using optical tweezers are in the order of piconewtons, ranging from 0.1 ρN to 100 ρN (Neuman and Nagy 2008).

1.3.4 Mechanical Cell Loading Devices

Mechanical cell loading devices are active mechanical manipulative devices as they induce external forces onto the cell to simulate mechanical stimuli. From research done, cell mechanical loading devices are predominantly cell stretching devices. Cell stretching devices use some form of actuation method to stretch a membrane, typically made of flexible polydimethylsiloxane (PDMS) substrates, where the cells are cultured on.

Shear stress is typically simulated by establishing a controlled flow of a certain fluid of known mechanical properties and analysing the shear stress applied to the cell monolayer. One often uses laminar flow to expose cells to a controlled shear stress. However, there are numerous studies that involve turbulent flow to mimic vessel wall pathologies and investigate atherosclerosis, a disease of the arteries characterised by the deposition of fatty material on the inner walls. The transition of laminar to turbulent flow is governed by the Reynolds number (Jacobs et al. 2012).

The following section provides more detail of the mechanical cell loading devices, as this type of device is the approach that this project will take.

1.4 Mechanical Cell Loading Devices

There are several commercially available cell stretcher devices such as Flexcell® (Burlington, USA) and STREX Inc. (Osaka, Japan). Additionally, academic research into Cell Mechanobiology has led to the development of custom cell stretcher devices by research groups.

1.4.1 Tension Stress

1.4.1.1 Uniaxial vs. Multiaxial Strain

Cell stretcher devices can be divided into two types: uniaxial stretching and multiaxial stretching. Uniaxial stretching refers to cells stretching in one direction which allows the cells to experience compression in the orthogonal axis. In literature, multiaxial stretching is predominantly biaxial. Biaxial stretching refers to cell stretching in the two axes perpendicular to each other. In biaxial stretching, it is preferred that both axes stretch equally to accommodate for uniform deformability of the substrate matrix.

Uniaxial applied forces have been found to cause changes to the cell cytoskeleton and cell alignment, as seen from the experiments of Naruse et al. (1998). The stretching direction is an important parameter to be considered in designing a cell stretcher device as it determines the reaction that takes place (Kamble et al. 2016). Cells that are placed over the *in vitro* membrane are randomly oriented, the cells are therefore not all aligned in the direction of strain. This results in cells experiencing different types of strain which varies cell behaviour (Tamiello et al. 2016). Ursekar et al. (2014) suggest that to avoid anisotropy and heterogeneity, equibiaxial stretching is preferred.

1.4.1.2 Cyclic Stretching

Through examination of literature and commercial research, cell stretching devices are programmed to offer two types of cyclic stretching modes, sinusoidal and square as illustrated in Figure 7. The sinusoidal stretching is the gradual stretch-release cycle, while the square wave is a sustained full stretch.

Different waveforms have different effects on cells. In a study conducted by Qu and Gao (2010), the effect of square wave stretching on the proliferation of lung adenocarcinoma A549 cells and squamous carcinoma of tongue Tca8113 cells were investigated. The cells were subjected to different types of mechanical strain and the effects were studied. A flow cytometer was adopted to investigate the proliferation index of A549 cells and Tca8113 cells. The experimental results showed that the proliferation index reduced significantly when the cells were subjected to a square wave for 4 hours while there was no difference in proliferation when the cells were subjected to sinusoidal wave treatment compared to the control group. This suggests that waveforms play a pivotal role in inhibiting proliferation of cells (Qu and Gao 2010).

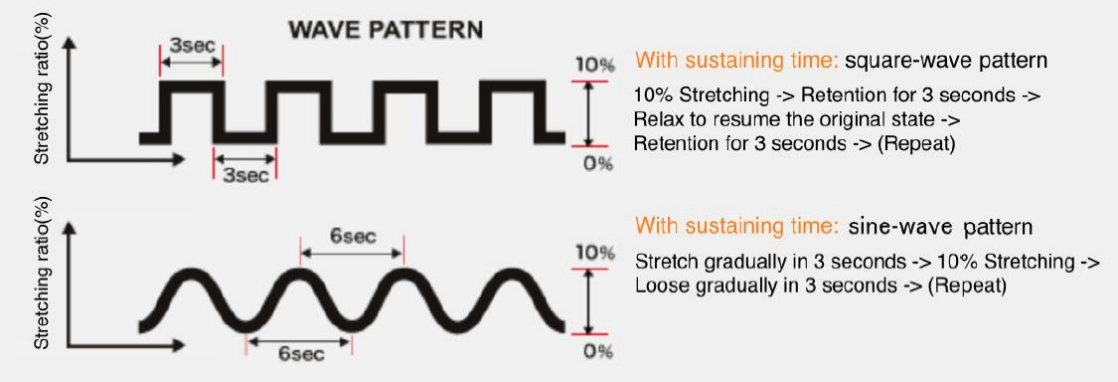

Figure 7: Example of cyclic stretching of 10%, 10 cycles/min (from Strex (2017))

1.4.1.3 Erlangen Cell Stretcher Device

The Erlangen Cell Stretcher Device serves as a baseline model for research based on a collaboration between the UCT Mechanobiology Lab and the research group of Professor Ben Fabry at the Friedrich Alexander University Erlangen-Nuremberg in Germany.

The device provides uniaxial stretch functionality driven by a direct current motor with an integrated gearbox. Displacement amplitudes are preselected and have an amplitude of 20 µm (Faust et al. 2011). The stretcher can be attached to an inverted confocal microscope to observe cell behaviour during the stretching experimentation (Bonakdar et al. 2012).

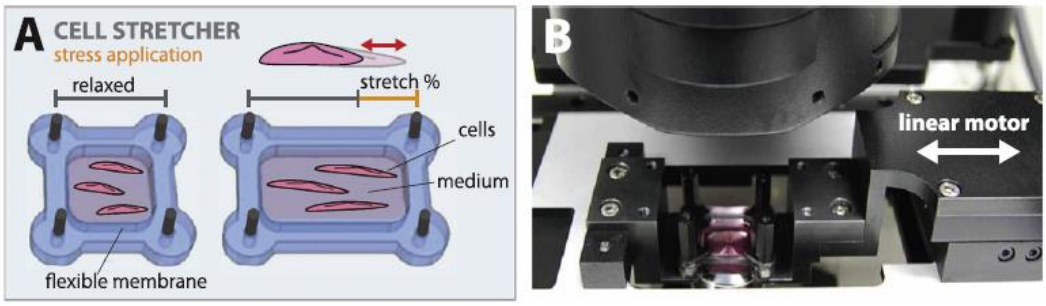

Figure 8: Erlangen Cell Stretcher Device (with permission from Bonakdar et al. (2012)): (A) Cells are plated on an elastomeric PDMS- membrane coated with the extracellular matrix-protein fibronectin. (B) The stretcher is attached to an inverted microscope to observe cell behaviour during the stretch.

1.4.1.4 Tension Actuation Methods

This section discusses the two most prominent methods of tensile actuation from the literature: pneumatic and electromagnetic actuation methods.

1.4.1.4.1 Pneumatic Actuation

This concept is based on the deformation of a thin flexible membrane by controlled actuation pressure. The cells are cultured directly onto the membrane as seen in Figure 9 (Tremblay et al. 2014). Pneumatic actuation methods present many advantages and these include: it is a simple system in to apply homogenous strain actuation and there is a lack of contamination (Kamble et al. 2016).

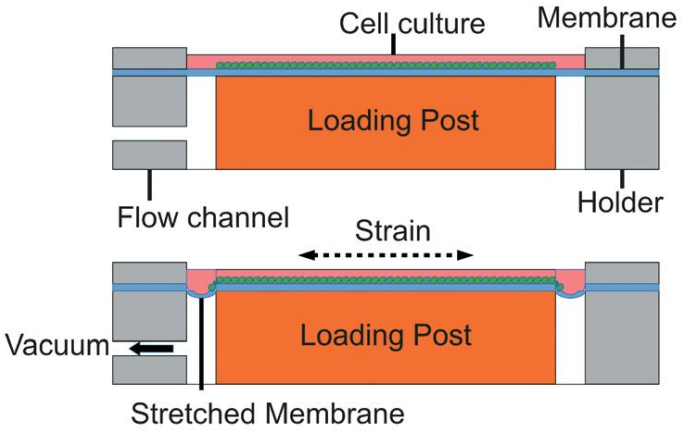

Figure 9: Pneumatic actuation device from Flexcell© (Burlington, USA) applying equibiaxial strain to cells (with permission from Kamble et al. (2016))

1.4.1.4.2 Electromagnetic Actuation

Electromagnetic actuation methods include the use of servos and stepper motors to linearly push and pull as seen in Figure 10. Kamble et al. (2016) discussed that electromagnetic actuation had the greater advantage of high precision and simple setup for various types of mechanical loading. The review does, however, suggest that heating and contamination through motor lubrication are disadvantages of having an electromagnetic actuation system (Kamble et al. 2016). Through careful selection of electromagnetic actuation type and advancement of electromagnetic actuators, these disadvantages can be reduced.

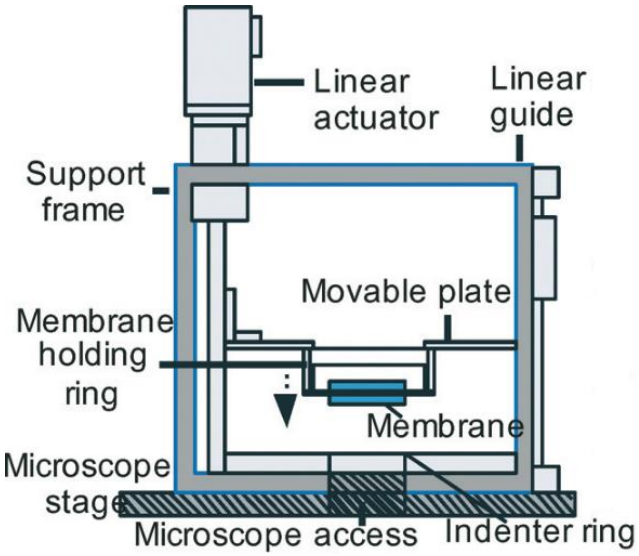

Figure 10: Typical cell stretching device with electromagnetic actuation (with permission from Kamble et al. (2016))

1.4.2 Compression Stress

Through research, compression methods include pressure techniques using a vacuum instrument (Banes et al. 1985), a glass indenter controlled by piezo actuators (Peeters et al. 2003) and a novel axial-stress bioreactor system (Li et al. 2014). These devices are all capable of applying static or variable duration cyclic compression to cells *in vitro* and are also capable of performing experiments in incubators for favourable environmental conditions.

1.4.2.1 Compression Actuation Methods

1.4.2.1.1 Vacuum operated Stress

This method of operation is similar to the method of the pneumatic cell stretcher device as discussed and seen in Figure 9. Banes et al. (1985) uses this pneumatic operation to deform a plastic petri dish which is capable of yielding 0.13% compression to the cells situated on the inner surface of the petri dish. The petri dish deflects 1.5mm from the pressure to produce this compressive yield (Banes et al. 1985).

The stress unit of (Banes et al. 1985) consists of a Perspex container which contains 6 vacuum ports displayed in Figure 11. Rubber seals are lined within each port and are coated with vacuum grease before the petri dishes are places in each port.

On one side of the Perspex container, a metered valve is fitted to measure and apply pressure and the on the other side of the container, a bleed valve is fitted for pressure level adjustment.

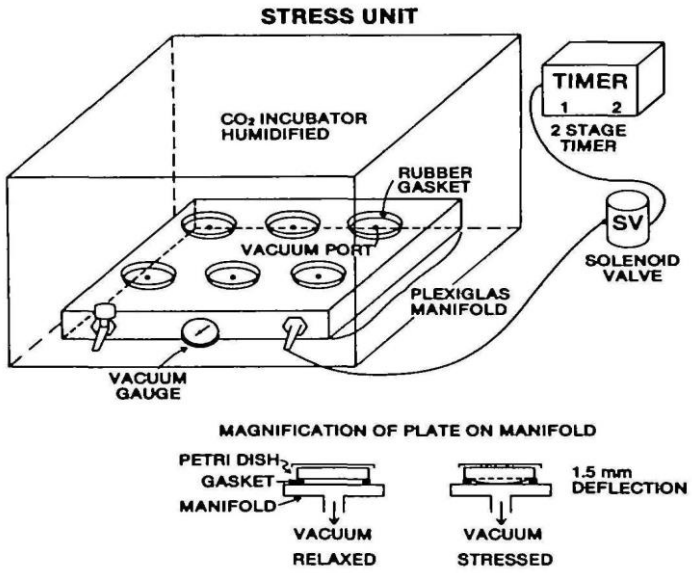

Figure 11: Vacuum stress unit and magnification of the petri dish during a cycle of compression (with permission from Banes et al. (1985))

1.4.2.1.2 Compression using Glass Indenter and Piezo Actuators

A cell loading device developed by Peeters et al. (2003) was used to further investigate the relationship between cell deformation and cell damage. The goal of their study was to develop a device to monitor the biochemical response of skeletal muscle cells to sustained cell deformation to gain an additional understanding of how pressure sores occur clinically on patients. The device is able to compress individual cells, allowing the mechanical properties of the cells to be measured and the cell structure to be simultaneously visualised, during compression (Peeters et al. 2003).

The device consists of a steel frame that mounts onto the stage of an inverted microscope. Cells are cultured on glass coverslips and are inserted into a chamber of the steel frame. Cells are compressed with the glass indenter as shown in Figure 12. The glass indenter has a flat surface with a diameter of 60 µm. A force transducer is connected to the glass indenter, to convert the input of mechanical force into an electrical output signal for mechanical characterisation (Peeters et al. 2003). Piezo actuators are used to position the glass indenter in the x, y and z plane. These actuators are controlled using a motor controller PC board (Peeters et al. 2005).

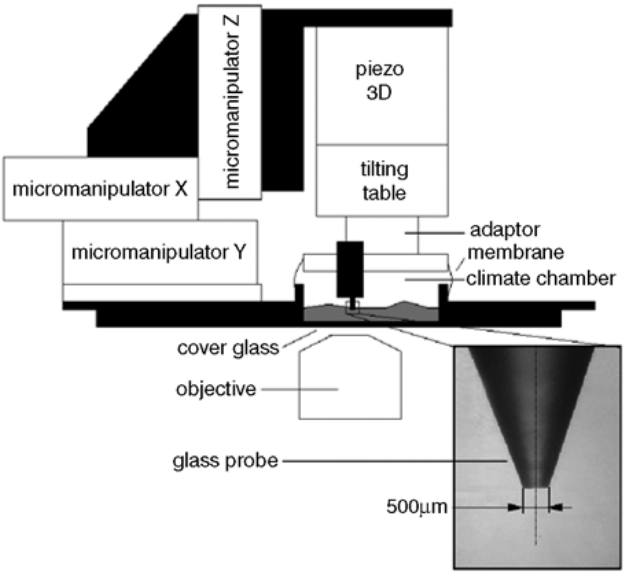

Figure 12: Schematic of cell loading device and close-up of glass probe (with permission from Peeters et al. (2003))

1.4.2.1.3 Novel axial-stress bioreactor system

A study conducted by Li et al. (2014) introduced a prototype of a novel axial-bioreactor system. The main feature of this system is to support the long-term growth of engineered tissues by incorporating substance exchanger and feedback systems of pH and PO_2. A 21-day study was conducted to showcase the system's ability to maintain a stable and sterile environment. The results showed that physiochemical environments remained at stable levels and no bacteria or fungi were detected, thus, demonstrating that the bioreactor system was sterile (Li et al. 2014). The bioreactor system consists of the integrated servomotor, physiochemical circulating system, motor controller unit and other supplementary equipment.

The cell loading unit consists of a linear servomotor to perform compression in the experiment on mouse bone-marrow mesenchymal stem cells (BMSCs) seeded in 3D scaffolds of decalcified bone matrix. A stainless-steel piston is attached to the linear servomotor for position control and force monitoring. The servomotor drives a loading plate to deliver axial compression to the cells seeded in the scaffold (Li et al. 2014).

1.4.3 Shear Stress

1.4.3.1 Parallel-plate flow chamber

As previously discussed, studies about shear stress on cells are typically simulated by fluids flowing over cells in a parallel-plate flow chamber. The use of the of the parallel-plate flow chamber allows for a well-defined and controlled environment. Variables, such as the chamber geometry and flow rate of fluids through the chamber can be explicit and controlled (Konstantopoulos. et al. 1998).

Parallel-plate flow chambers typically consist of a transparent polycarbonate disk, a silicone gasket, and a glass coverslip. The polycarbonate disk forms one side of the parallel-plate flow chamber and includes an inlet port and outlet port. The silicone gasket mates the surfaces of the disk and the glass coverslip, and its thickness determines the flow path depth. A confluent cell monolayer is coated on the glass coverslip. The apparatus is sealed together by vacuum, holding the three respective parts together (Chiu and Chien 2011).

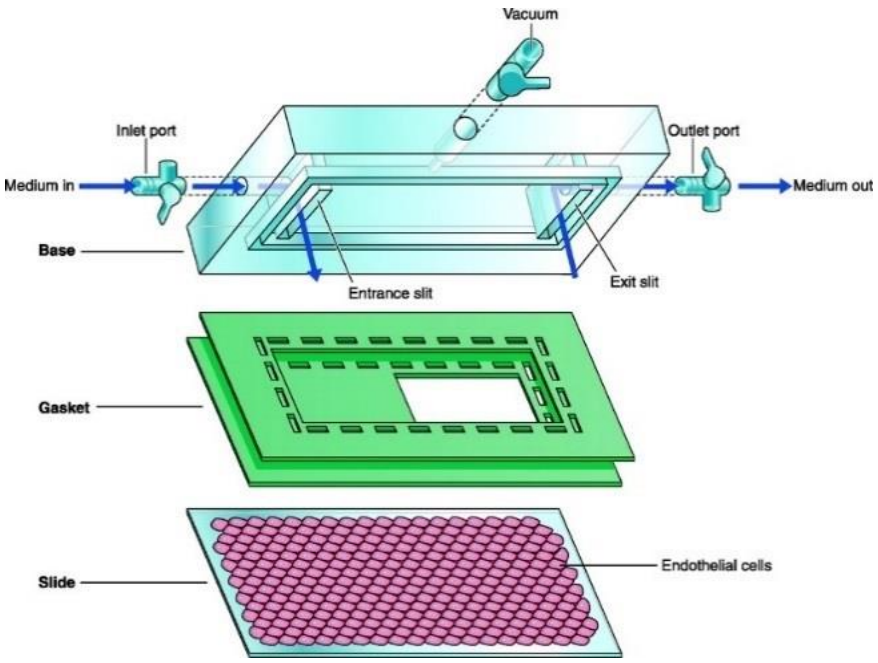

Figure 13: Diagram showing the parallel-plate flow chamber (from Chiu and Chien (2011))

1.4.3.2 Viscometer

The use of a viscometer is another method to simulate mechanical shearing stress conditions. A viscometer is an instrument used to measure the viscosity of a fluid. Cells are placed between the cone and plate as shown in Figure 14. The rotation of the conical plate causes a constant and uniform shear stress on the sample. Viscometers use the notion of determining a required force to rotate the cone in the fluid at a known speed. This determined force is further evaluated to determine the shear stress applied (Rheosys 2011).

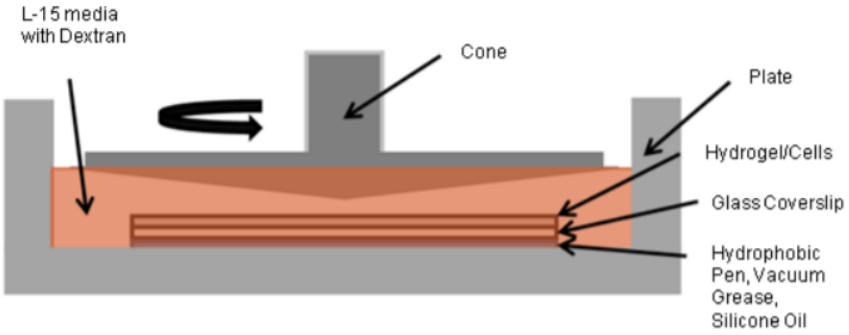

Figure 14: Cone and plate viscometer schematic (with permission from Kohn et al. (2015))

When the particles or cells of its own fluid are falling by its own weight, then the terminal velocity also known as the settling velocity is reached. This is due to the summation of the frictional force and the buoyant force balancing the gravitational force. The settling velocity is given by the following equation:

$$V_s = \frac{2r^2 g(\rho_p - \rho_f)}{9\mu}$$

where:

- V_s is the particle's settling velocity or terminal velocity $[m/s]$
- r is the radius of the particle $[m]$
- g is the gravitational acceleration $[m/s^2]$
- ρ_p is the density of the particles $[kg/s^3]$
- ρ_f is the density of the fluid $[kg/s^3]$
- μ is the fluid viscosity $[Pa.s]$

1.5 Substrates

1.5.1 Polydimethylsiloxane (PDMS)

To perform biological experiments and to study the cell mechanical properties, soft elastic substrates are often used (Brown et al. 2005; Thangawng et al. 2007). Polydimethylsiloxane (PDMS) is often selected as a common elastomer to be used in these cellular mechanic experiments, due to its biocompatibility properties and ease of processing (Sophie L. Peterson et al. 2004). Its mechanical feature of high elasticity offers an advantage over traditional substrate materials such as glass, silicon and other harder polymers. Other advantages include low cost, fast and simple fabrication and optical transparency (Liu et al. 2009; Johnston et al. 2014).

The Young's modulus value of the PDMS can be varied during the processing of it to suit the physiological relevance of the cells under experiment; such as to resemble the elastic modulus of many different types of human tissue. Mechanical properties of the PDMS elastomers as seen from the experiments of Khanafer et al. (2009), may assist in the design of *in vitro* experiments of arterial walls to understand the complex interaction with blood flow.

1.5.1.1 Molecular Structure

Polysiloxane, the polymer base for PDMS, is made of entangled chains of polymer molecules. The long polymeric chains slide across each other acting like a viscous fluid when it has not undergone vulcanization. PDMS is an elastomer (rubber-like material) under the silicone family tree.

PDMS is composed of two parts, DC 184 Base (Polysiloxane, the unprocessed Silicone) and DC 184 Curing Agent. The Curing Agent is a cross-linker or hardening agent. The cross-links are the chemical bonds between the polymer molecules. To produce the strength and durability of the polymer network, the polymer chains must be cross-linked.

1.5.1.2 Processing of PDMS

Vulcanization is the chemical process of converting the polymer network into a more durable material by adding a curing agent. During the processing of PDMS, vulcanization produces cross-links among the polymer chain, which stiffens the molecular network.

The cross-link density in the PDMS network is dependent on the factors such as: the amount of added curing agent, the type of curing process, cure temperature and the curing duration. Research on these variations is widely conducted from the literature to define a mechanical function of PDMS. It is very important that test specimens share the same curing history for adequate results when testing for its mechanical properties.

PDMS is formed by combining a pre-polymer base agent and a cross-linking agent. The ratio of the two agents affects the elastic modulus. The elastic modulus of the cured substrate increases as the mixing ratio of pre-polymer to cross-linking agent increases to 9:1. Subsequently, the elastic modulus decreases as the mixing ratio continues to increase. This mechanical characteristic of the elastomer network of different ratios is shown in Figure 15. Exceeding the ratio of 9:1 softens the nature of the PDMS (Khanafer et al. 2009).

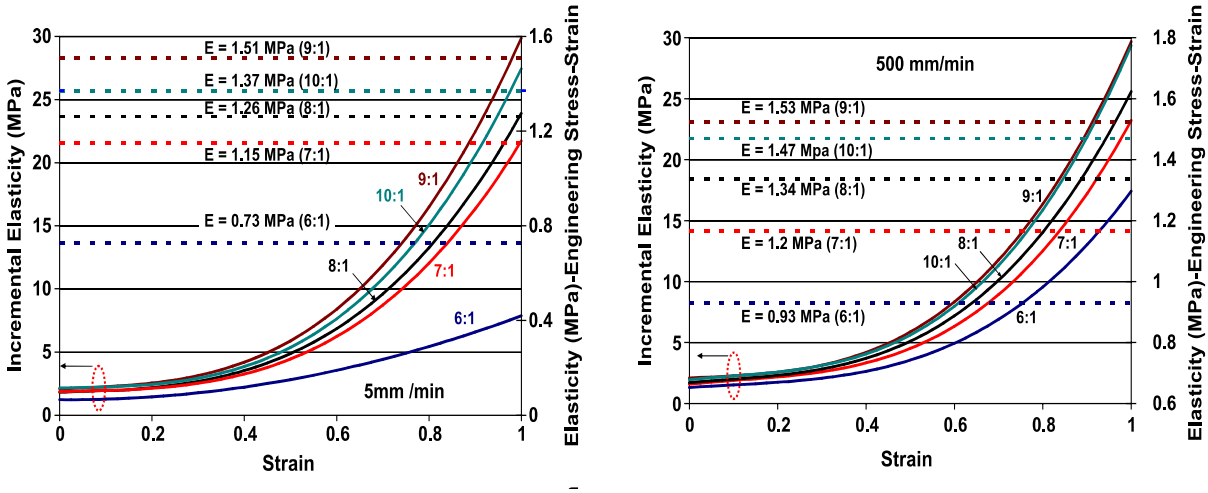

Figure 15: Effect of the mixing ratio on the elastic modulus at different crosshead speeds (with permission from Khanafer et al. (2009))

The mechanical effects on PDMS by varying the curing temperature have been reported from literature. Liu et al. (2009) demonstrated that curing temperature can significantly influence the resulting properties of the substrate. In the experiment of Liu et al. (2009); during their production of the elastomer, sets of samples were heated on a hot plate. The test specimens were grouped into four sets. Each group was cured on a hotplate at 100 °C, 150 °C, 200 °C and 300 °C respectively. After the heating process, the cured PDMS samples left to cool until room temperature, at which was the temperature the mechanical loading tests were performed. The results showed that higher heating temperatures of the mixture on a hotplate produced materials with a lower Young's Modulus as seen in Figure 17.

Conversely, in a separate study of the investigation between curing temperature and the mechanical properties of PDMS conducted by Johnston et al. (2014), a linear relationship between the Elastic Modulus and curing temperature was observed. The Elastic Modulus approximately doubled from 1.32 MPa to 2.97 MPa by increasing the curing temperature from 25 °C to 200 °C; illustrated in Figure 16. However, the curing process is different to that of Liu et al. (2009). All samples were mixed at room temperature (pre-polymer base and curing agent) using a commercial flocculator for 1 minute at a speed of 195rpm. Samples followed a process of degassing and subsequently poured into the ASTM standard tensile test moulds. Test specimens were all cured using a digitally controlled oven with the features of precise control of the operating temperature. The temperature conditions investigated were 25 °C, 100 °C, 125 °C, 150 °C and 200 °C.

The linear correlation between the Elastic Modulus and temperature and the doubling of the Elastic Modulus with the temperatures ranges from 23 °C to 190 °C are also noticed in the study from Schneider et al. (2008). However, all samples were cured at 150 °C for 15min in an oven and the tensile tests were performed in a temperature-controlled chamber at 23 °C, 70 °C, 175 °C and 190 °C.

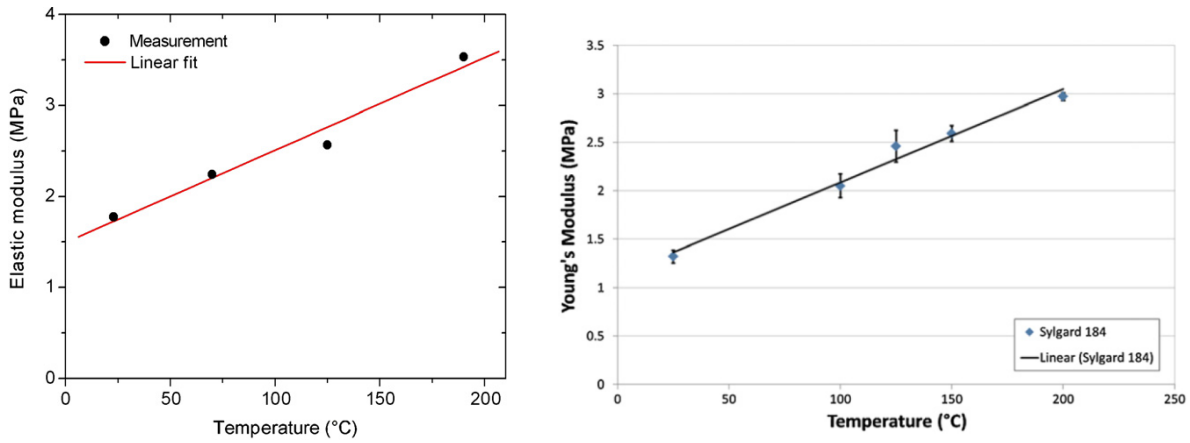

Figure 16: Relationship between Elastic Modulus and operation temperature on the left (with permission from Schneider et al. (2008)) and relationship between Elastic Modulus and curing temperature of Sylgard 184 on the right (with permission from Johnston et al. (2014))

Liu et al. (2009) reported that curing the PDMS elastomers greater than 200 °C reduced the mechanical strength greatly due to thermal decomposition. Liu et al. (2009) also stated that the mechanical properties were independent of the duration of heating, for PDMS substrates cured at low temperatures, shown in Figure 17.

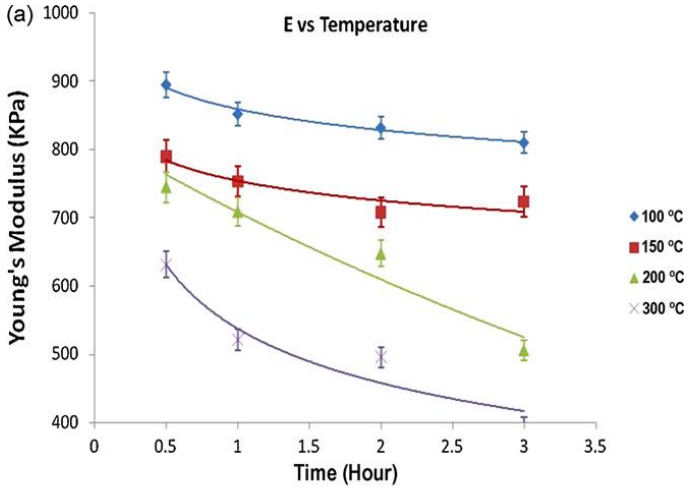

Figure 17: Heating temperature effects on Young's modulus of PDMS (with permission from Liu et al. (2009))

1.5.1.3 Behaviours of PDMS (Hysteresis and Damping)

To model the mechanical features of elastomers, hyperelastic material theoretical models are applied. These models are used to predict the nonlinear stress-strain response of materials undergoing large deformations. The typical elastomer does not satisfy Hooke's law and has a nonlinear stress-strain curve, thus demonstrating complex behaviour (MSC.SoftwareCorporation 2010). The Young's Modulus of the PDMS cannot be described with a single number. Hyperelastic materials can tolerate large deformations without suffering plastic strains. The hyperelastic definition describes the stress-strain definition of an elastomeric material using its strain energy density function. Strain energy is defined as the energy stored in a body due to its deformation.

Elastomeric materials are difficult to compress volumetrically but relatively easy to stretch. A familiar example is the rubber band. There is a major difference of the moduli between tension and compression. This is one of the features of the incapability of Hooke's Law to model elastomers. Hooke's Law assumes that stress and strain are proportional, but this is certainly not the case for rubber-like materials. Elastomer materials are also known to be nearly incompressible (MSC.SoftwareCorporation 2010). This near incompressibility of elastomers is important in the theoretical modelling of hyperelastic materials.

Polydimethylsiloxane is a material with viscoelastic behaviour. A material with viscoelastic behaviour denotes that it has time-dependent behavioural properties. This means that the material does not respond the same way over time, but is dependent of its history. It is typical of elastomers to have such behaviours. Viscoelastic materials exhibit creep behaviour and stress-relaxation phenomena.

A material may creep when it is subjected to constant stress. Creep behaviour is the tendency of the material to undergo permanent deformation from the influence of mechanical stress. This phenomenon is demonstrated in Figure 18 with PDMS produced from Sylgard 184 experiencing a pressure of 3.125 Nmm^{-2} at a temperature of 23 °C (Schneider et al. 2008). Figure 18 displays that creep behaviour is increased with an increased thinner solution. This is due to the decreased number of cross-links per unit area of the polymer network, which decreases the stiffness of the material, thus succumbing to more strain.

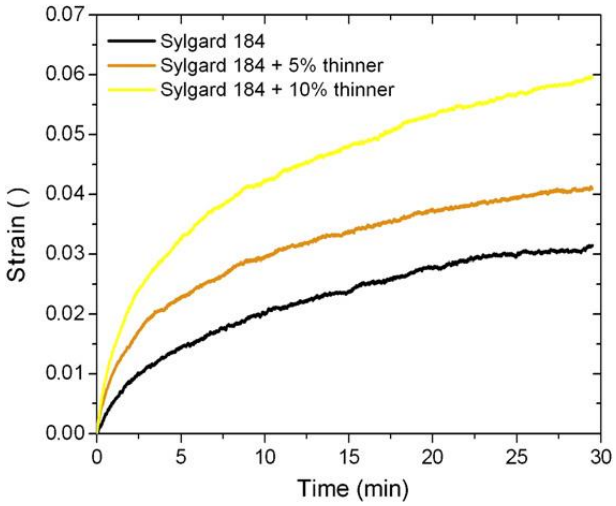

Figure 18: Strain–time relationship of Sylgard 184 PDMS with 3.125 $N.mm^{-2}$ stress. Different concentrations of Sylgard 184 PDMS was cast by the addition of different degrees of saline (thinner) solution (with permission from Schneider et al. (2008))

Stress-relaxation behaviour is observed when the material stress response decreases to the same amount of strain over the period of the load applied. This phenomenon is demonstrated by Dalrymple et al. (2007) in Figure 19; the stress response decreases at a gradual rate with a constant strain. In Figure 19, the overshoot of the stress response is seen; this is due to the inertia of the test-instrument actuator. In ideal stress-relaxation tests, the test specimen is strained instantaneously. The ability of a hyperelastic material to return to its original shape under continuous stress is measured using the creep and stress-relaxation test. These tests provide an idea of the time-dependence behaviour of a material.

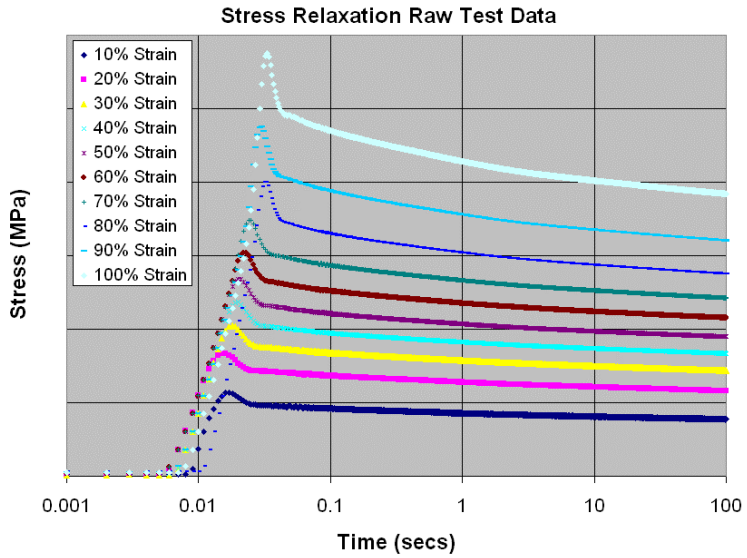

Figure 19: Stress response of elastomer material at different strain levels (adapted from Dalrymple et al. (2007))

From cyclic loading of an elastomer, energy is dissipated as heat. Repeated cycles of loading on a material can cause complications to its stress-strain response. This is due to the hysteresis effects. Hysteresis is a phenomenon in which a response by a body is delayed or lags behind in reacting to the changes of forces. It is a property of a system such that the output is dependent not only dependent on the input but also on the system's history.

Hysteresis behaviour causes loops in the stress-strain curve as can be seen in Figure 20. In the experiments conducted by Kim et al. (2011), PDMS test specimens of different pre-polymer to curing agent ratios were subjected to tension tests to investigate their nonlinear mechanical properties. The tension test consisted of 2 sets of 10 repetition cyclic tests followed by a structural breakage test (single-pull-till-failure). The first cyclic test was straining the test specimen to 50% for 10 cycles and the latter to 100%. The stress-strain curve in Figure 20 shows no noticeable change in the stress response for the cycles of 50% strain. However, the hysteresis loop is evident when the sample undergoes the 100% strain cycle. Kim et al. (2011) observed that hysteresis began to subside from the first load and unload cycle paths and the successive load and unload paths eventually converged to reach a state of equilibrium. In the latter experiments of an increased ratio of base polymer to curing agent, the effects of hysteresis were reduced. Kim et al. (2011) concluded that when PDMS is cured with more hardening agent, stress-softening occurs and creep behaviours exist when strain magnitude was increased in cyclic tension tests.

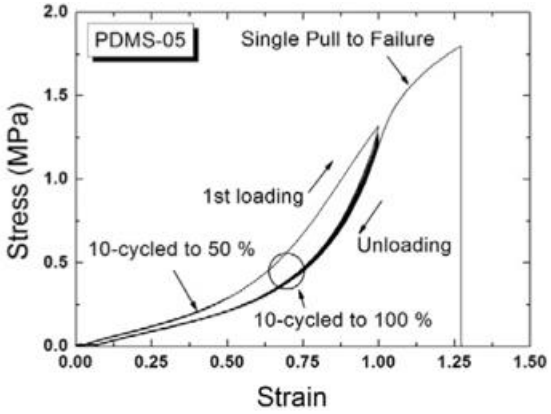

Figure 20: Stress-strain curve of PDMS with 5:1 base polymer to curing agent ratio (from Kim et al. (2011))

The stress-softening of the PDMS-05 (Kim et al. 2011) is known as the Mullins' effect. The Mullins' effect phenomenon describes the effect of cycles of loading decreasing the stiffness of elastomeric materials. When the elastomer experiences its first deformation, it becomes gradually stiffened. After a few cycles of loading and unloading, the elastomer softens. The cycles of strain damage the cross-links in the polymer network. The Mullins' effect further describes the repeated deformation causing the elastomeric material to reach a steady state stress-strain curve (Mullins 1969), as can be observed in Figure 20 and Figure 22.

Because elastomers are viscoelastic materials, they exhibit damping behaviours. This means the stress-strain response of elastomers is rate dependent, as can be observed in Figure 21 (Khanafer et al. 2009). Damping is the effect of the stress-strain curve increasing in stiffness as the rate of strain increases. From Figure 21, as the ratio of pre-polymer to curing agent is increased, the difference in the Elastic Modulus between a lower cross-head speed and higher cross-head speed is not as apparent.

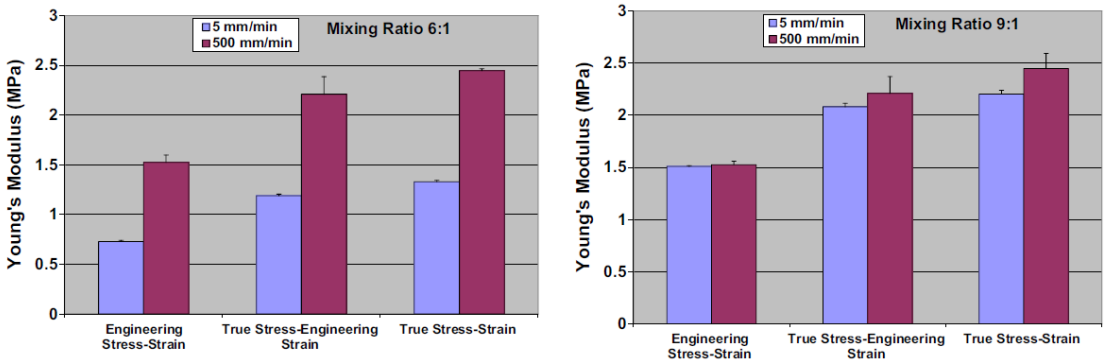

Figure 21: The effect of the strain rate on the Young's Modulus at different crosshead speeds and different mixing ratios (with permission from Khanafer et al. (2009))

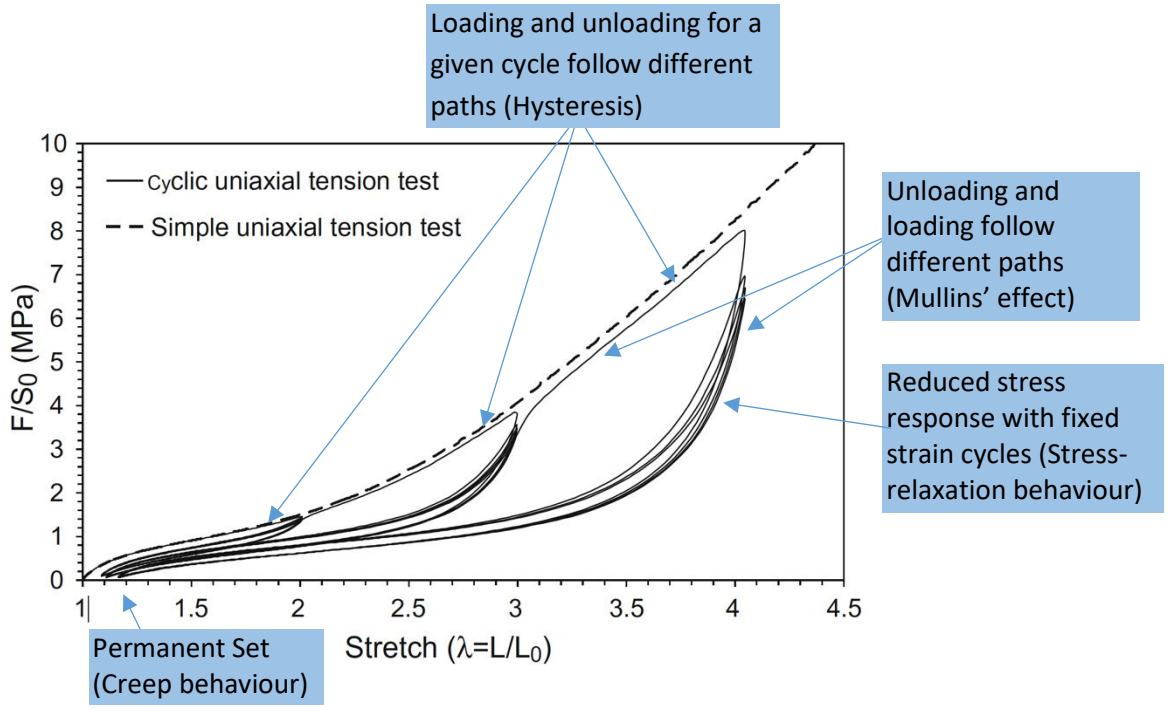

Figure 22: Stress–strain responses of carbon-black filled styrene-butadiene rubber (adapted with permission from Diani et al. (2009))

Elastomeric materials have complex behaviours. Their nonlinearity stress-strain curve feature originates from the viscoelastic behaviours as described above.

Figure 22 demonstrates well-described behaviours of a typical viscoelastic material. Creep behaviour is displayed from the permanent setting of the rubber. The diagram indicates that the residual extension remains after cycles of unloading and unloading. Stress-relaxation behaviour is observed from the progressive damage indicated by the reduced stress response with fixed strain loading cycles. The loading and unloading for a given cycle follow different paths due to energy dissipation is demonstrated by the hysteresis loops. Stress-softening is shown by the different paths of unloading and loading due to damage to the material.

From the description of a viscoelastic material. Polydimethylsiloxane (PDMS) strain characterisation follows a complex procedure. It is necessary to be consistent when preparing test samples. Test specimens should share the same curing history for precise measurements.

After determination of the behavioural measurement values of test specimens. A choice will depend to a large extent on the availability of test data. According to Dassault Systèmes®, when data from different modes are available, the Van de Waals and Ogden strain energy functions are more accurate in fitting the stress-strain curves. When data is limited it is best to use reduced polynomial functions such as the Marlow, Arruda-Boyce or Neo-Hooken models.

1.5.2 Hydrogel

Hydrogels are polymeric materials of high water content and have diverse physical properties. Water content can range from 70% to 99% (Oyen 2013). The network of polymeric chains is hydrophilic. Which means that the polymeric material can accommodate large quantities of water without dissolving. Hydrogel substrates are engineered to resemble the extracellular environment of the body's biological tissues to mimic the surroundings of the cells undergoing the bio-mechanic

experiment (Griffith 2002). Due to its high water content, hydrogels are able to be sustainable in living systems and not cause physiological rejections (Oyen 2013).

Mechanical and chemical considerations are not the only aspects involved in hydrogel development; the cell compatibility of the hydrogel material is designed by considering both the biological and physical attributes of the cellular environment to achieve specific interactions and responses of cellular systems. In essence, a cell-compatible hydrogel is characterized by its ability to control specific molecular interactions at the cell-material interface (Seliktar 2012). These molecular interactions include receptor-ligand complexes that mediate cell adhesion, biodegradation or transcriptional events that govern cell phenotype and focal adhesion interactions to transmit mechanical stresses to cells (Seliktar 2012).

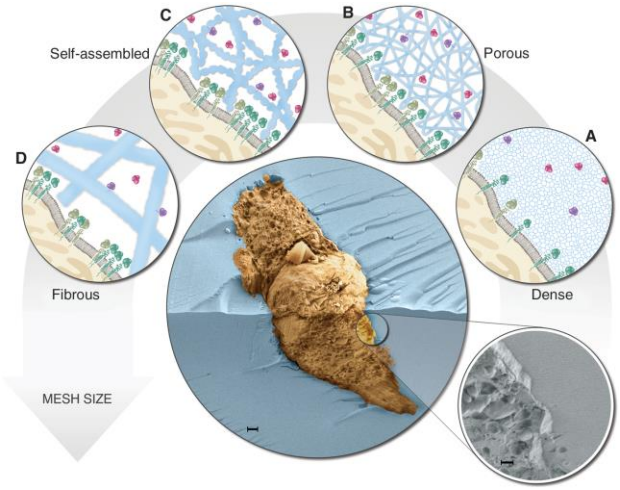

Figure 23: Interface between cell and hydrogel (with permission from Seliktar (2012))

Figure 23 depicts the 3D interface between the hydrated hydrogel (blue) and the captured cell (brown). The insert on the bottom right is the magnification of the interface between the cell membrane and hydrogel.

The four inserts (**A** to **D**) from right to left illustrate the activity between the cell membrane and hydrogel ranging from dense polymer network to fibrous polymer network. The blue depicts the polymer network and the white depicts the void space in the different types of hydrogel structures. The green represents the cell receptor proteins that lie on the cell membrane (grey). The soluble bioactive molecules (red) and the tethered bioactive factors (purple) lie within the hydrogel mesh.

The polymer network mesh size of the hydrogel is engineered to control the transport of the different factors such as receptor-ligand interactions and even cell motility.

In **A** and **B,** the polymer network is dense and has no definite structure which prohibits contact between the receptors and ligands. The molecular interactions are less favoured due to this special confinement.

The fibrous structure of **C** and **D** enable the focal adhesion contacts between the cell and the hydrogel polymer network through receptor-ligand clustering. **D** facilitates amoeboid cell motility within the larger pores.

Although, most hydrogels are biocompatible, hydrogels generally have poor mechanical properties compared to that of solid polymers. These complex substrates exhibit particular properties of a solid and some properties of a liquid; identifying them as a multi-phase material (Oyen 2013). Thus, hydrogels require a complex analysis to describe their mechanical properties.

Anseth et al. (1996) proposed that mechanical properties of hydrogels were best understood using both theories of rubber elasticity and viscoelasticity. In their swollen state, hydrogels demonstrate properties of rubber. The mechanical behaviour of the gel is dependent on the architecture of the polymer matrix. In low temperatures, the hydrogels lose their elastic properties and exhibit viscoelastic behaviour. Anseth et al. (1996) concluded that the mechanical properties of hydrogels were dependent on the polymer matrix structure, cross-linking density and the degree of the swelling. In a review conducted by Ahearne et al. (2008); it was revealed that when cells were seeded in the hydrogel sample, the mechanical strengths of the matrix improved from the reorganization of the polymer fibres and products of the extracellular matrix.

The complexity of hydrogel substrates presents difficulty for researchers to work with and to mechanically define. During testing, hydrogel samples are subjected to water loss which alters the structure of the polymer matrix and obscures the results of the experimentation to characterize the mechanical properties (Anseth et al. 1996). The elastic modulus of this multi-phase material is in the order of kilo-pascals (kPa), which brings about difficulty in measurement; as most mechanical testing equipment is designed to test materials in the range of mega-pascals (MPa) to giga-pascals (GPa) (Oyen 2013). Other difficulties include the gripping or cleaving of the hydrogel. Methods of gripping the hydrogel in various research include the use of cardboard tabs, double sided tape and polymeric glue (Normand et al. 2000).

Through various literature research, the mechanical properties of hydrogel substrates are not clearly defined. In the examination of the papers reviewed, there is large variability in data, measurement accuracy and precision of hydrogel properties is low. There was very little calibration or verification of testing techniques of known standard that was found (Oyen 2013). Oyen (2013) suggested that there is a need for consensus and standardization in this field of research on the testing techniques of mechanical characterisation and analysis of data.

1.6 Cell Imaging Methods

Common imaging techniques for the study and analysis of cell mechanics are atomic force microscopy (AFM), optical tweezers and confocal microscopy (Unal et al. 2014). Although AFM and optical tweezers have imaging functionality, these techniques are primarily for mechanical manipulation. AFM and optical tweezers were examined previously. The following will discuss a brief overview of optical microscopy and more specifically of confocal microscopy.

1.6.1 Optical Microscopy

The optical microscope is commonly used in the study of cell biology and mechanics. Optical microscopy offers high-resolution imaging and 3D volume construction. These features allow for measurements of cell deformation and strain. With the advancement of the optical microscopy technology, fluorescence and confocal microscopes were developed. These techniques offer real-time high-resolution 3D imaging (Unal et al. 2014).

Confocal microscopy performs a point-by-point image construction by focusing a laser beam sequentially across the specimen and collecting data of the returning rays (Semwogerere and Weeks 2005). The basic approach of confocal microscopy is the use of spatial filtering techniques to eliminate out-of-focus light in the specimens where the thickness exceeds the dimensions of the focal plane (OLYMPUS 2012). The point-by-point illumination of samples results in high-resolution 3D imaging by the reconstruction and stacking of collected sets of images at different depths.

1.7 Limitations and Scope

Current devices are exceptionally expensive and are aimed at commercial applications such as biological research companies. A uniaxial stretcher from STREX Inc. (Osaka, Japan), that is microscope mountable was offered at USD 15 000. Academic institutions, in particular in developing countries, tend to develop their own devices for specific experiments as it is of lower cost to develop their own.

The Mechanobiology Laboratory of Division of Biomedical Engineering did not have equipment to undertake experiments in cell mechanics in vitro. One research focus of interest is for example cell therapies for myocardial infarction, including understanding mechanisms of mechanotransduction in therapeutically delivered cells in the infarcted heart, and collagen production by cardiac fibroblasts and myofibroblasts associated with infarct scar development.

Experimental studies and data will greatly enhance the research undertaken towards predictive computational modelling on these topics.

1.8 Aim & Objectives

1.8.1 Aim

The aim of this research project was to develop a mechanical cell loading device for the Mechanobiology Laboratory in UCT's Division of Biomedical Engineering to perform cellular mechanic experiments. The device was to provide the three primary load types, tension, compression and shear. Strain field characterisation of the PDMS substrates was also investigated to illustrate the areas of similar strain.

1.8.2 Identification of Requirements and Specifications of Mechanical Loading Device

The device developed was to perform the following tasks:

1. Uniaxial tension of 2D and 3D cell culture constructs
   Uniaxial compression of 3D cell culture constructs
   Shearing of 3D cell culture constructs

2. Tension load experiments with live microscopy imaging.

3. Uniform strain across cell culture area of the membrane.

4. Obtain a calibrated output tensile stain corresponding to the tensile strain set in the motor control user-interface.

1.8.3 Objectives

The objectives of the project were as follows:

1. Development and optimisation of design of cell loading device and sample fixtures required for different load types.

2. Manufacturing of the device components.

3. Assembly of the device.

4. Characterisation of the strain fields on PDMS membranes (without cultured cells).

5. Development of FEA models of PDMS membranes to simulate experiments with cell loading device.

One of the main objectives of the design and development of the cell stretcher device was to be cost-effective. The design was also required to incorporate the available confocal microscope offered by the Health Sciences Faculty for live cell imaging. The developed cell stretcher device was essential to be able to perform the following types of force on the substrate: stretch, compression and shear.

2 Methodology

This chapter is separated into seven sections. Section 2.1 describes the design process and approach of the 3 modalities of stress: tension, compression and shear. Section 2.2 describes the design methods and the process of moulding the various types of polydimethylsiloxane (PDMS) membranes. The experimental methodology of the mechanical cell manipulator and the preparation of the PDMS membranes are discussed in Section 2.3. Section 2.4 describes the method of processing and analysing the acquired data from the experimentation of the device. Section 2.5 provides the method to quantify the effectiveness of the device and the different types of designed PDMS membranes. Learning from the results of the analysis, a method to improve the accuracy is illustrated in Section 2.6 with a block diagram. This chapter concludes with section 2.7, which describes the setup of the FEA models of the various types of PDMS membranes and details of the input and assumptions made to develop the FEA models.

2.1 Device Design

Following the design requirements as introduced in the beginning chapter, the design of the project contains three essential aspects:

1. A design method of the device to be microscope mountable – the selected device dimensions allows the device to work within the microscope workspace for live cell imaging.

2. The mechanical systems and components design to deliver tension, shear and compression load on the substrates – this entails the various components to be suitable for each load type and includes the mechanisms or components to grasp or hold the substrates.

3. The method to provide uniaxial translation movement for the three types of load – this aspect entails the selection of electronic hardware and software components, such as the linear actuator motor to mechanically load the substrates, microcontroller and user-interface.

A CAD Software (Solidworks®) was used to design the different components. The different components are assembled together in the CAD software for the overall mechanical cell loading device design. Conceptual and manufacturing aspects are discussed further in this chapter.

2.1.1 Methodology of Device to be Microscope Mountable

2.1.1.1 Conceptual Design of Mounting Device on Microscope

The specimen holder from the Carl Zeiss LSM510 Confocal Microscope (the microscope used in this investigation) is a removable component from the microscope stage. It is a piece of equipment which is part of the microscope and its function is to hold glass slides in place. The specimen holder acts as a stage tray as to mount firmly onto the microscope stage.

To suit the requirement of the designed device to be able to mount onto a microscope, the specimen required remodelling. The removability of the specimen holder and its immovable features on the microscope stage, motivated the remodelling and modification of it to suit the requirement of the designed device to be able to mount onto a microscope. The Specimen Holder of the Carl Zeiss LSM510 confocal microscope is shown in Figure 24.

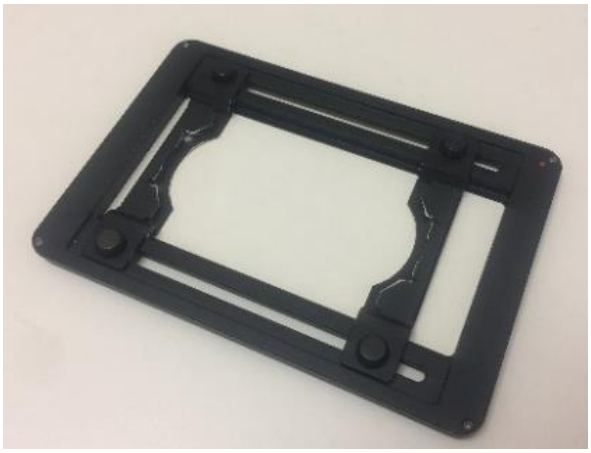

Figure 24: Photographed specimen holder from the Carl Zeiss Axiovert 200M

The original specimen holder model was imported into the Solidworks® CAD software and duplicated. The accuracy of the measurements of the duplicated model was then verified by 3D printing the imported model and it was then fitted onto the microscope stage. This process was to ensure the validity of the Solidworks® CAD model and its measurements, as shown in Figure 25.

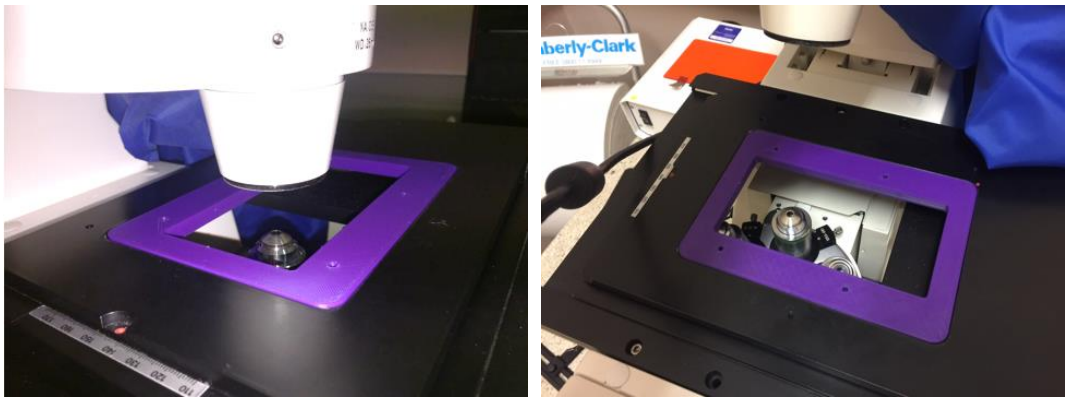

Figure 25: 3D printed model of the original specimen holder

2.1.1.2 Prototype Design of Mounting Device on Microscope

After the verification process of the duplication model; additional modifications were made on the Solidworks® CAD software to accommodate the device design. Polypropylene was the material was used for the final manufacturing of the microscope fitting component at the UCT Mechanical Engineering workshop as shown in Figure 26. The polypropylene material was chosen specifically to be used for the microscope fitting component due to its durability and non-abrasive nature as to not cause damage to the microscope stage. The consideration for using this material is for the advantage of low-cost replaceability. Using abrasive materials could cause potential damage to the microscope stage leading to costly repairs. The microscope fitting component, therefore, acts as the sacrificial component of the cell loading device as to avoid the abrasion of the microscope stage from the regular removal and insertion upon usage of the mechanical cell manipulator device.

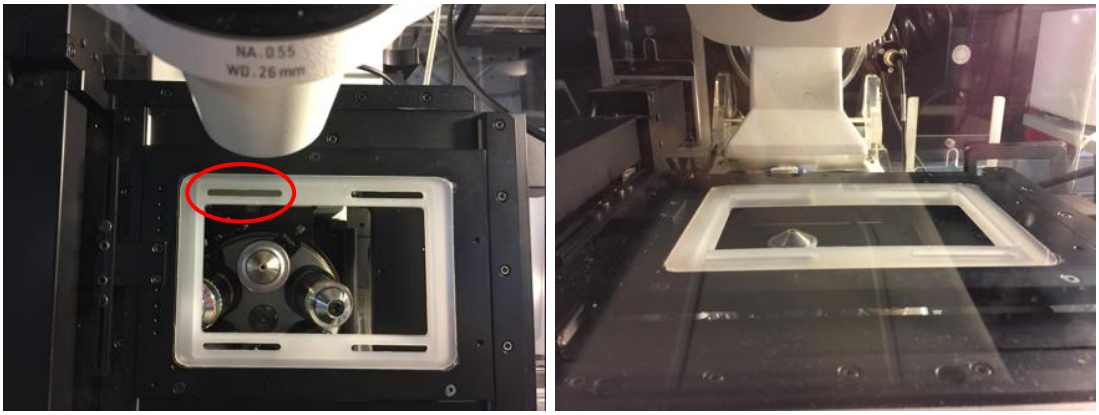

Figure 26: Final design of microscope fitting component based on the specimen holder of the microscope

The final design of the microscope fitting contains elongated slots (circled in red) as shown in Figure 26. The elongated slots are to increase the range of positions to accommodate the mechanical cell manipulator along the microscope stage. This design allows for the device to be positioned accordingly for cells to be within the objective view. Additionally, in Figure 26 it is seen that the remodelled microscope fitting is flush with the microscope stage, indicating the validity from software design to the manufacturing process of the component.

2.1.2 Mechanical Systems and Components Design

2.1.2.1 Conceptual Design of Tension Loading System

As mentioned briefly in the introducing chapters, the mechanical cell manipulator developed in the project is based on the cell stretcher design from the Friedrich Alexander University Erlangen-Nuremberg in Germany. Modifications were made to the original design to accommodate for the Carl Zeiss LSM510 Confocal Microscope. More modifications were made to provide for different load types of compression and shear.

The substrate experiences tension when a stress is applied on one end of it while the opposite end is fixated. The stress applied to the substrate acts in the opposite direction to the fixated edge. Strain is the mechanical deformation or the change in shape as a result of mechanical stress. By definition, strain is the ratio of the displacement to the original length of shape. By stretching the substrate matrix by a certain strain, the contents in the matrix experience the same strain, provided that the substrate undergoes absolute uniform strain. Figure 27, demonstrates the concept of tension load adhered by the designed device.

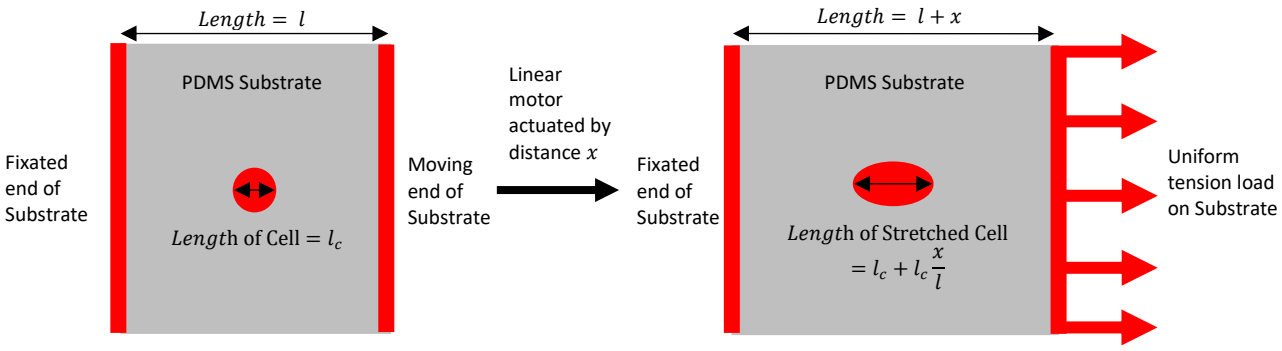

Figure 27: Conceptual design of tension system

To attain uniform strain, it is required that uniform stress is to be applied to the substrate. This is achieved by the design of two membrane clamping components, which are labelled "*11*" in Figure 29. The clamping components grapple or "lip over" the edges of the substrate and are tightly secured. Figure 28 illustrates this concept.

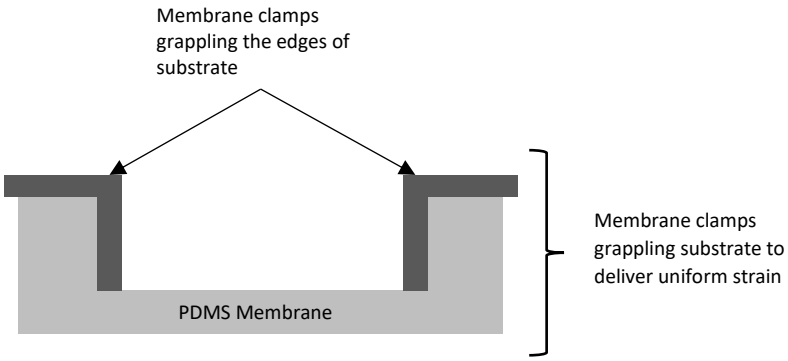

Figure 28: Cross-section of conceptual model of clamps and substrate

In Figure 29, it additionally illustrates a labelled technical diagram to show the relationship of the various components which form the entire assembly of the device to perform tension load type. Furthermore, Figure 30 displays the assembled mechanical device.

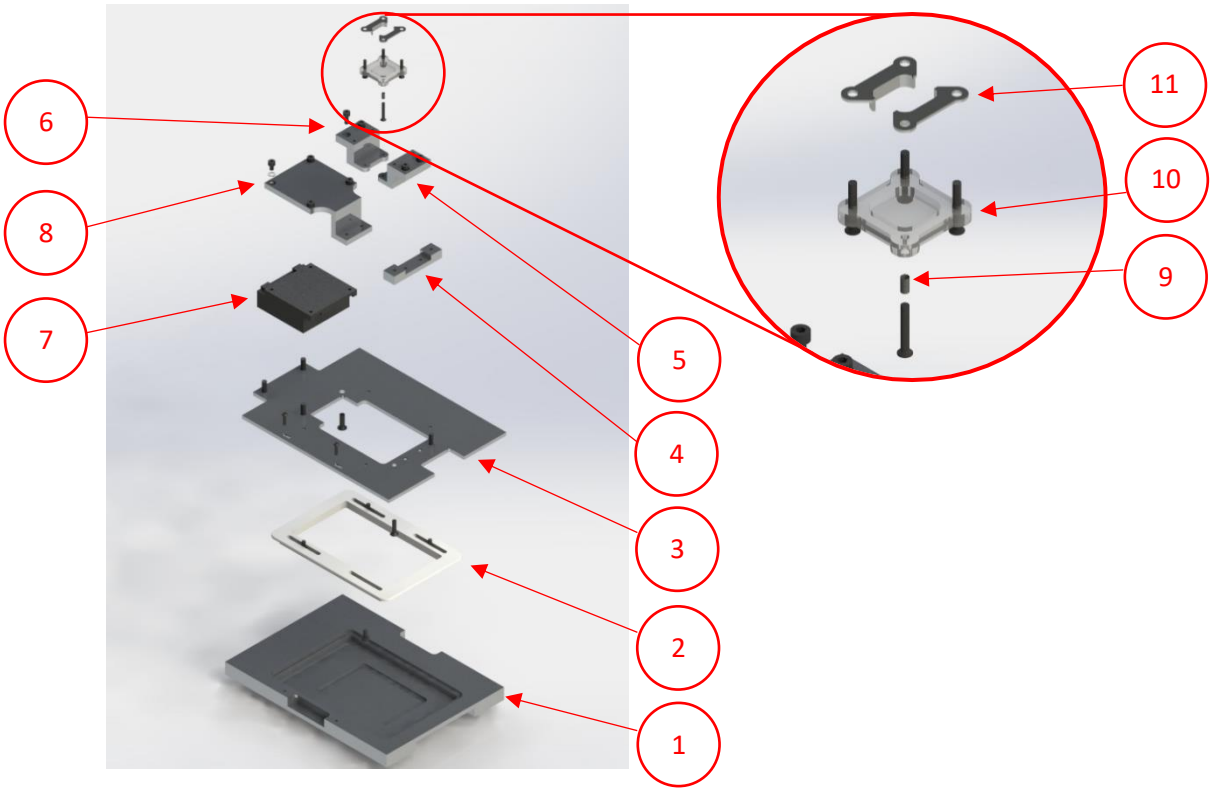

Figure 29: Design of tension system of mechanical cell loading device (exploded view) and close-up of PDMS membrane

The following labels and descriptions depict the components in Figure 29:

1. **Base Plate** – this component serves to contain and hold the device when the device is not used under the microscope.
2. **Microscope Fitting** – this component is modelled from the **Specimen Holder** of the Carl Zeiss LSM510 Confocal Microscope. The **Microscope Fitting** inserts firmly into the

mechanical stage of the microscope to provide the device firm support and prevent unstable movements. The material of this unit is of plastic type, polypropylene. It is the sacrificial component of the device to prevent wearing of the microscope stage from multiple insertions and removals.

3. **Assembly Plate** – the **Assembly Plate** is a platform to support the device components. All components are assembled onto the **Assembly Plate**.
4. **Support Bracket** – this component provides the different load modules of the one end of the mechanical cell loading device to be the same height as the other end that is attached to the **Linear Motor**.
5. **Tension Module A** – this component is to hold the membrane. It is designed with two elongated screws to grapple onto the membrane.
6. **Tension Module B** – the component is of similar design to **Tension Module A** and is positioned on the opposite side of **A** to grapple the membrane.
7. **Linear Motor** – the Linear Motor produces the uniaxial translation movement to provide the various types of mechanical loading on cells. The **Linear Motor** is a programmable component of the mechanical cell loading device.
8. **Motor Attachment** – this component is attached to the **Linear Motor** and **Tension Module B** which holds the PDMS membrane where the cells are cultured.
9. **Heat Shrink** – heat shrink is used to conceal the threads of the screws to prevent the sharp edges of the screws severing the PDMS membrane.
10. **PDMS Membrane** – the PDMS membrane is where the cells are seeded on.
11. **Membrane Clamps –** the membrane clamps grip onto the PDMS substrate and are designed to provide uniform strain during tension.

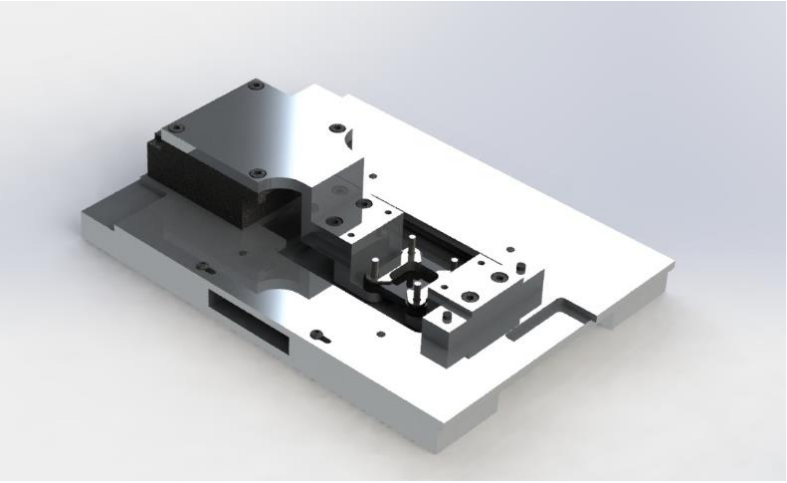

Figure 30: Rendered CAD design model of tension system of mechanical cell loading device (assembled view)

2.1.2.2 Conceptual Design of Compression Loading System

In this study, the substrate with cells seeded inside is placed in the cell well against the wall. A compression module oscillates back and forth, compressing and releasing the substrate against the cell wall.

Figure 31 demonstrates the conceptual design of the compression system. In this design method, the load is placed against the *Compression Cell Well* component, labelled "*5"* in Figure 32. The substrate

experiences compression when the perpendicular load, *Compression Module B* is pressed against the wall of the cell well. This method of stress is opposite to that of tension. Saline solution should be used as a means of keeping the cells within the substrate hydrated to allow for long periods of experimentation.

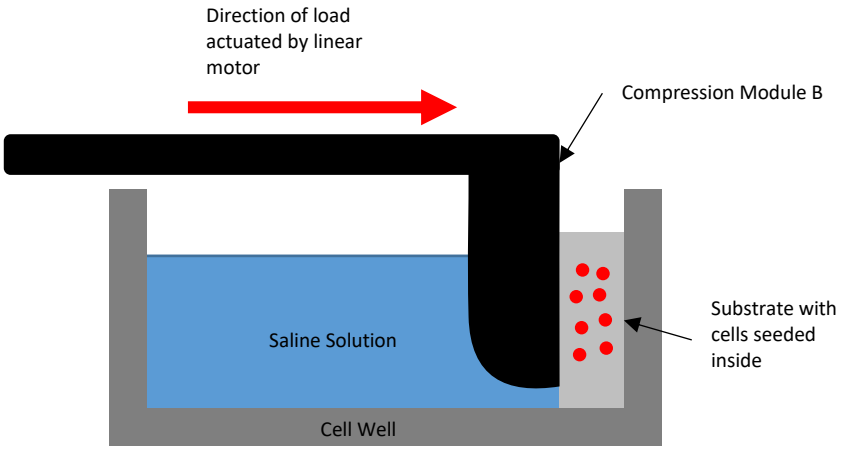

Figure 31: Conceptual design of compression system

Figure 32 illustrates the exploded view of the device for the method of compression load and the relationship of the various components. Figure 32 only labels the components that are essential to the compression system, since fundamental components of the device have been described in Figure 29. An assembled view of the device for compression loading is displayed in Figure 33.

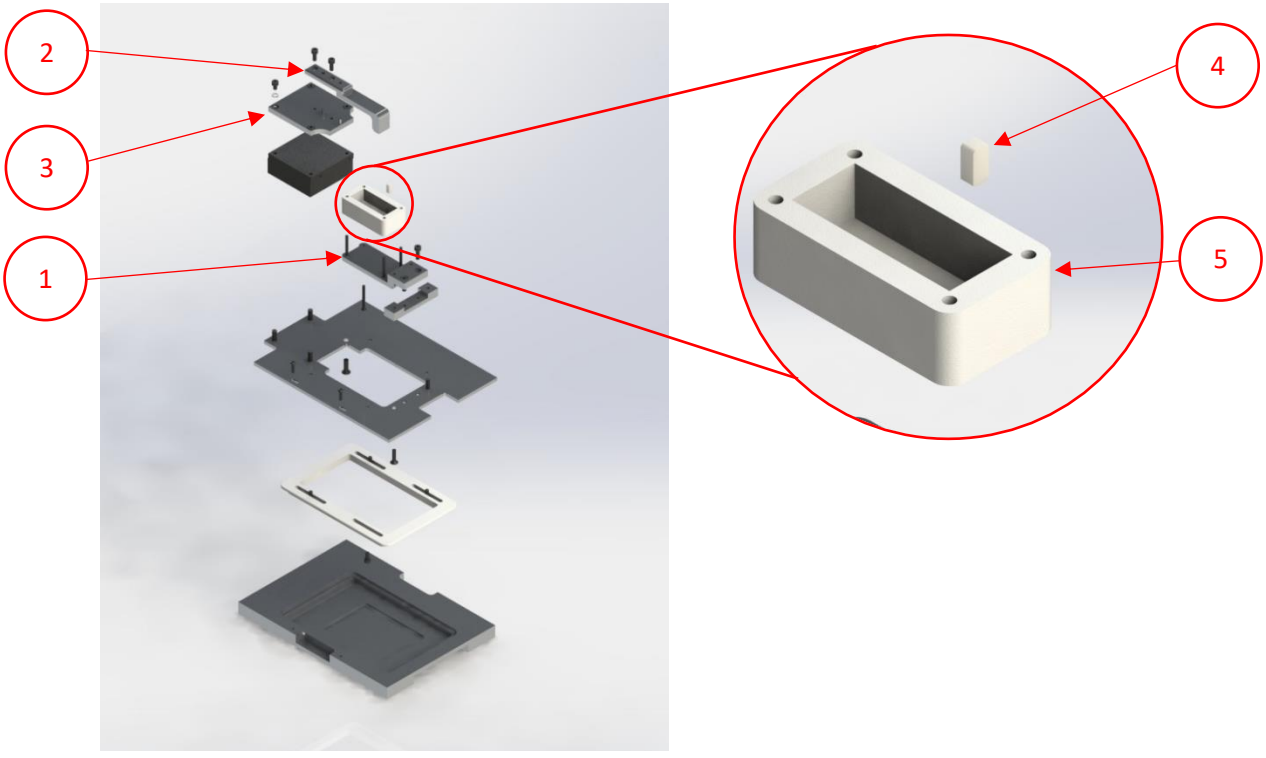

Figure 32: Design of compression system of mechanical cell loading device (exploded view) and close-up of substrate in compression cell well

The following labels and descriptions of the components depict Figure 32:

1. **Compression Module A** – this component is elongated to support the compression cell well.
2. **Compression Module B** – Compression Module B lies on the opposite end, where the motor is positioned. The module is designed with a flat surface head to compress the substrate.
3. **Motor Attachment** – The purpose of this component is to connect **Compression Module B** to the **Linear Motor**.
4. **Matrix Substrate** – The **Matrix Substrate** is where the cells will be seeded.
5. **Compression Cell Well** – In the cell well, the hydrogel substrate is seeded against the wall and arranged to be compressed by **Compression Module B**. Saline fluid is kept in the cell well to keep the cells hydrated and alive.

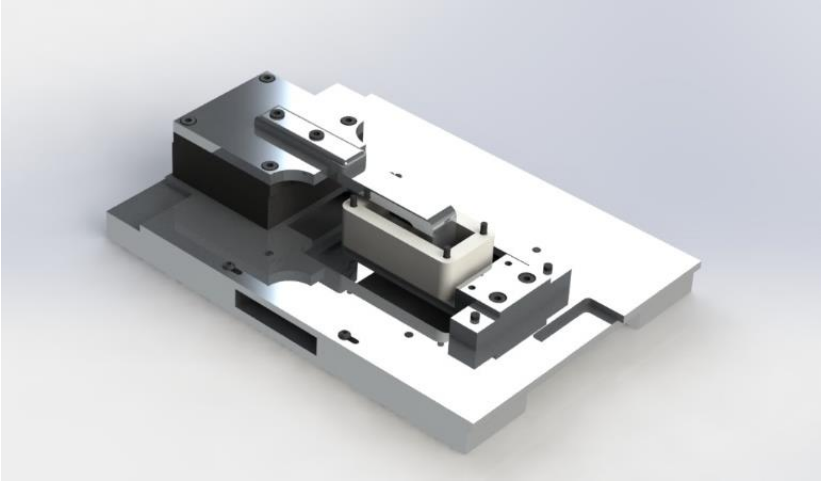

Figure 33: Rendered CAD design model of compression system of mechanical cell loading device (assembled view)

2.1.2.3 Conceptual Design of Shear Loading System

As mentioned in the literature review, typical methods of simulating shear stress on cells involve experimental devices such as the parallel-plate flow chamber and the viscometer. The method of shear stress being applied to cells in this study is unique and will be discussed further.

Shear stress is defined as the component of stress that is coplanar to the sample cross-section. The method of shear in this study takes the use of two parallel plates with the substrate matrix in between, demonstrated in Figure 34.

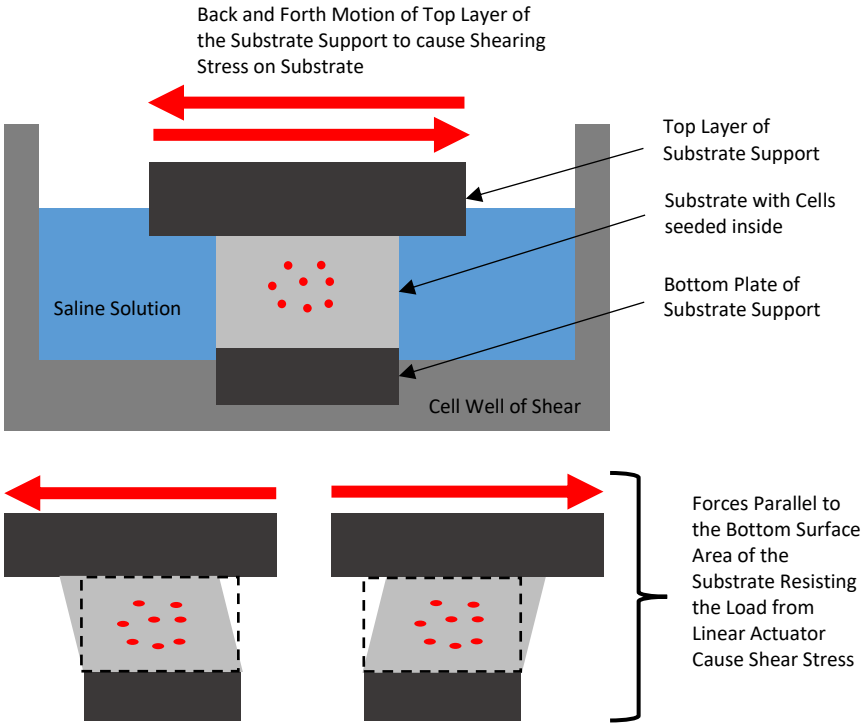

Figure 34: Conceptual design of sample loading in shear system

The bottom plate is stationary and is fixed in the cell well, whilst the top plate is attached to the linear motor. The substrate is held in between the top layer and the bottom layer. Saline fluid is contained by the cell well. The three components, the substrate, top and bottom plates are submerged within the saline fluid. Deformation of the shape of the substrate occurs as a result of the top plate moving forwards and backwards, whilst the bottom plate resists movement. Shear stress on the substrate matrix is thus experienced due to the resistance of movement of the bottom surface of the substrate.

Figure 35 illustrates a labelled exploded view, indicating the relationships of the various components. Figure 36 shows the fully assembled device for the shear load type.

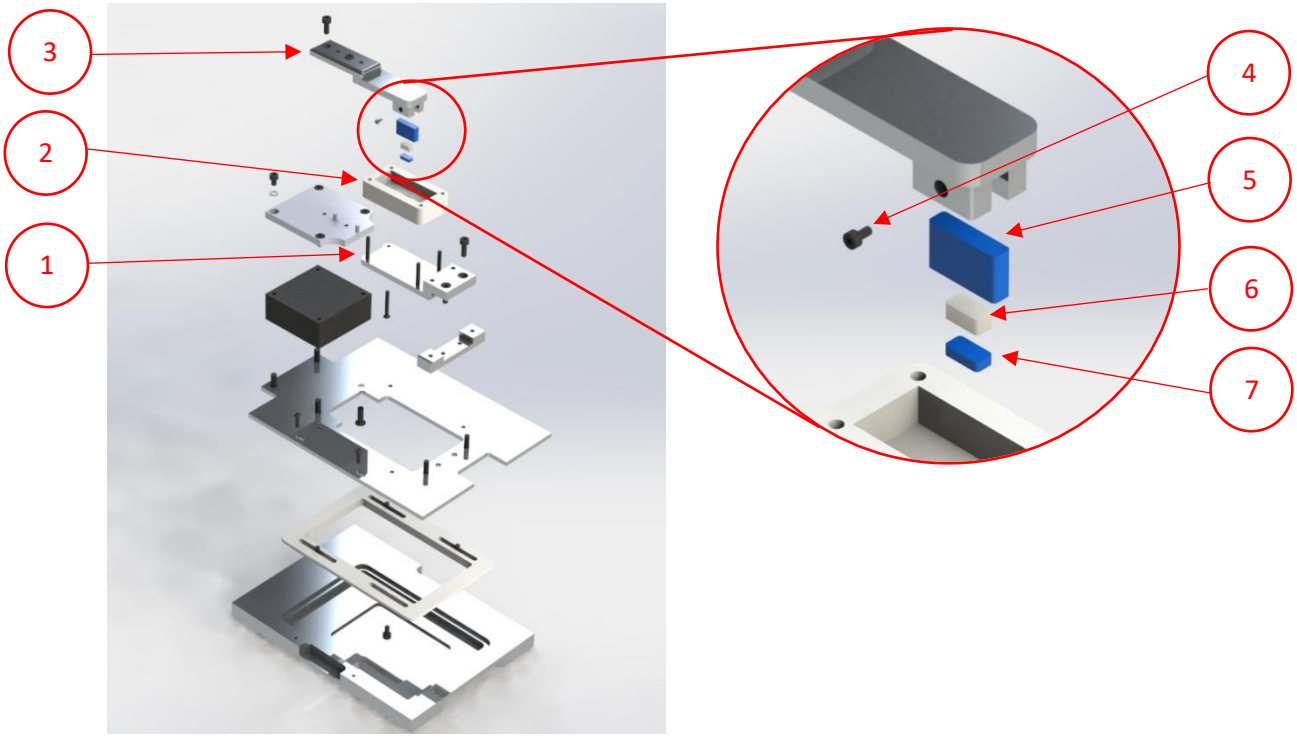

Figure 35: Design of shear system of mechanical cell loading device (exploded view) and close-up of substrate for shear loading

The following are the labels and descriptions of the components:

1. **Shear Module A** – This component is identical to that of **Compression Module A**. It supports the **Shear Cell Well**.
2. **Shear Cell Well** – The Hydrogel Substrate and saline fluid are contained in this component.
3. **Shear Module B** – Shear Module B is designed to clasp the substrate support. The **Linear Motor** actuates this component forwards and backwards to load shear stress on the hydrogel substrate.
4. **Fixator screw** – The Fixator Screw loosens or tightens for the removal or fixed positioning of the substrate mould.
5. **Substrate Support Layer Top** – ABS material is used to manufacture the Top and Bottom Support Layers. 3D printing was done to manufacture the two layers. The support layers help to hold and position the hydrogel substrate in a coordinated manner due to its fragility. The top layer is fastened by the **Fixator Screw** onto **Shear Module B** and actuates forwards and backwards movement.
6. **Hydrogel Matrix Substrate** – This component is cast together with **Hydrogel Support Top and Bottom Layer**. Cells are contained within the matrix substrate.
7. **Substrate Support Layer Bottom** – The bottom support layer is anchored to the bottom of the **Shear Cell Well**.

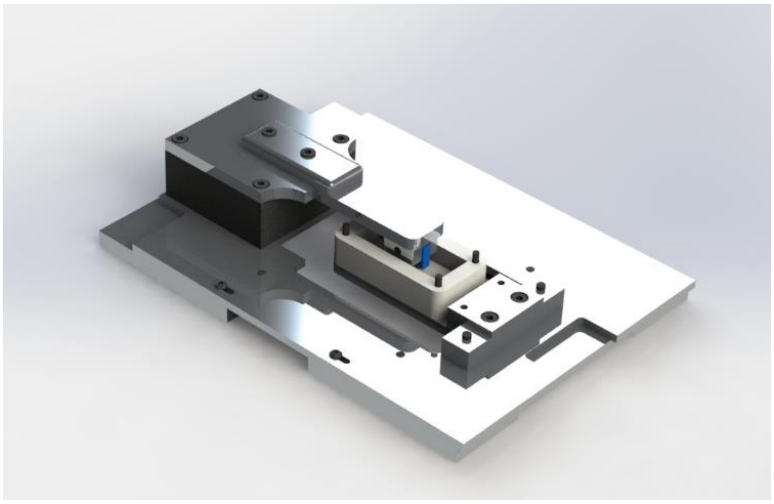

Figure 36: Rendered CAD design model of shearing system of mechanical cell loading device (assembled view)

2.1.3 Method to Provide Uniaxial Translation

An MT63-SM micro-stage from Steinmeyer (Albstadt, Germany) was selected for the project to illicit linear actuation. The MT63-SM micro-stage is driven by a stepper motor. Stepper motors are frequently used in precision positioning equipment. From the datasheet of the MT63-SM micro-stage from Steinmeyer, the accuracy of the micro-stage is ± 6µm.Thus, this renders the MT63-SM to offer a high resolution suitable which is for research and development.

The microcontroller, seen in Figure 37, was provided with the MT63-SM linear actuator by Steinmeyer. It is essential to the device setup as it communicates and translates data between the user-interface and the linear motor. The *FMC-Quick Access* application, seen in Figure 38 is also an important item to the device as this piece of software provides an interface between motor position and human control.

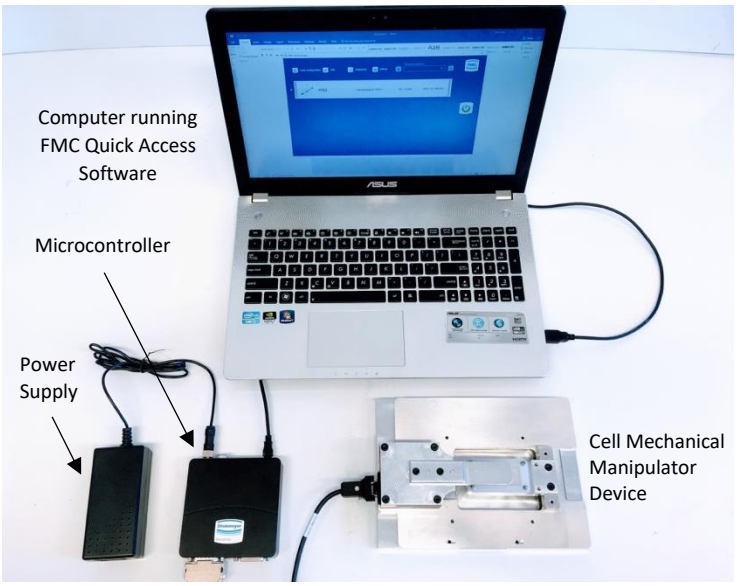

Figure 37: Photograph of hardware and software setup

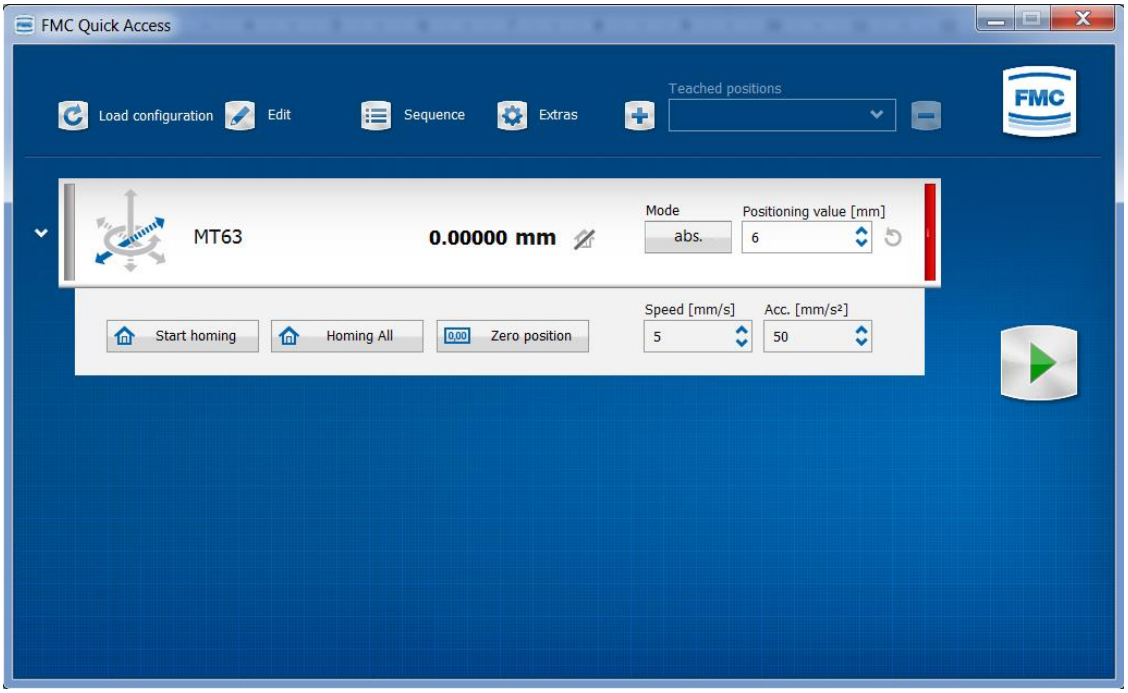

Figure 38: FMC Quick Access software – interface between user and device

2.2 Concept of PDMS Membrane Design

As mentioned in the literature review, the polydimethylsiloxane (PDMS) is a cost-effective, biocompatible material, thus inspiring its use. PDMS membrane design in this project was made specific to the tension system. Substrate design for the tension system was a more complex task compared to the design of the compression and shear systems, since the substrates for these two systems is of a simple cuboidal shape, shown in Figure 32 and Figure 35. This following section focuses on the design of PDMS substrates for the tension system.

Following the collaborator protocol, the initial membrane designed was a 20 mm x 20 mm cell culture area, illustrated in Figure 39a. The cell culture area is the location where cells are seeded and experiences the tension loads that are applied. The design of the 20 mm x 20 mm membrane ensued in two more designs, a 20 mm x 20 mm membrane with dividers and a 10 mm x 10 mm membrane, displayed in Figure 39b and Figure 39c, respectively.

The purpose of the membrane is to provide a supporting surface for the cells to seed on, while different sizes allow for different amounts of cellular samples. The 10 mm x 10 mm membrane was designed to avoid the manufacturing of additional device attachments; enabling the compatibility between the tension system components and all membrane geometry types. Thus, the 10 mm x 10 mm is designed with thick walls to take similar outer shape as the 20 mm x 20 mm PDMS membranes. The 20 mm × 20 mm membrane with dividers configuration, separates the area of cell culture into four quadrants. This type of configuration accommodates up to four different types of cellular samples on a single membrane.

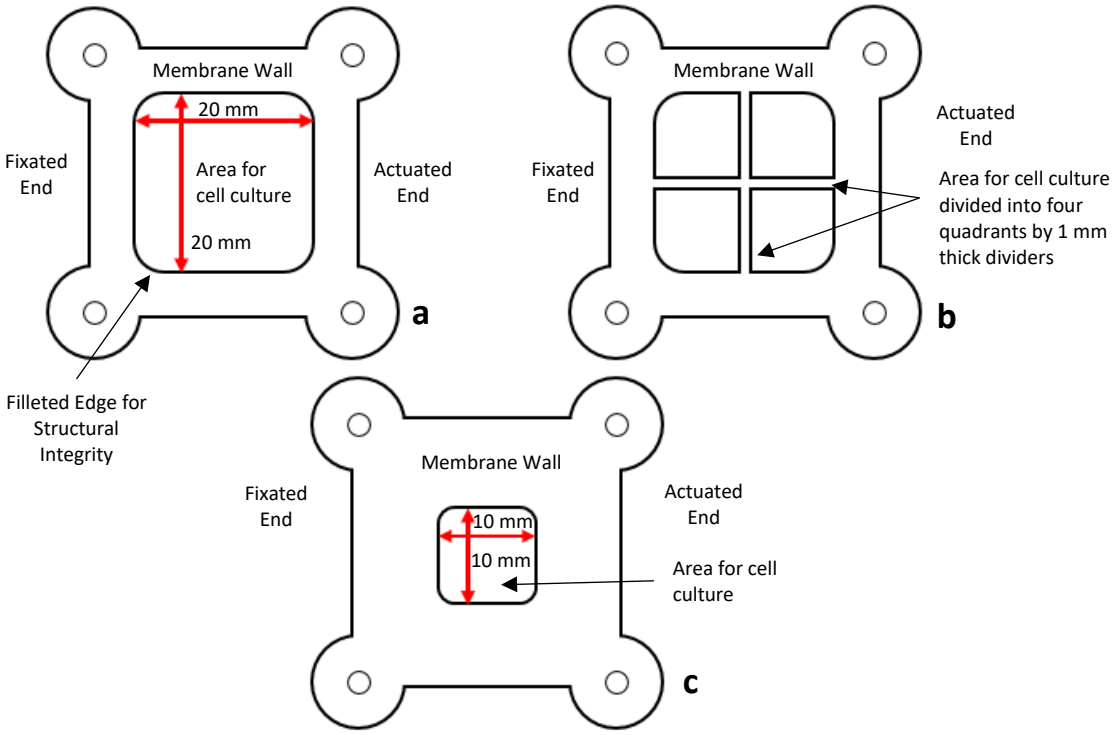

Figure 39: Conceptual schematic of PDMS membranes for tension system: (a) 20 mm x 20 mm membrane, (b) 20 mm x 20 mm membrane with dividers, (c) 10 mm x 10 mm membrane

Following the stipulated design procedure, Solidworks® CAD software was used to generate the substrate models for manufacturing, shown in Figure 40. Since PDMS comes in the form of two liquid parts, the silicone base and curing agent, it requires a process of moulding to form the substrates. Therefore, it was necessary to correspondingly design the mould negatives of the designed substrates illustrated in Figure 41.

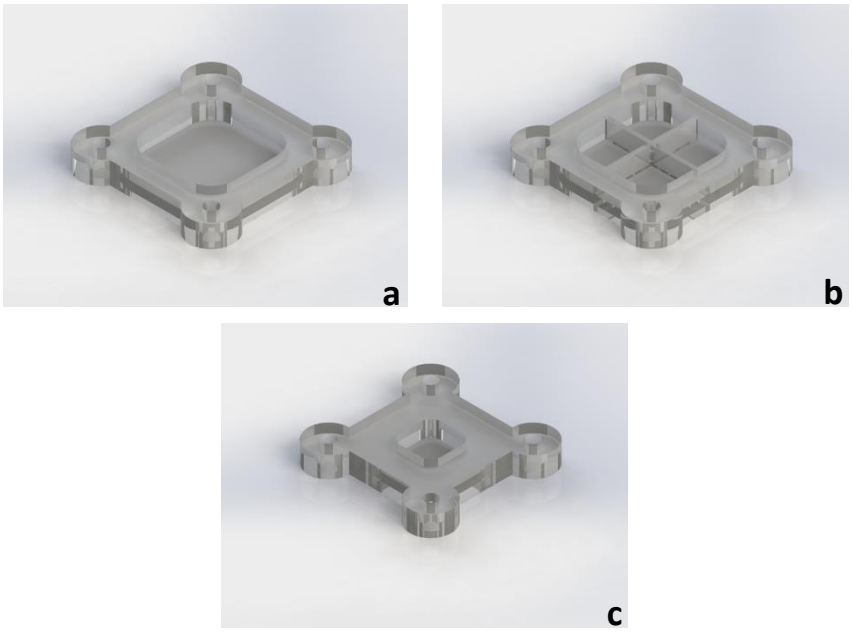

Figure 40: Rendered CAD model illustration of final conceptual designs of PDMS membranes for tension system: (a) 20 mm x 20 mm membrane, (b) 20 mm x 20 mm membrane with dividers, (c) 10 mm x 10 mm membrane

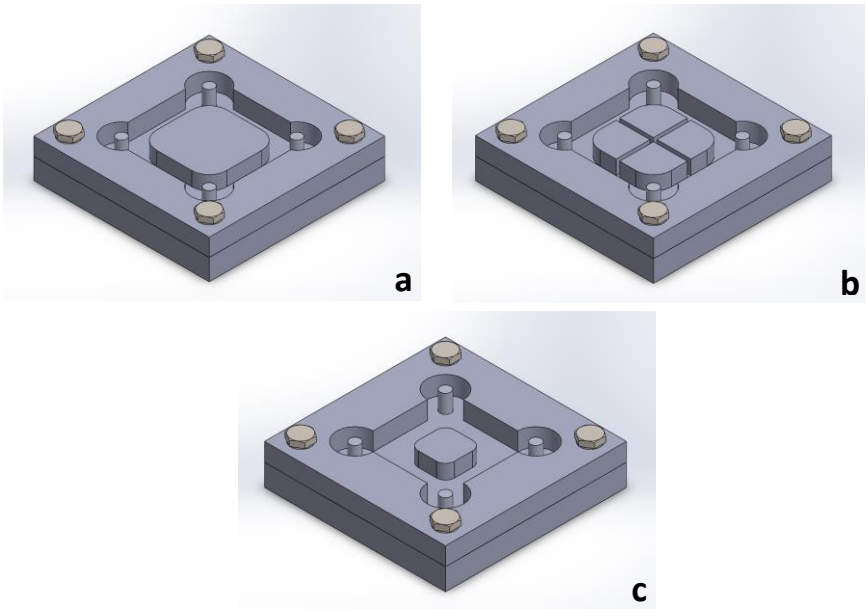

Figure 41: Designed CAD models of mould negatives for PDMS substrates

2.3 Experimental Assessment of Membrane Strain Distribution for Uniaxial Stretch

Practical Experimentation was only performed on the tension system as it is the only system viewable by the microscope. The experimentation includes testing of the device design and strain tests of the cured PDMS membranes. Membranes were put under tensile load and the strain deformation change was recorded. The collected data was processed for strain characterisation of the membranes. In the strain tests, the moulded substrate membranes are loaded into the developed tension system device and put under strains from 0% to 30%. The device is inserted into the microscope stage to record deformation change of the substrates via the on-board camera offered by the Carl Zeiss LSM 510 Confocal Microscope.

It was expected that PDMS membrane samples of each geometry type would be similar, thus three membrane samples of each type were manufactured to produce a mean value for each type of membrane. The membranes were marked with ink from a permanent marker (Artline® 725 Superior Point Permanent Marker) as a frame of reference for strain measurement. Using the permanent marker, dots were marked in grid format as shown in Figure 42. Each ink mark was used as a measurement point for strain output.

The 20 mm x 20 mm membrane was marked with 25 dots in a format of 5 rows by 5 columns, the 20 mm x 20 mm membrane with dividers was marked with 2 rows by 2 columns in each quadrant and the 10 mm x 10 mm membrane was marked with 3 rows by 3 columns. The number of dots indicates the number of readable data points. Thus, the 20 mm x 20 mm membrane offers 25 deformation results to be recorded for each strain interval, the 20 mm x 20 mm with dividers offers 16 deformation results (2 x 2 grid in each of the 4 quadrants) and the 10 mm x 10 mm offers 9 deformation results.

A red marker which can be seen in Figure 42a and Figure 42c was used to conveniently locate the centre of the substrate when placed under the microscope. As tension was applied to the substrate, the markers correspondingly took strain and deformed. Using the measurement tools available on the Carl Zeiss Microscope software, measurements of the deformation lengths of each marker was recorded to calculate the strain for data processing.

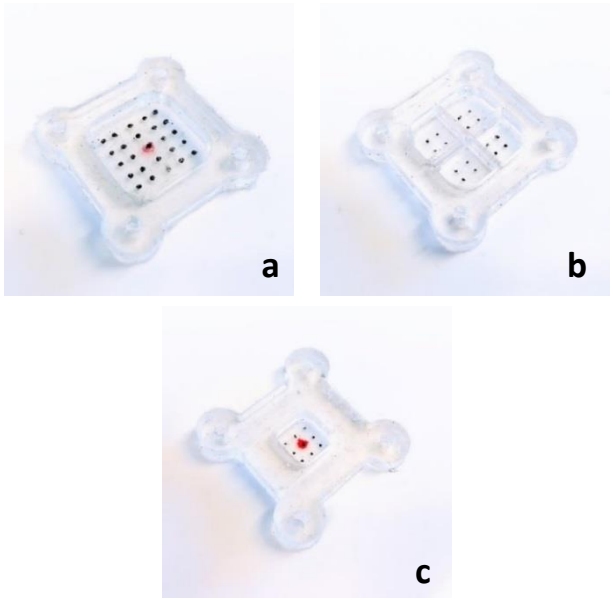

Figure 42: Photographed PDMS membranes marked with permanent marker in preparation for practical experimentation: (a) 20 mm x 20 mm membrane, (b) 20 mm x 20 mm membrane with dividers, (c) 10 mm x 10 mm membrane

The linear motor was set to travel at a speed of 5 mm/sec throughout the experimental procedure using the FMC Quick Access software. The 9 specimens followed the following procedure:

1. The PDMS membrane was loaded onto the device.
2. The device was loaded onto the microscope stage and held firmly by the designed microscope fitting, demonstrated in Figure 43.
3. The microscope was set to use at 2.5x magnification as it was the smallest objective available. At 2.5x magnification, individual markers were magnified to fit the field of view. Larger objectives did not suffice as the individual markers were too magnified and thus its entirety could not be viewed.
4. The microscope was set to perform a Tile Scan. This is a feature to capture the overview of the substrate. The Tile Scan feature automatically assembles an overview image from multiple smaller images. PDMS membranes are too large to be viewed through the 2.5x magnification objective. Figure 44 displays the overview image for each type of membrane at 0%, 10%, 20% and 30% strain. Each overview image of the PDMS membrane is made up by the stitching of the smaller images of the individual markers.
5. The Z-stack feature was enabled and it is commonly known as focus stacking. It is a digital image processing technique which combines multiple images taken at different focus distances. This results in an image with greater depth of field. The focus stacking feature was enabled due to the changes in focus distance from the objective to the membrane during stretch.
6. All membranes were stretched at intervals of: 0%, 2%, 5%, 10%, 15%, 20%, 25% and 30% respectively. At each strain interval, the membrane was viewed and an image of it at strain was captured. Figure 44 illustrates some of the captured images of the different membranes with tension load applied, captured by the microscope. Appendix A in section 6.1 illustrates the captured imaged results of the 9 specimens.
7. At each stretch interval, the image of the membrane is captured by the internal camera system offered by the microscope with Tile Scan and Z-Stack feature enabled.
8. After capturing the images, the horizontal deformation length (parallel to actuated load) of each mark of each substrate was recorded.
9. The data was recorded, input and analysed using Microsoft ® Excel.

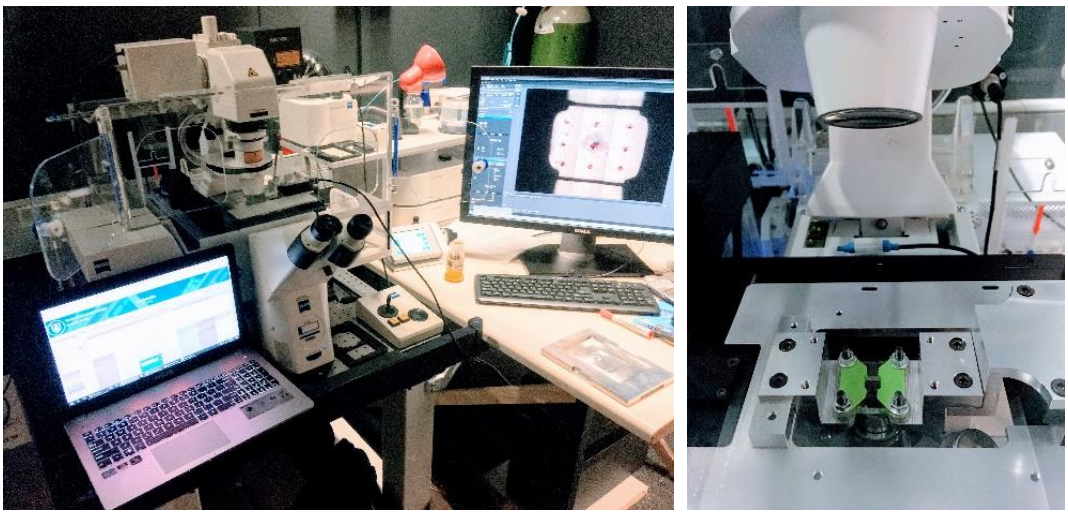

Figure 43: 10 mm x 10 mm PDMS membrane undergoing test procedure

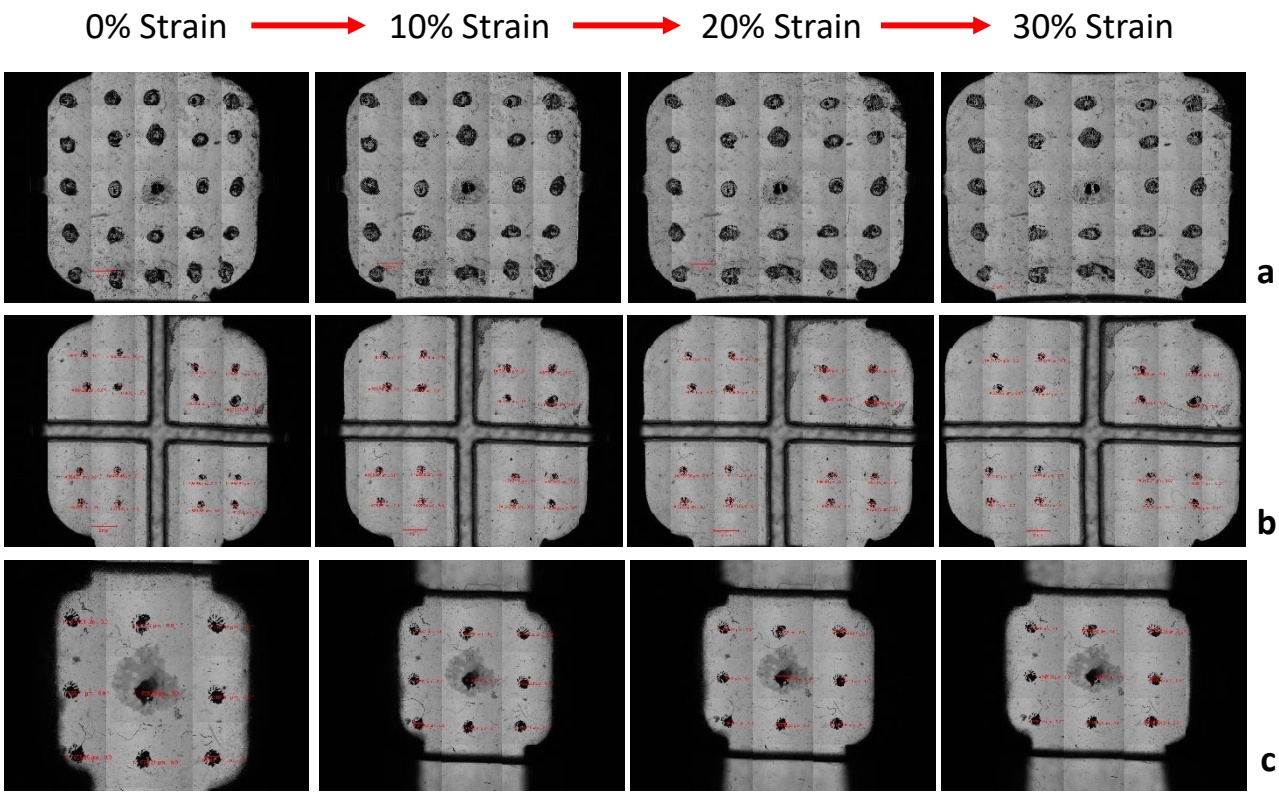

Figure 44: Photographed images of substrates at 0%, 10%, 20%, and 30% strain of: (a) 20 mm x 20 mm membrane with 5 x 5 matrix of non-biological marks, (b) 20 mm x 20 mm membrane with dividers with 2 x 2 matrix of non-biological markers in each quadrant, (c) 10 mm x 10 mm membrane with 3 x 3 matrix of non-biological marks

2.4 Data Analysis of Membrane Strain Measurements

The collected deformation lengths from the strain tests were further processed using Microsoft® Excel Spreadsheet to facilitate interpretation of recorded results for the data analysis procedure. The strain measurements were put into a format to show the strain distribution of each of the 9 specimens, similar to the grid layout of markers for each type of substrate seen in Figure 42. The matrix layouts, demonstrated in Figure 45 were used to show the change in strain for each marker of each substrate. For each strain interval, the deformed length of each marker from the captured images was divided over the original length of the marker to obtain the percentage of strain. The percentage values were input into the corresponding matrix cells. This procedure was completed for all 9 membranes.

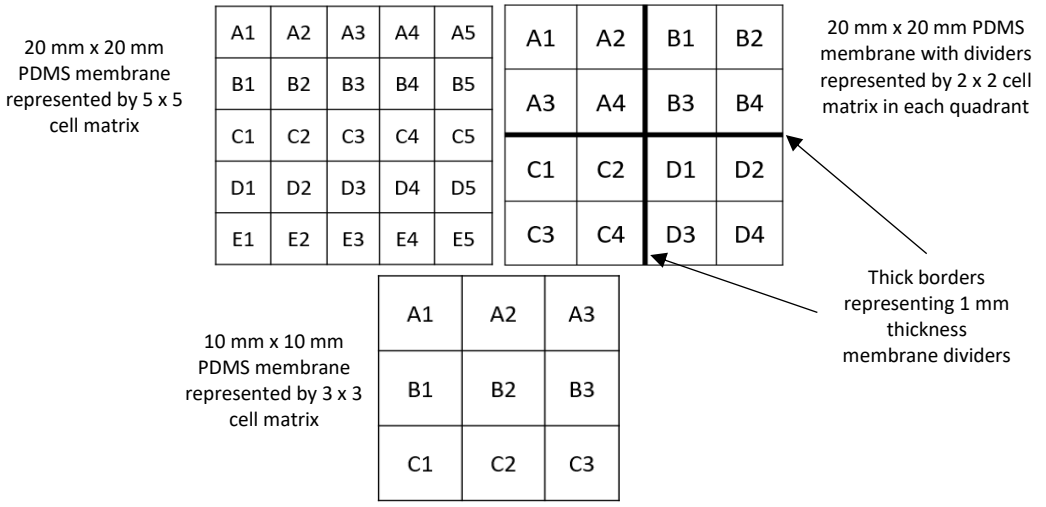

Figure 45: PDMS membranes represented as matrices in Microsoft® Excel for data processing

Each substrate type has 3 samples for the calculation of the mean deformation for each input strain. For each strain input, the corresponding cells of each matrix of the same type were averaged to generate the mean deformation matrix. Figure 46 demonstrates an example of the calculated mean deformation matrix along with the standard deviation of each measurement point of a particular membrane type under a specific induced strain. The standard deviation of each measurement point expresses how much the corresponding specimen cells differ from the mean cell value.

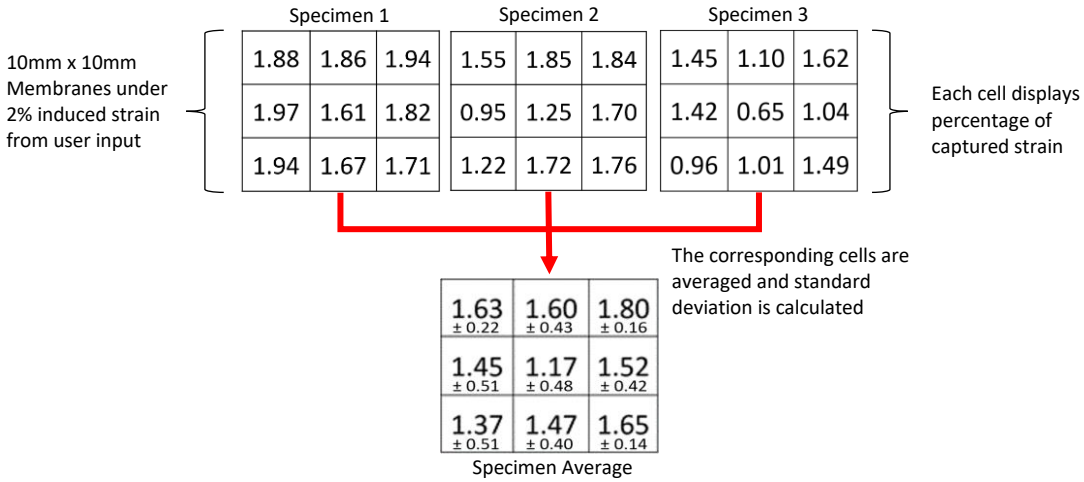

Figure 46: Average strain distribution and standard deviation captured of 10 mm x 10 mm membrane under 2% induced strain.

With the acquired mean deformation matrix of each substrate type at each induced strain, a visual system is used to show the strain distribution. The visual system ranks the cell values by using a colour scale; red representing the highest value, green representing the lowest values and yellow representing the middle percentile. An example of this is shown in Figure 47.

Mean deformation matrix of 20 mm x 20 mm membrane under 30% induced strain

25.30 ± 3.06	27.94 ± 1.07	28.46 ± 1.54	26.13 ± 3.12	23.83 ± 3.37
23.18 ± 1.32	26.98 ± 1.55	27.80 ± 3.41	29.45 ± 1.11	26.11 ± 3.90
27.35 ± 2.71	27.66 ± 1.37	29.63 ± 8.41	28.51 ± 1.45	27.37 ± 3.41
23.75 ± 2.83	28.98 ± 0.93	30.17 ± 0.92	28.83 ± 1.83	29.13 ± 2.45
28.02 ± 2.51	29.52 ± 0.52	28.95 ± 2.13	30.27 ± 1.36	25.54 ± 4.93

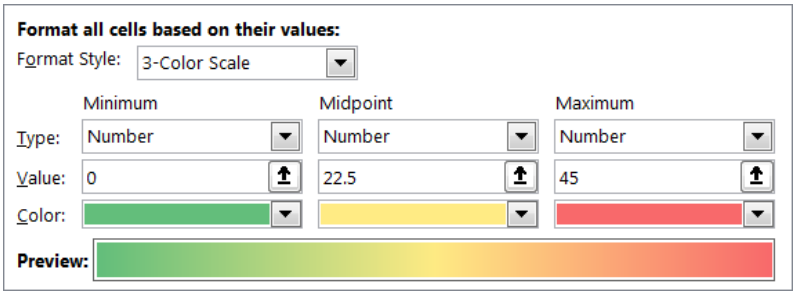

Colour Scales

Figure 47: Colour scale system to visualise strain distribution of mean deformation matrix of each substrate at each induced strain

2.5 Quantifying the Effectiveness of Device

After the processing of the captured data from the practical experimentation of the PDMS membranes, a method to quantify the effectiveness of the cell stretching device proceeded. The effectiveness of the device is the degree to which the strain output is successful in producing the desired strain result. To quantify the effectiveness of the device, three metrics were investigated: the repeatability of the device and membrane system, the uniformity of the strain field across the membrane and the accuracy of the output strain. A comparison between the acquired actual test data to the ideal situations was conducted.

The repeatability of the device-membrane system expresses the variation in the measurements between the specimens of the same type of PDMS membrane. The standard deviation in each measurement point in Figure 48 (highlighted in pink) demonstrates the consistency of the cell loading device upon different specimens of the 20 mm x 20 mm PDMS membrane at 30% induced strain. Good repeatability is indicated by a low standard deviation. The average standard deviation across all the measurement points is taken and used as an indicator for repeatability at that strain percentage, highlighted in yellow in Figure 48. This procedure is repeated for each induced strain percentage, subsequently, the average standard deviation across all the induced strains for each type of PDMS membrane shape is acquired. The average standard deviation across all the induced strains serves as an indicator for the repeatability effectiveness of a particular membrane type.

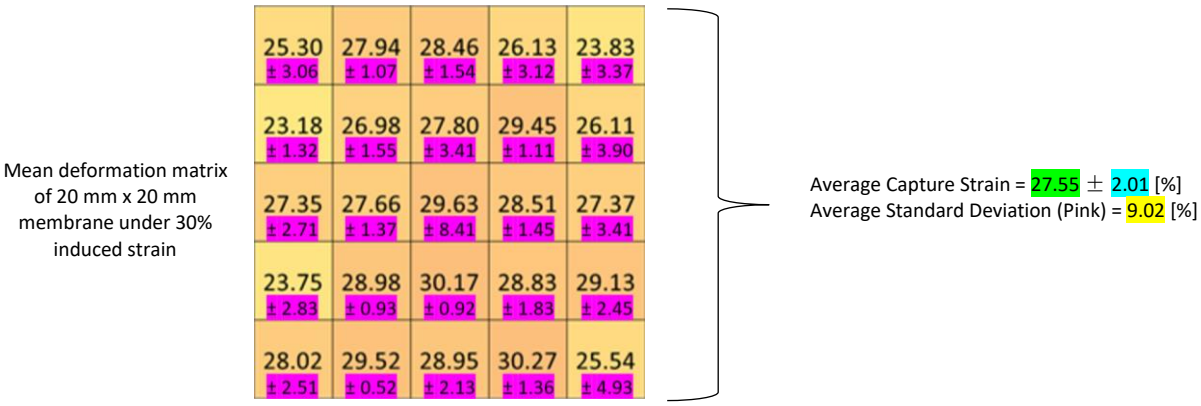

Figure 48: Obtained average strain capture from a 20 mm x 20 mm membrane under 30% induced strain

The uniformity of strain is described by the overall homogeneity of the measurement points (ink marks) of the PDMS membranes. An Ideal situation is whereby the field of the membrane stretches with the same strain across the entirety of the membrane. The standard deviation of the strain reports the information of the PDMS membrane uniformity and is acquired from the mean defamation matrix. The standard deviation for the 20 mm x 20 mm membrane at 30% induced strain is highlighted in blue in Figure 48.

The accuracy of the device indicates the quality of the strain output being correct to the input strain. Ideal situations are described as the output corresponding equally to the user input. If the user of the device inputs the desired strain and the output of the membrane has deformed by the input value, then this is described as an ideal situation. An ideal input-output strain graph is represented by $y = x$, where y represents the captured strain output and x represents the induced strain input.

The average strain captured for each induced strain was plotted in an input-output strain graph along with the ideal scenario. The average strain captured for each strain induced is calculated by obtaining the average of the cell values of the mean deformation matrix. Figure 48 is an example of calculating the average captured strain (highlighted in green) by averaging the cell values for a particular membrane type at a particular strain.

A graph showing the relationship between the induced strain and the average captured strain for each membrane type was plotted, illustrated in Figure 64, Figure 65 and Figure 66 in the chapter of Results.

A linear line of best fit method is used to best represent the average strain captured output from the strain induced input for each membrane type. The line of best fit was compared with the ideal strain to gauge the effectiveness of the device.

The ideal strain is expressed by,

$$y_{ideal} = x$$

and line of best fit for a certain type of membrane is expressed as:

$$y_{membrane\ type} = mx + c$$

where the constant $c = 0$, since there is no output strain for an input strain of 0. The gradient m quantifies the accuracy of the device for a particular PDMS membrane type, since it measures the proximity to the ideal gradient value of 1. The closer the measured gradient value m is to 1, the more accurate the device is for the associated PDMS membrane type.

2.6 Refinement to Improve Linear Actuator Accuracy

A gradient less than one in the ideal to actual stain plots indicates that the linear actuator is under stretching the PDMS membrane and needs to compensate by moving more than originally anticipated. The block diagram below in Figure 49 illustrates how the desired output strain is achieved from the compensated user input.

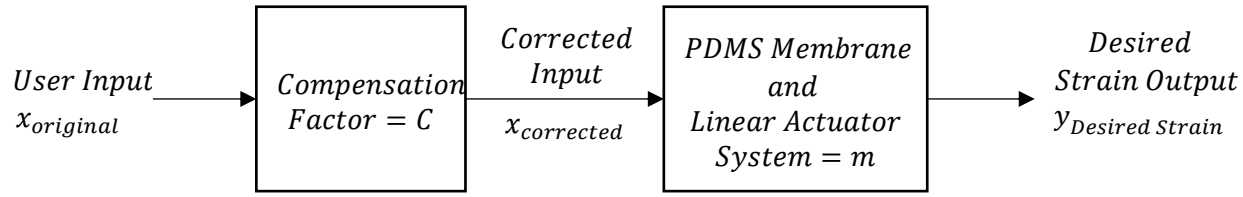

Figure 49: Open loop control system of device

From Figure 49, the desired output strain can be expressed as:

$$Desired\ Output\ Strain\ =\ m\ \times\ Compensation\ Factor\ \times\ User\ Input$$

$$y_{Desired\ Strain}\ =\ mCx_{original} \qquad (1)$$

By re-arranging equation (1), the compensation factor is expressed as:

$$C = \frac{y_{Desired\ Strain}}{mx_{original}} \qquad (2)$$

Since the desired strain output is defined by the user input,

$$y_{Desired\ Strain}\ =\ x_{original}$$

Thus, from equation *(2)*, the compensation factor is simplified to:

$$C = \frac{1}{m}$$

2.7 Finite Element Analysis of PDMS Membranes

Computational models of the PDMS membranes were constructed and simulated via Abaqus®, a finite element analysis (FEA) software. To perform computational modelling of the PDMS membranes, input data and assumptions such as; mechanical properties, constraints and boundary conditions are required. Thus, uniaxial tensile tests were performed to collect input data of mechanical properties of PDMS produced by curing 32 parts of silicone base to 1 part elastomer. Tests were performed using the Instron Universal Testing Machine to apply tensile strain on dog-bone shaped specimens. Mechanical property data of the PDMS material was acquired and further processed using MATLAB. The processed data was subsequently exported into Abaqus®. In Abaqus®, PDMS membranes models are generated and programmed to experience the various strains similar to that of the strain tests that the actual model experiences. A comparison between numerical results from FEA and experimental results are discussed in Chapter 4 to validate the computational models of the PDMS membranes

2.7.1 Experimental Determination of the Stress-Strain Curve of PDMS Membranes

To enable realistic FEA models, Abaqus® contains the feature of inputting acquired experimental data. A stress-strain curve typically described the mechanical properties of a material. The following describes the method of obtaining the stress and strain relationship of PDMS.

According to ASTM D412 test standards for vulcanized rubber and thermoplastic elastomers; dog-bone shaped specimens (Figure 50) were created and tensile tests were performed on an Instron 5544 Universal Testing Machine with a 500 N load cell (Instron, Norwood, USA). By performing tensile tests, the way in which the material will react to forces being applied in tension is quickly determined. Experimental conditions were set at room temperature and the crosshead velocity was set at 5 mm/sec, similar to that of the linear actuator of the tension system of the device created in this project. The mechanical properties were determined by processing the output files from the Instron Universal Testing System. The dog-bone shaped specimen was clamped in the grips of the Instron system at the specified gauge length of 25 mm, indicated in Figure 51.

The preparation of the PDMS specimens followed a similar procedure to that used for the membranes:

1. Ratio of 32:1 of elastomer to cross-linker was stirred and mixed for 5 min using a spatula.
2. Mixture was put into a vacuum to be degassed for 15 min.
3. Mixture was poured into a large petri dish.
4. Mixture was cured at 65 °C in an oven chamber for 2 hours
5. The produced PDMS was taken out the oven and left to cool to room temperature for 1 hour.
6. The Cured PDMS was carefully removed from the petri dish
7. Dog-bone shaped specimens were punched out using ASTM D412 Die Standards.

After the curing process, each dog-bone shaped PDMS specimen was mounted on the grips of Instron Universal Testing System. Dynamic stretching of 5 cycles to 30% tensile strain was performed as a pre-test to prepare the membranes for the ultimate tensile strength test. Stress and Strain data is computed and obtained via the Instron Universal Testing Machine and then collected.

Figure 50: Photographed images of dog-bone shaped PDMS 32:1 (ratio of elastomer base to cross-linker) specimens cut from ASTM D412 die

Figure 51: Uniaxial tensile testing of PDMS specimens on Instron universal testing system

The Instron Universal Testing Machine outputs stress-strain curves of each of the 10 specimens. Stress-strain data of each specimen was imported in MATLAB. The following procedure was conducted on MATLAB:

1. All stress-strain curves were extracted and plotted.
2. The mean stress-strain was calculated from the data of the 10 specimens.
3. The mean maximum of stress-strain was calculated.
4. The mean stress-strain curve and mean stress-strain maximum was plotted.
5. A best-fit curve was fitted and a power function was acquired.
6. A linear best-fit line was calculated from the initial segment of the mean stress-strain curve.
7. A linear best-fit line was calculated from the final segment of the mean stress-strain curve.

Figure 52 displays a graph plot of the relationship between tensile stress and strain of the individual specimens, the mean stress-strain curve, the power function that best fits the mean stress-strain

curve, and the maximum mean stress-strain value. The shortened mean stress-strain curve in Figure 52 is the mean stress-strain curve plotted till the maximum mean stress-strain value.

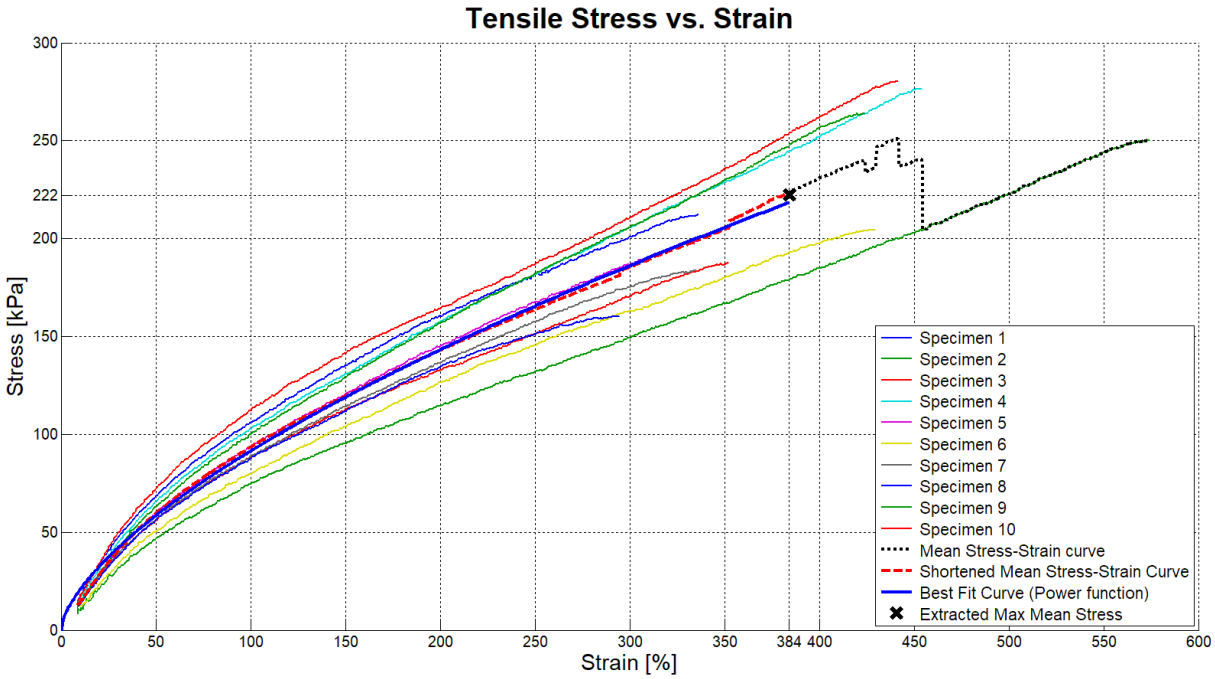

Figure 52: Tensile Stress vs. Strain plot of PDMS (32:1) specimens displaying mean stress-strain curve, best fit curve and max mean stress

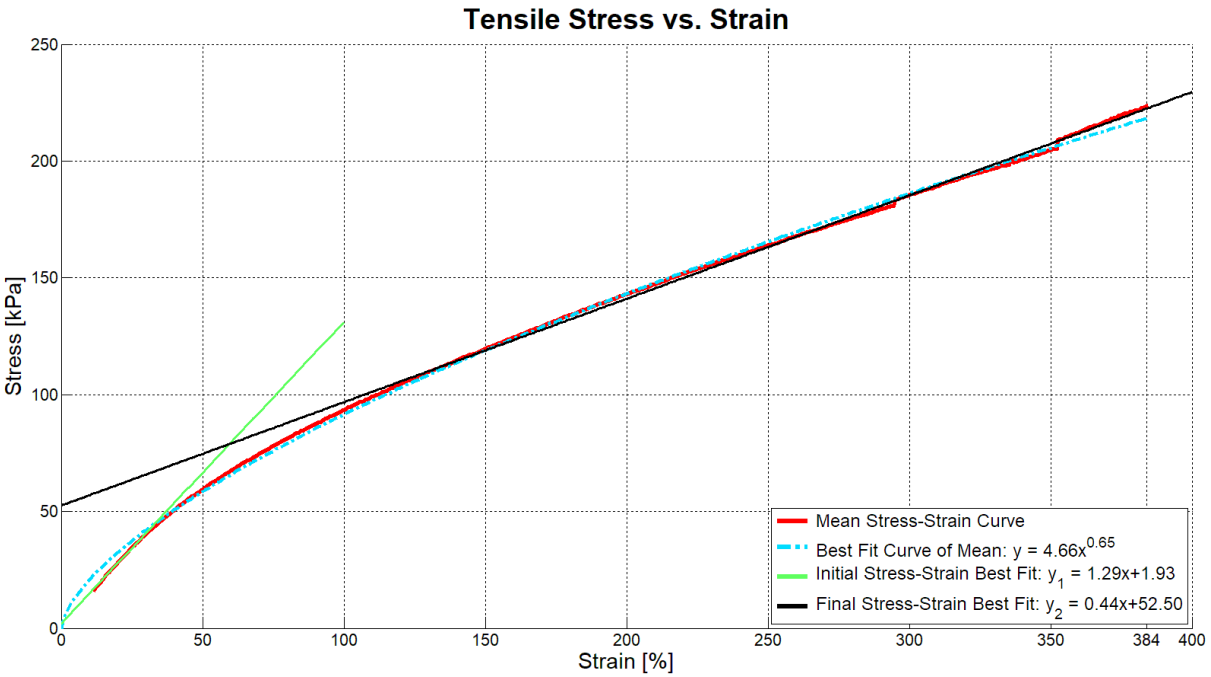

Figure 53: Tensile Stress vs. Strain plot of mean stress-strain curve, best-fit curve, initial stress-strain best fit and final stress-strain best fit

Using MATLAB, the calculated best fit for the mean stress-strain curve is:

$$y = 4.66x^{0.65}$$

The mean stress-strain curve is further processed to extract the elastic modulus, E. This process was achieved by generating a linear line of best fit in the initial segment of the mean stress-strain curve and another to the final segment of the mean stress-strain curve, as seen in Figure 53. The strain data points considered for the line of best fit for the initial segment were from 0% to 40% of the mean stress-strain curve, as within these strains are the strain values the PDMS membranes experienced in the practical experimentation. Strain data points from 150% to 384% were taken for the latter.

The linear best fit of the initial segment of the mean stress-strain curve is calculated to be:

$$y_1 = 1.29x + 1.93$$

Thus, from the gradient of y_1, the elastic modulus of PDMS composed with a ratio 32 parts of elastomer base to 1 part cross-linker is:

$$E = \frac{1.29\ kPa}{1\ \%} = 129\ kPa$$

The elastic modulus of y_1 describes the material properties of PDMS (32:1) for strains between 0% to 40%, i.e. the strains that the PDMS membranes experienced during the testing procedure.

The linear best fit of the final segment of the mean stress-strain curve is calculated to be:

$$y_2 = 0.44x + 52.50$$

From the gradient of y_2, the elastic modulus of PDMS is:

$$E = \frac{0.44\ kPa}{1\ \%} = 44\ kPa$$

The elastic modulus of y_2 describes the material properties of PDMS (32:1) for strains from 150% to 384%.

2.7.2 Data Input and Assumptions for the Computational Model of PDMS Membranes

2.7.2.1 Membrane Geometries & Finite Element Meshes

The global membrane shape in the Abaqus® software takes the imported membrane models from Solidworks®. The geometries of the membrane models in Abaqus® are defined as a solid deformable 3D part with material properties of PDMS (32:1), a hyperelastic material. Material property data of the PDMS (32:1) were acquired from the experimental determination of the mean stress-strain curve described in Figure 53.

The default hexagonal shaped mesh was unable to be applied as Abaqus® recognises the membrane models as complex geometries; thus, a tetrahedral shaped element mesh was selected for the 3 membrane types as shown in Figure 54. The approximate global mesh size for the 20 mm x 20 mm membranes in Figure 54 a and b is 1.64 mm. For the 10 mm x 10 mm membrane, indicated in Figure 54 c, 0.8 mm is allocated as the approximate global mesh size, since the cell culture area is smaller. A smaller global mesh size for the 10 mm x 10 mm membrane will produce a number of elements across

the cell culture area similar to that of the 20 mm x 20 mm membranes to provide a similar level of detail in the predicted strain distribution.

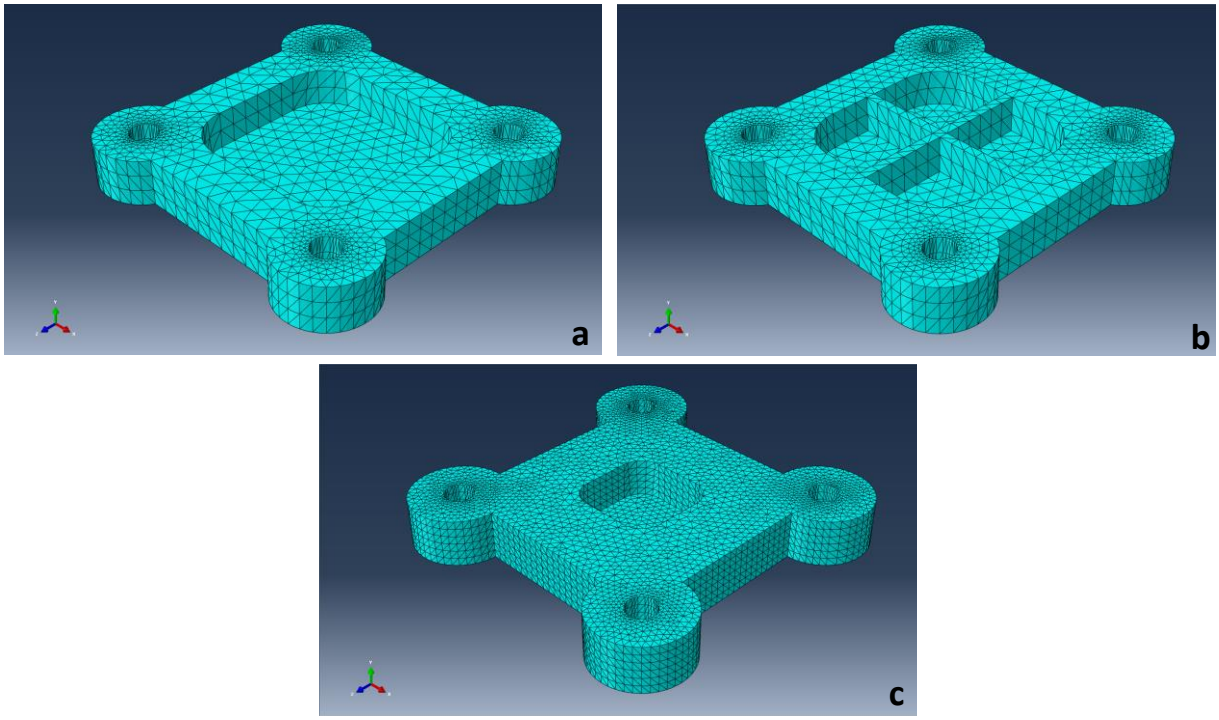

Figure 54: FEA meshing of membrane models

2.7.2.2 Constitutive Modelling

Data points were obtained from the mean stress-strain curve of Figure 53 from MATLAB and imported into the material model of Abaqus®. The mean stress-strain curve data presents Abaqus® with the material properties of PDMS acquired from practical experimentation. This enables Abaqus® to output practical-like simulations.

A Neo-Hookean hyperelastic material model was selected under the Strain Energy Potential field. A Poisson's ratio of 0.49 was used, since a hyperelastic material is nearly incompressible. The stress-strain data was fitted to the Neo-Hookean hyperelastic material model and then further evaluated to derive the hyperelastic material constants as seen in Figure 55. The evaluation allows one to view the behaviour predicted by a hyperelastic or viscoelastic material and that allows one to choose a suitable material formulation. Figure 55 indicates that the Neo-Hookean material model fits well with the test data, from strain values of 0.1 to 0.9. The Neo-Hookean model is suitable for the initial range of cross-linked polymer materials and is generally known that it does not predict accurate phenomena at large strains (Kim et al. 2012). The strain energy density function for an incompressible Neo-Hookean material is defined as:

$$W = C_1(I_1 - 3)$$

where C_1 is defined as the material constant and I_1 is defined as the first invariant of the left Cauchy-Green deformation tensor. From the evaluation of the PDMS material of mixture ratio 32 parts of polymer to 1 part cross-linker, the material constant C_1 was calculated to be:

$$C_1 = 28131.36\, J/m^2$$

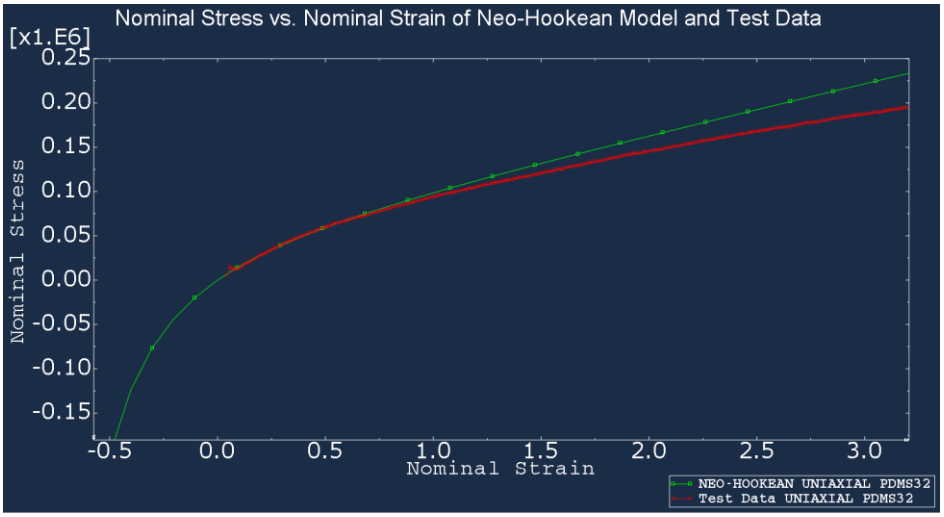

Figure 55: Evaluation of Neo-Hookean hyperelastic material model

2.7.2.3 Boundary Conditions and Loading

Since the model takes into account the material non-linearity (hyperelastic material model), the FEM model was solved implicitly. Boundary conditions were implemented to approximate the experimentation setup, indicated in Figure 56. One end of the membrane was fixated and the opposite end was applied with a displacement till the desired strain was reached. The non-fixated end was programmed to displace at a velocity of 5 mm/s. The desired strain presents a measurement for the opposite end to displace. This displacement measurement divided by the velocity produces the time period for the strain simulation to run till the user-defined strain percentage is met.

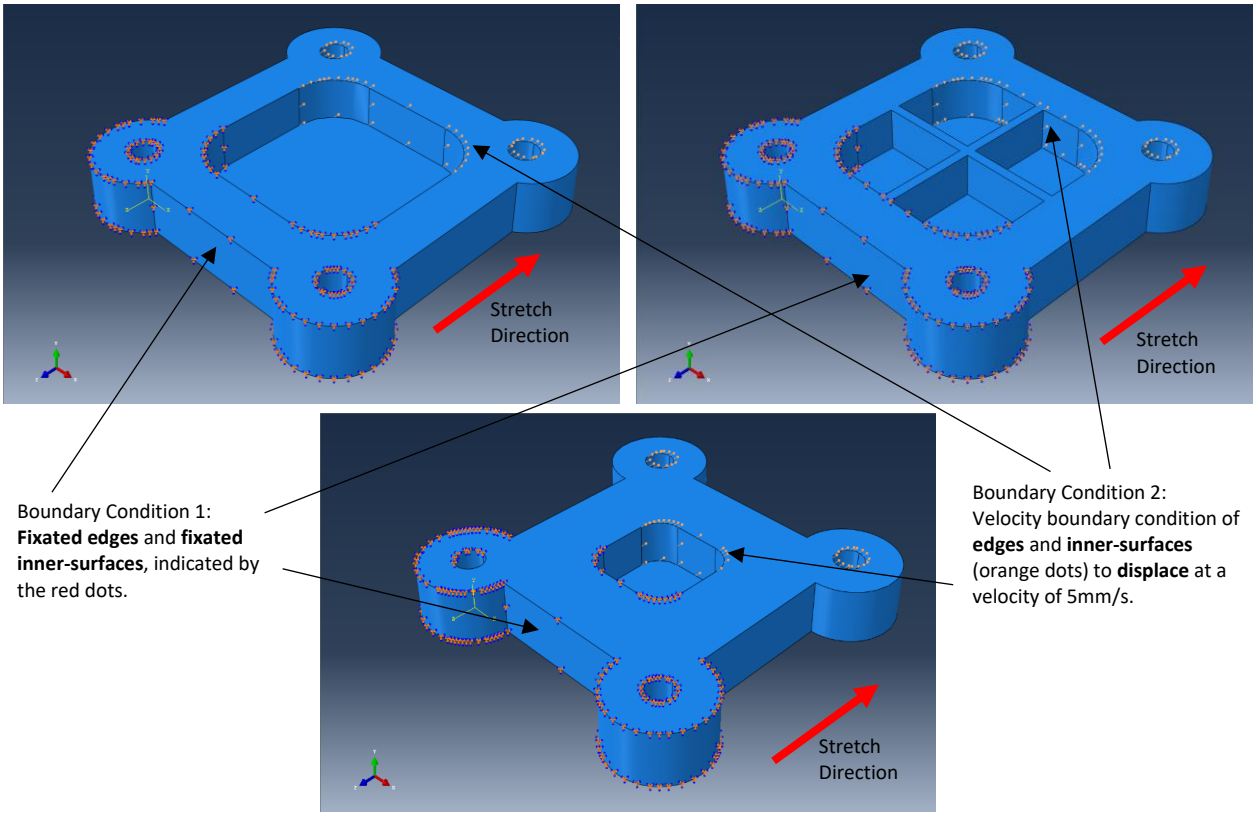

Figure 56: Setup of boundary conditions for FEA: boundary condition were setup in the similar arrangement to the experimentation setup. Inner-surfaces and edges of the model were bound.

2.7.2.4 Data Capture and Analysis

Simulations of each substrate were run until strains of 2%, 5%, 10%, 15%, 20%, 25% and 30% were achieved. The logarithmic strain component was requested as the output field variable during the simulation of stretching of the various membranes. Data were captured and analysed by using the colour contour plots to examine the strain homogeneity of the cell culture area, and by averaging the node selection of the cell culture area of the model, the average captured strain output of the FEA was calculated. An example is shown in Figure 57.

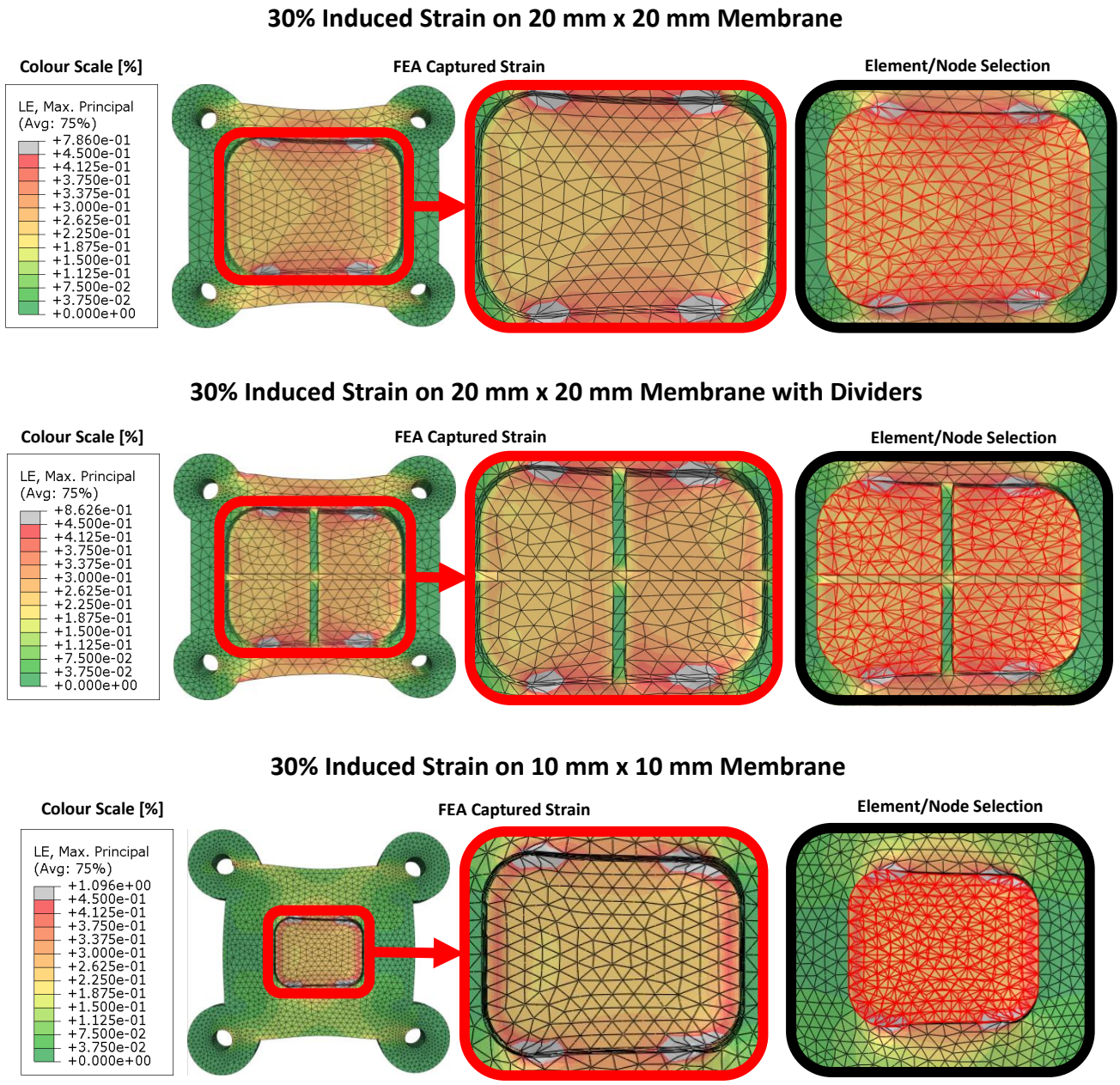

Figure 57: Node selection of 20 mm x 20 mm membrane, 20 mm x 20 mm membrane with dividers and 10 mm x 10 mm membrane at 30% induced strain

3 Results and Discussion

The following chapter reveals the prototype of the manufactured loading device, the manufactured PDMS membranes, and the acquired data of the strain tests of the various types of PDMS membranes from the experimentation and computational modelling. Data analysis is also discussed in this chapter to investigate the performance of the designed device and the computational models.

The first section describes and displays the manufactured prototype device and membrane moulds. The section further provides the curing process of the PDMS membranes.

Methods to indicate the effectiveness of the designed device is described in Section 3.2. The effectiveness of the stretching device describes its ability to produce the desired strain result. The effectiveness is gauged by the uniformity of the strain field and the accuracy of the strain field. Once the effectiveness of the loading device has been quantified, the compensation steps to improve the effectiveness of the device are computed, which is presented in Section 3.3.

In Section 2.4, further data analysis was performed to determine the validity of the computational model. Numerical data validation includes the comparison between the numerical results acquired from FEA software and results recorded from practical experimentation. The stretch behaviour pattern results of the FEA and practical experimentation tests are compared in this chapter. If FEA results are similar to the practical experimentation results, then it can be concluded that the computational model of the PDMS membranes are valid. The following diagrams, Figure 71, Figure 72 and Figure 73, display the results of the acquired strain distribution at 2%, 15% and 30% induced strain of all PDMS membrane types. The strain distribution colour scale refers to both the FEA model and practical experimentation model.

3.1 Loading Device and Membranes

3.1.1 Prototype of Loading Device

Models designed with the Solidworks® CAD software were manufactured at the UCT Mechanical Engineering workshop. The metal components were manufactured with 6061 Aluminium Alloy, due to its high resistance to corrosion, since the cell manipulation device can be subjected to various kinds of liquids and solutions for cellular research. 6061 Aluminium Alloy is one of the most common alloys for general purpose use because of its cost-effectiveness, high strength and suitable workability. The material is relatively soft and durable, allowing it to be tolerable for the cutting tools when machining the device components. Figure 58 displays the manufactured mechanical cell loading device in the mode of tension.

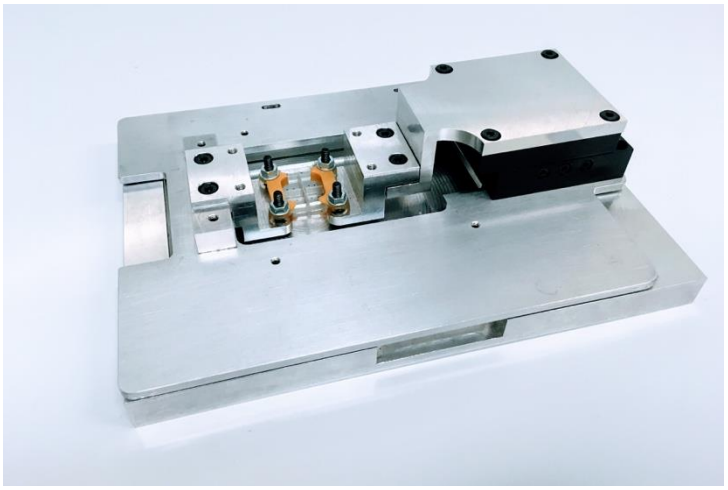

Figure 58: Photograph of manufactured prototype of mechanical cell loading device demonstrating tension

The same manufacturing process of the tension loading system was used for the compression system and shear system, displayed in Figure 59 and Figure 60 respectively. The cell well of the compression and shear system is manufactured with polypropylene material type.

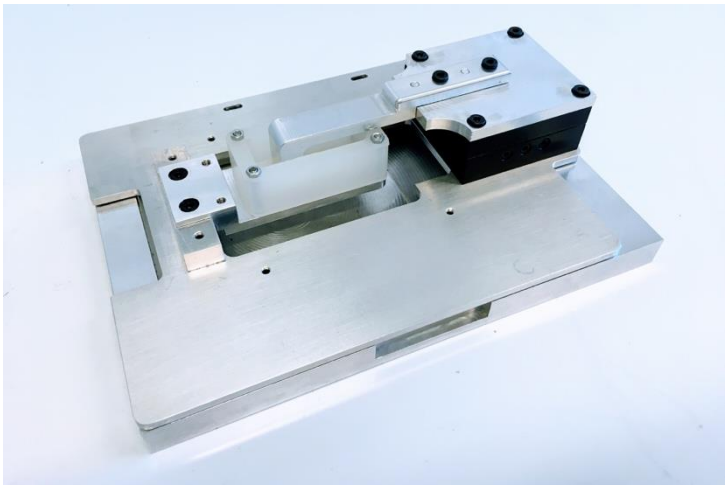

Figure 59: Photograph of manufactured prototype of mechanical cell loading device demonstrating compression

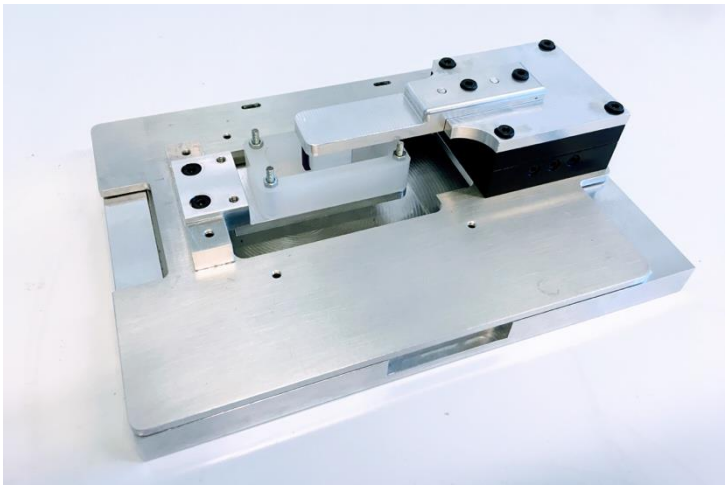

Figure 60: Photograph of manufactured prototype of mechanical cell loading device demonstrating shear

3.1.2 Prototype of PDMS Membranes

Mould negative, as seen in Figure 61, are manufactured with ABS plastic, from the process of 3D printing. 3D printing was the preferred choice of manufacturing due to its rapidness of delivery.

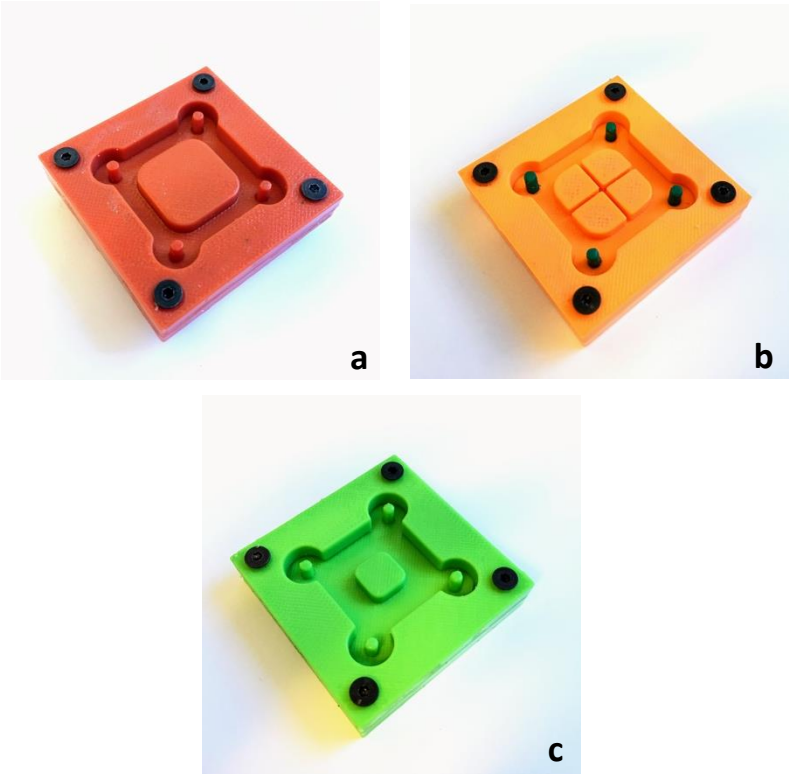

Figure 61: Photographed 3D printed mould negatives for PDMS substrates

After the manufacturing of mould negatives, the moulding process then followed. From collaborator protocol, the PDMS membranes were made by mixing the weight ratio of 32 parts of Sylgard 184 PDMS elastomer (the silicone base) to 1 part of cross-linker (the curing agent). These two components for the PDMS substrates were supplied by Dow Corning, a leading global supplier of silicone products. A ratio of 32 to 1 is used to create qualities such as a highly stretchable and soft membrane to

withstand the tensile loads. The curing process of the PDMS substrates followed a procedure to ensure all resulting moulds would have consistent mechanical behaviour. The process was as follows:

1. Sylgard 184 PDMS elastomer and cross-linker were mixed using a weight ratio of 32:1 (elastomer to cross-linker). The cross-linker was added to the elastomer and mixed well to create a homogenous distribution of the cross-linker. A 5-minute timer was set for this process and a spatula was used for stirring to ensure even mixing.
2. The mixture was degassed under vacuum until all the bubbles disappeared. Typically, this is a 5 to 10 min process. During the mixing, air bubbles were trapped in the mixture. The pre-polymer and hardener mixture was put into a vacuum and degassed for 15 min.
3. PDMS mixture was poured into the 9 moulds (3 of each type of substrate for procedure of testing)
4. Moulds were placed into the preheated oven at 65 °C for 2 hours
5. After 1 hour of cooling, the PDMS moulds were taken out of their casts

Figure 62 displays the cured PDMS membranes of weight ratio 32 parts of Sylgard 184 PDMS elastomer to 1 part of cross-linker.

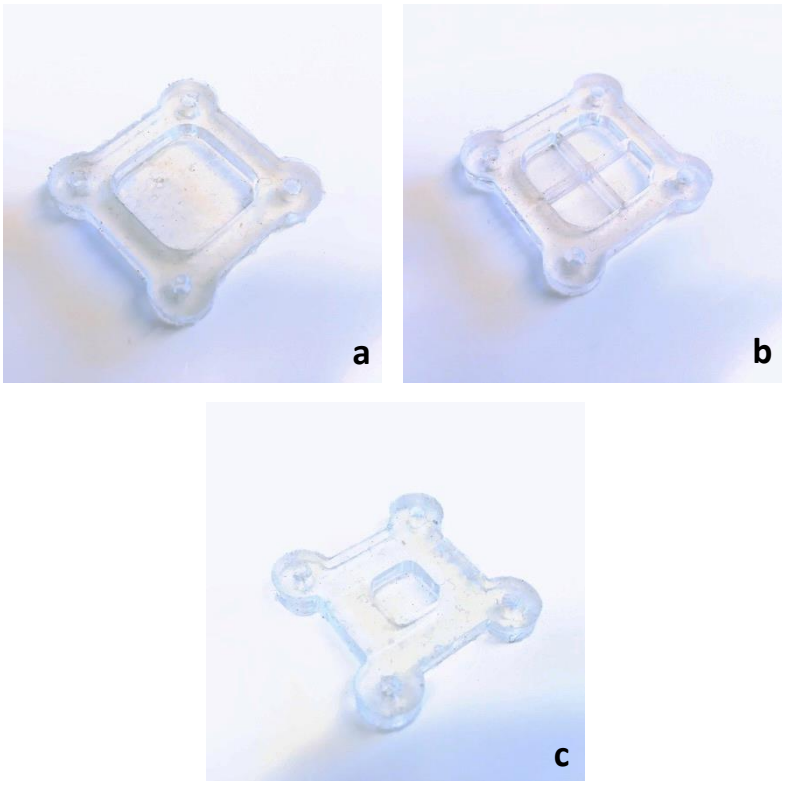

Figure 62: Photographed cast PDMS membranes of 32:1 for tension system: (a) 20 mm x 20 mm membrane, (b) 20 mm x 20 mm membrane with dividers, (c) 10 mm x 10 mm membrane

3.2 Quantification of the Effectiveness of Device

To quantify the effectiveness of the device, three metrics were investigated: the repeatability of the system of device and membrane, the uniformity of the strain field across the membrane and the accuracy of the output strain. The uniformity of strain refers to the homogeneity of the strain throughout the PDMS membrane. The accuracy refers to the degree to which the measured strain conforms to the ideal strain.

3.2.1 Repeatability of Test System Comprising of Device and Membrane

As mentioned in Section 2.5, repeatability is the ability of the device-membrane system to constantly achieve a certain strain for a specific user input across the multiple specimens for the same membrane type. The indicator for repeatability, as discussed in Section 2.5, is the standard deviation between the strain results for each specimen of each PDMS membrane type. The repeatability of the system is summarised in Table 1.

Table 1: Repeatability indicator for the different types of PDMS membrane shapes

Repeatability Indicator			
	Average Standard Deviation between Specimens for each Membrane Type		
Induced Strain	**20mm x20mm**	**20mm x 20mm with Dividers**	**10 mm x 10 mm**
2%	12%	18%	28%
5%	9%	18%	30%
10%	9%	16%	30%
15%	8%	23%	30%
20%	9%	15%	28%
25%	9%	17%	27%
30%	9%	16%	24%
Average	9%	18%	28%

Table 1 indicates that the 20 mm x 20 mm PDMS membrane specimens offer the greatest repeatability, as it has the lowest standard deviation between its specimens. The 10 mm x 10 mm membrane specimens showcase the poorest repeatability as it has the highest standard deviation between its specimens. The poor repeatability is not due to the inconsistencies between the specimens as they are moulded from the same homogenous PDMS batch. The poor repeatability is due to the inconsistency of the loading device. This is discussed in Section 3.3.1.

3.2.2 Uniformity of the Strain Field

The strain field uniformity is assessed by calculating the standard deviation of the mean deformation matrix of each type of PDMS membrane for each strain interval as discussed in Section 2.5.

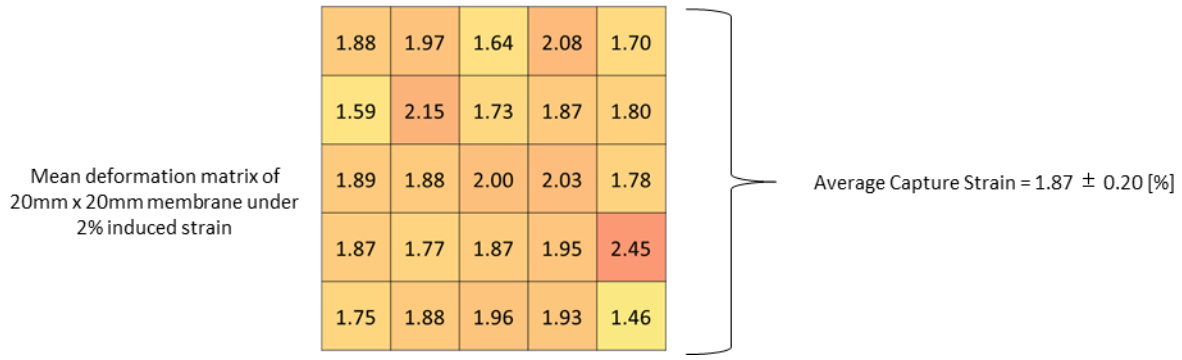

Figure 63: Mean deformation matrix of 20 mm x 20 mm PDMS membrane at 2% induced strain

From Figure 63, it can be seen that there is non-uniformity across the PDMS membrane. To quantify the percentage non-uniformity, the average strain across all the measurement points was calculated as well as the standard deviation of the average strain. The percentage non-uniformity calculated for the 20 mm x 20 mm PDMS membrane deformation matrix at 2% strain is

$$Avg\ Strain\ at\ 2\%\ Induced\ Strain = 1.87\%$$

$$Standard\ Deviation = 0.2\%$$

$$Percentage\ non\ uniformity = \frac{Standard\ Deviation}{Avg\ Strain} = 11\%$$

This method was used for all strain results. Table 2 summarizes the results:

Table 2: Percentage Non-uniformity of the different types of PDMS membranes

	Strain Field Non-uniformity		
Induced Strain	**20 mm x 20 mm**	**20 mm x 20 mm with Dividers**	**10 mm x 10 mm**
2%	10%	24%	12%
5%	7%	20%	9%
10%	8%	11%	10%
15%	7%	19%	9%
20%	7%	12%	11%
25%	7%	14%	11%
30%	7%	13%	12%
Average	8%	16%	11%

From Table 2, demonstrates that the 20 mm x 20 mm membrane with dividers has the greatest percentage non-uniformity. This is possibly due to the dividers influencing the strain field throughout the membrane.

3.2.3 Accuracy of the Strain Field

In Figure 64, Figure 65 and Figure 66, the strain captured from each specimen and the average strain captured of the three types of samples are plotted against the induced strain. The induced strain is the input strain applied by the linear actuator.

Figure 64, Figure 65 and Figure 66 provide a comparison between the effectiveness of the device and the ideal strain effect. As mentioned in the previous chapter, the gradient of the average captured strain plot showcases the accuracy of the designed device to induce strain on the particular PDMS membrane type. The gradient values for each PDMS membrane type are shown in their respective plots below.

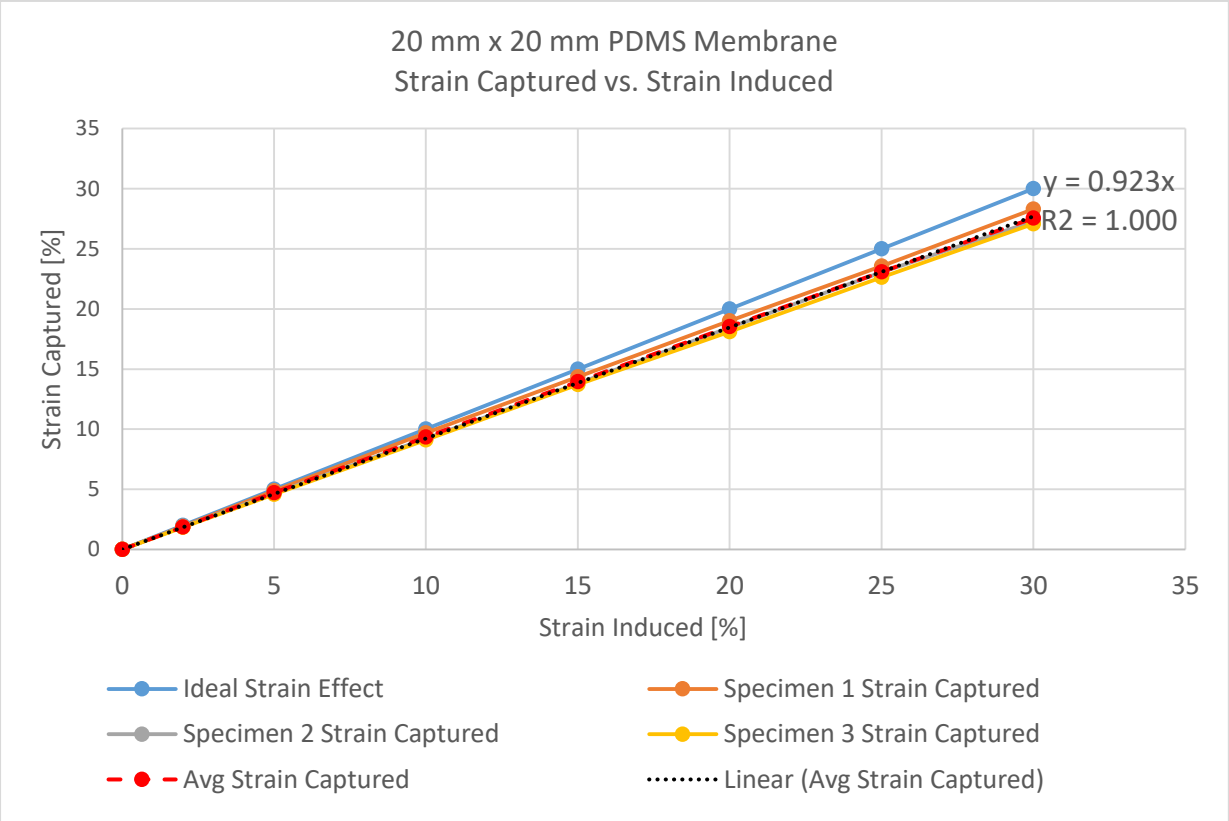

Figure 64: Strain Captured vs. Strain Induced graph plot of ideal strain effect, individual specimens, average of the specimens and linear best fit of 20 mm x 20 mm PDMS membrane

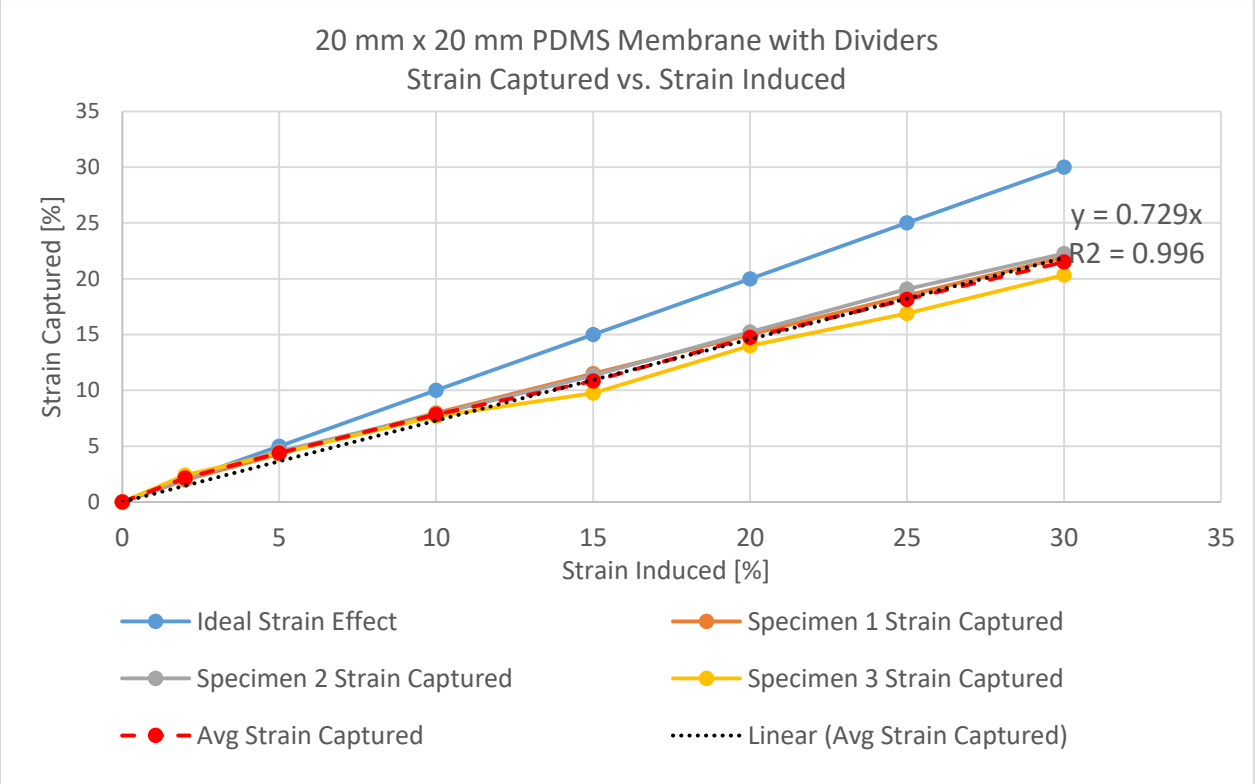

Figure 65: Strain Captured vs. Strain Induced graph plot of ideal strain effect, individual specimens, average of the specimens and linear best fit of 20 mm x 20 mm PDMS membrane with dividers

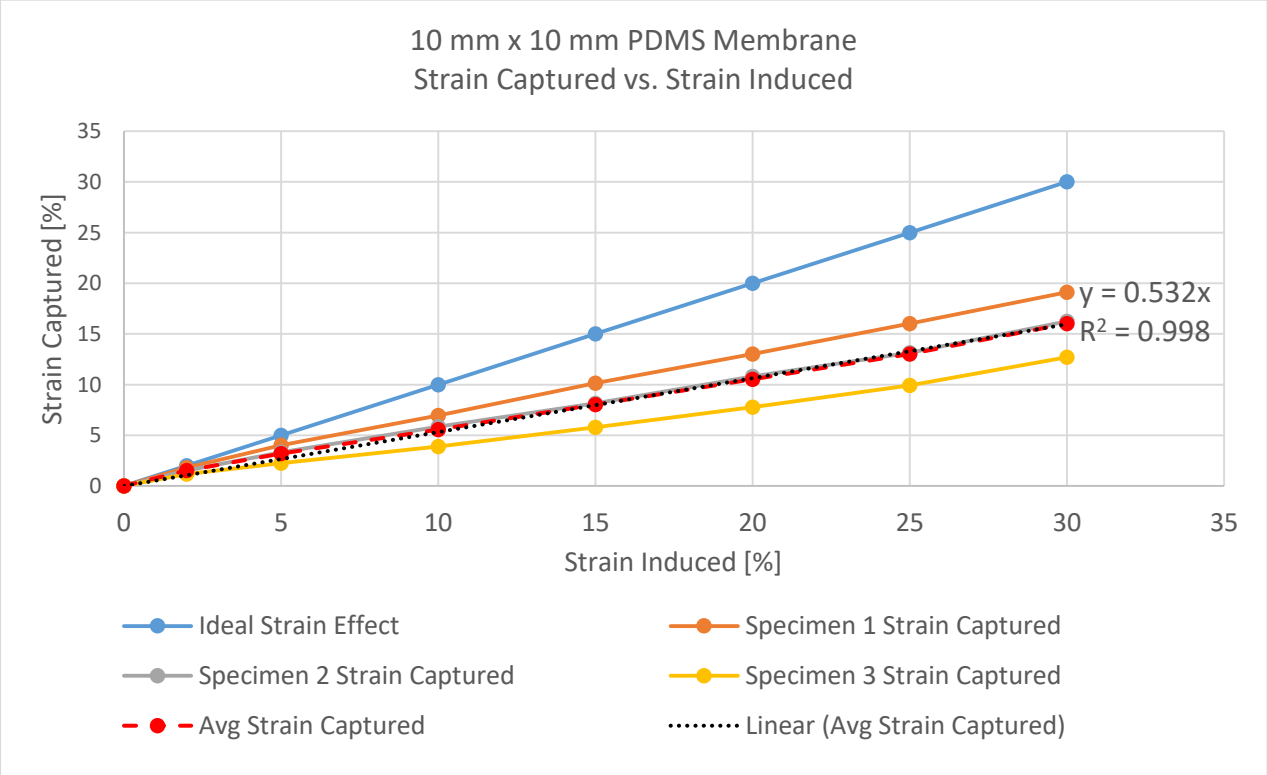

Figure 66: Strain Captured vs. Strain Induced graph plot of ideal strain effect, individual specimens, average of the specimens and linear best fit of 10 mm x 10 mm PDMS membrane

The gradients of the above three plots are summarised in Table 3 below for ease of reference.

Table 3: Accuracy of designed device on various types of PDMS membrane types

Membrane Type	Gradient	Accuracy
20 mm x 20 mm	0.923	92.3%
20 mm x 20 mm with Dividers	0.729	72.9%
10 mm x 10 mm	0.532	53.2%

The 20 mm x 20 mm PDMS membrane shows to be the most accurate out of the three membrane types, with the 10 mm x 10 mm being the least accurate. The linear actuator of the cell loading device displaces by the exact amount input by the user. Thus, any discrepancy between the resultant output strain and the user input strain is due to an error in the gripping component as it is the direct interface between the actuator and the membrane and therefore responsible for translating the displacement from the linear actuator to the PDMS membrane. The improvement in the gripping component is described in the following section.

3.3 Improvement of the Effectiveness of Device

Increased effectiveness of the device can be achieved by improving the repeatability, uniformity and accuracy. The effectiveness of the system can be improved by changing the membrane attachment technique. The accuracy can be further refined by over-driving the linear motor based on a calculated compensation factor.

3.3.1 Limited Repeatability, Uniformity and Accuracy due to Membrane Attachment

The captured results indicate required changes to improve the effectiveness of the device on the membranes. From the analysis of the results, improvements to the gripping components are suggested. The different clamps of various lengths for the different types of substrate are shown in Figure 67.

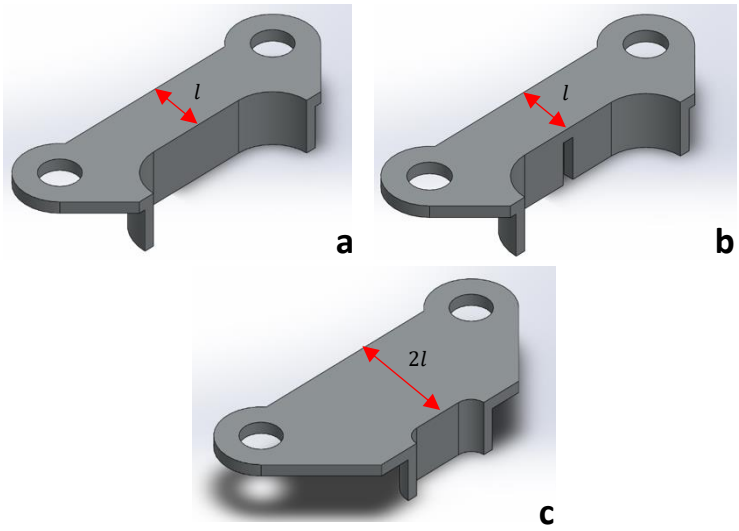

Figure 67: Existing clamp design for the various types of PDMS membrane demonstrating their different lengths: (a) 20 mm x 20 mm PDMS membrane clamp, (b) clamp with orifice for walls of 20 mm x 20 mm membrane with dividers, (c) 10 mm x 10 mm PDMS membrane clamp

The method of securing the PDMS membrane is of a M3 nut fastening the clamp onto the screw. The tightening of the nut onto the screw varies, since the PDMS membrane that is assembled in between is of a viscoelastic material. Since it is a viscoelastic material, PDMS is compressible. The varying of the tightness of the nut leads to a changing angular position of the clamp. The more the M3 nut is tightened, the greater the angle between clamp and cell culture area of the PDMS membrane becomes, as shown in Figure 68.

The changing of angular position of the clamp is of a concern as the clamp is unable to completely grapple the edges of the PDMS membrane, which causes the area for cell culture to strain less as the induced input strain, thus giving reason to the low accuracy score of 53.2%. The different variations of the tightness of the M3 nut causing different fixation of the holder is expected to cause the measurement irregularities, in particular for the 10 mm x 10 mm PDMS membranes, observed in Figure 66.

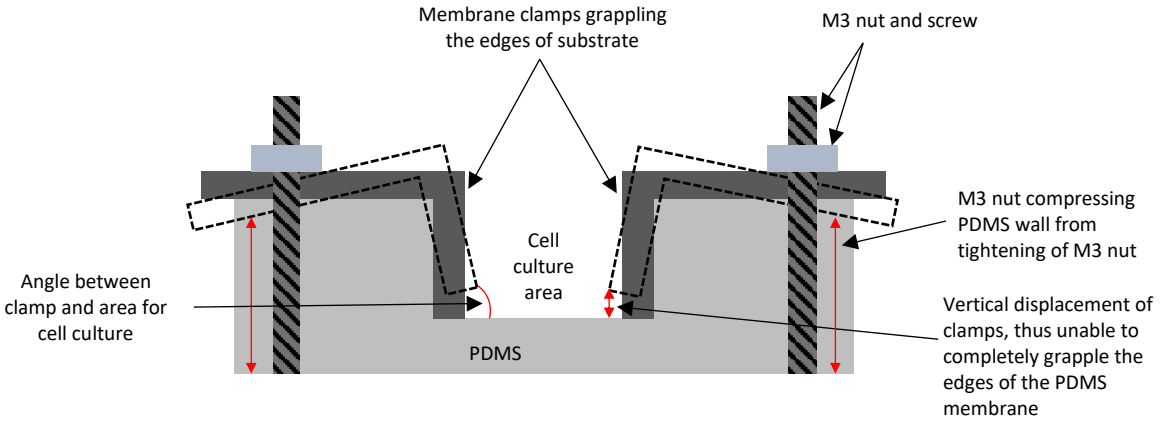

Figure 68: 10 mm x 10 mm PDMS membrane fault-finding

The difference between the measured strain and input strain value with the 20 mm x 20 mm PDMS membrane is small. The gradient value is 0.923, indicating high accuracy of the designed device on this particular PDMS membrane as seen in Figure 64. The effect of the varying of tightness of the M3 nut on the 20 mm x 20 mm PDMS membrane is of a minor concern compared to that of the 10 mm x 10 mm PDMS membrane. This is due to the shorter length of the clamp, illustrated in Figure 69.

The angular displacement for both PDMS membrane cases are the same. However, when the clamp length is shortened, the vertical displacement of the grappling component of the clamp along the edge is less. Thus, comparing the 10 mm x 10 mm PDMS membrane to the 20 mm x 20 mm PDMS membrane; for the same angular displacement, the vertical displacement of the grappling component of the clamp along the edge of the cell culture area of the PDMS membrane is less in the 20 mm x 20 mm PDMS membrane due to the shorter clamp length. This concept is illustrated in Figure 70.

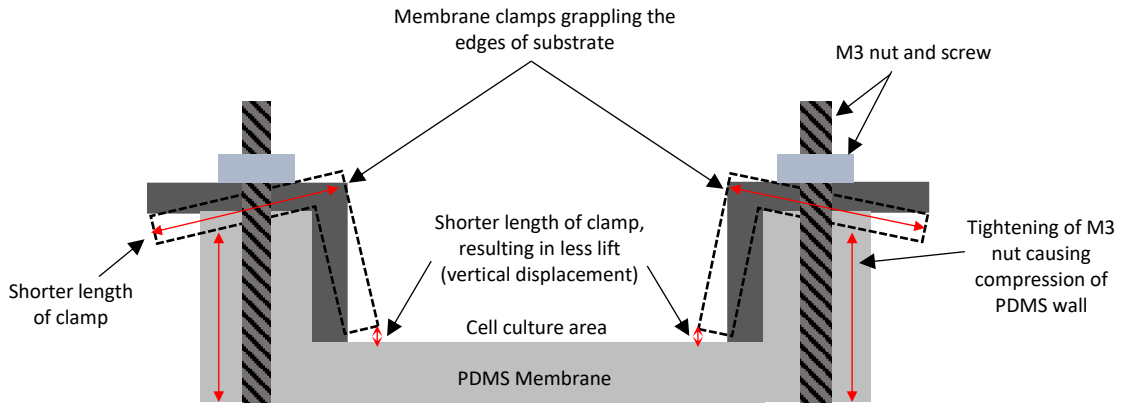

Figure 69: Cross-section of clamp setup of 20 mm x 20 mm membrane demonstrating that shorter length of clamp results in less effects from the tightness of M3 nut

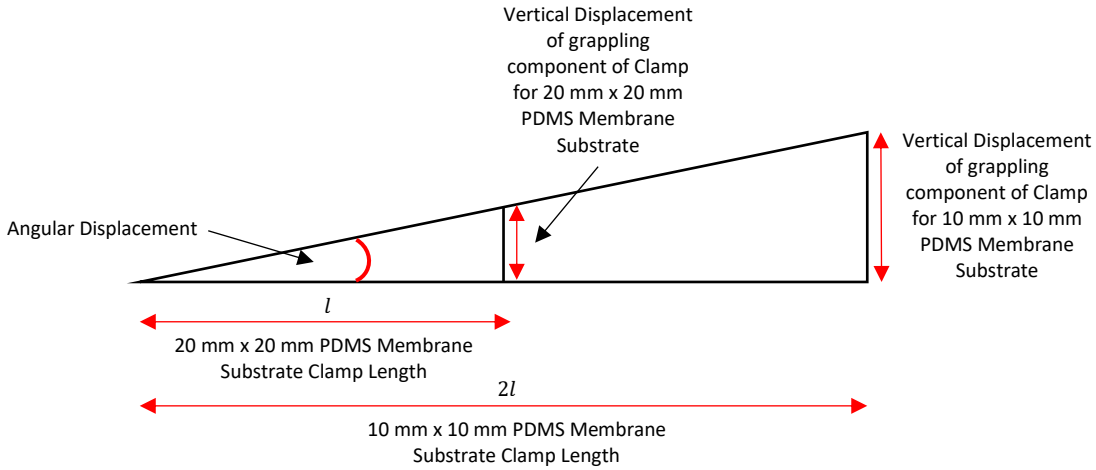

Figure 70: Demonstration of difference in vertical displacements of grappling components of clamps for 20 mm x 20 mm and 10 mm x 10 mm PDMS membranes

Similar clamps from the 20 mm x 20 mm PDMS membrane were used for the 20 mm x 20 mm PDMS membrane with dividers. An extruded cut was applied to the clamp to provide an orifice for the 1 mm thick divider to pass through as illustrated in Figure 67b. The gradient value of the 20 mm x 20 mm PDMS membrane with the 1 mm thick dividers falls between the other two types of PDMS membranes. The 1mm thick divider walls is the only difference that separates the two 20 mm x 20 mm PDMS membranes. Thus, the walls can be isolated as the cause for the decrease in strain effectiveness between the two types of 20 mm x 20 mm PDMS membranes. The acquired accuracy of the 20 mm x 20 mm PDMS membrane with dividers is 72.9%. The difference in effectiveness between the two types of 20 mm x 20 mm PDMS membranes is due to the divider absorbing some of the strain energy from the input source. With the proper gripping technique, as mentioned above, this issue should be resolved due to direct translation of the linear actuator's displacement to the PDMS membrane.

3.3.2 Compensation Factor Calculation (Improving Accuracy)

From the methodology section of quantifying the effectiveness of the designed device, it was seen that the PDMS membrane was under-strained. In order to strain the PMDS membrane correctly, the linear actuator has to be over-driven by a calculated compensation factor. The compensation factor is quantified by the following expression, which is derived in section 2.5:

$$C = \frac{1}{m}$$

The gradient value for the 20 mm x 20 mm PDMS membrane obtained from Table 3

The gradients of the above three plots are summarised in Table 3 below for ease of reference.

Table 3 in Section 3.2.3, denoted as m_{20} is:

$$m_{20} = 0.923$$

The compensation factor for the 20 mm x 20 mm PDMS membrane which is denoted by C_{20} is calculated:

$$C_{20} = \frac{1}{m_{20}}$$

$$= 1.083$$

Thus, to achieve the desired strain output, the desired input strain, x, is corrected to

$$x_{corrected} = 1.083x$$

To achieve the desired strain output, the corrected strain, $x_{corrected}$, is the value that is to be input into the control plant model which is represented by the 20 mm x 20 mm PDMS membrane and the linear actuator system. From the open-loop control system in Figure 49, the desired output strain, denoted as S_{20} is,

$$S_{20} = 0.923x_{corrected}$$

Following the same calculation procedure as the 20 mm x 20 mm PDMS membrane, the compensation factor for the 20mm × 20mm membrane with dividers is determined:

$$m_{20d} = 0.729$$

$$C_{20d} = \frac{1}{m_{20d}}$$

$$= 1.372$$

Thus, the corrected strain input into the control system which contains the 20 mm x 20 mm PDMS membrane with dividers and linear actuator is,

$$x_{corrected} = 1.372x$$

To achieve the desired strain output, the output strain S_{20d} is,

$$S_{20d} = 0.729x_{corrected}$$

10 mm x 10 mm compensation factor calculation:

$$m_{10} = 0.532$$

$$C_{10} = \frac{1}{m_{10}}$$

$$= 1.880$$

Thus, the corrected strain input into the control system which contains the 10 mm x 10 mm PDMS membrane and linear actuator is,

$$x_{corrected} = 1.880x$$

To achieve the desired strain output, the output strain S_{10} is,

$$S_{10} = 0.532x_{corrected}$$

The calculated value of the compensation factor for the 10 mm x 10 mm PDMS membrane suggests that a redesign of the membrane may be more desirable than employing such a large compensation

factor. Recommendations for further device development and improvements are discussed in the following chapter. Table 4 provides a summary of the calculated compensation factor values.

Table 4: Calculated compensation factor values

PDMS Membrane Type	Gradient value	Compensation Factor
20 mm x 20 mm	0.923	1.083
20 mm x 20 mm with dividers	0.729	1.372
10 mm x 10 mm	0.532	1.880

3.4 Finite Element Analysis

The comparison of FEA and experimental results in Figure 71, Figure 72 and Figure 73, reveals a notable difference in strain values between the FEA and the experiments. This comparison is summarised in Table 5. In this section, only comparison results of 2%, 15% and 30% induced strain are presented. The complete array of results of 2%, 5%, 10%, 15%, 20%, 25% and 30% induced strain is presented in Appendix B of section 6.2.

3.4.1 20 mm x 20 mm Membrane

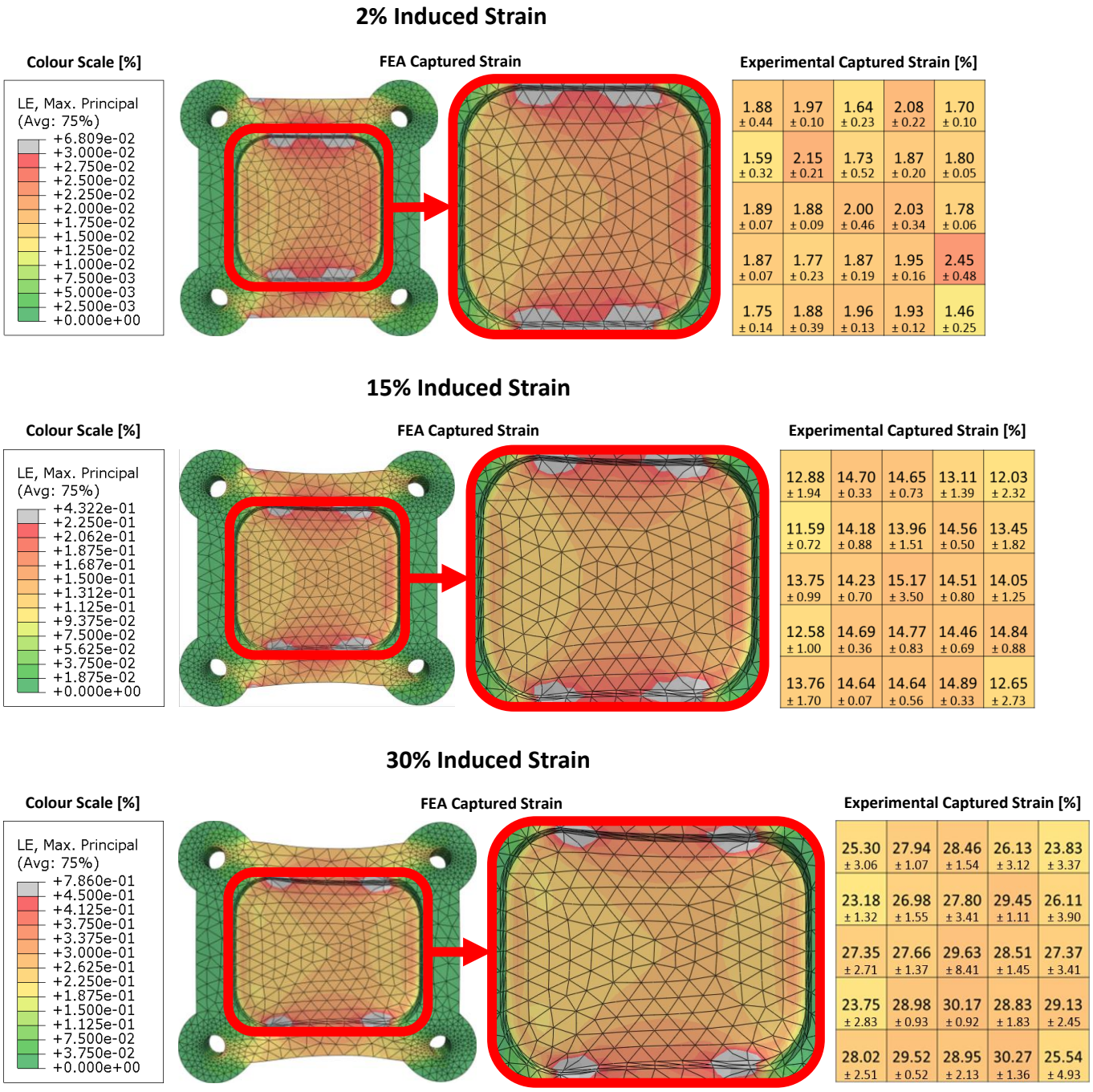

Figure 71: Comparison between FEA and practical experimentation of 20 mm x 20 mm membrane experiencing 2%, 15% and 30% induced strain

3.4.2 20 mm x 20 mm Membrane with Dividers

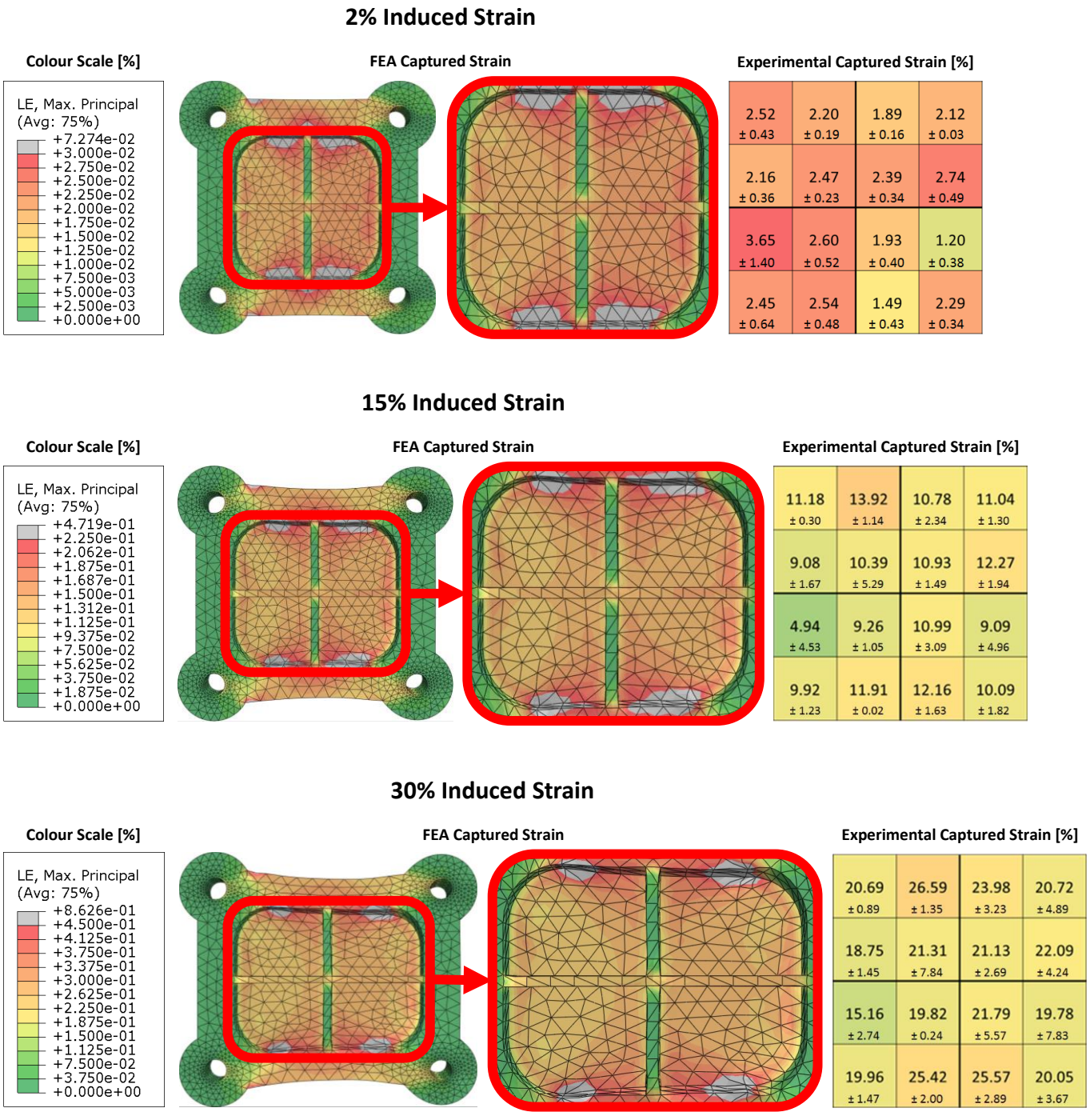

Figure 72: Comparison between FEA and practical experimentation of 20 mm x 20 mm membrane with dividers experiencing 2%, 15% and 30% induced strain

3.4.3 10 mm x 10 mm Membrane

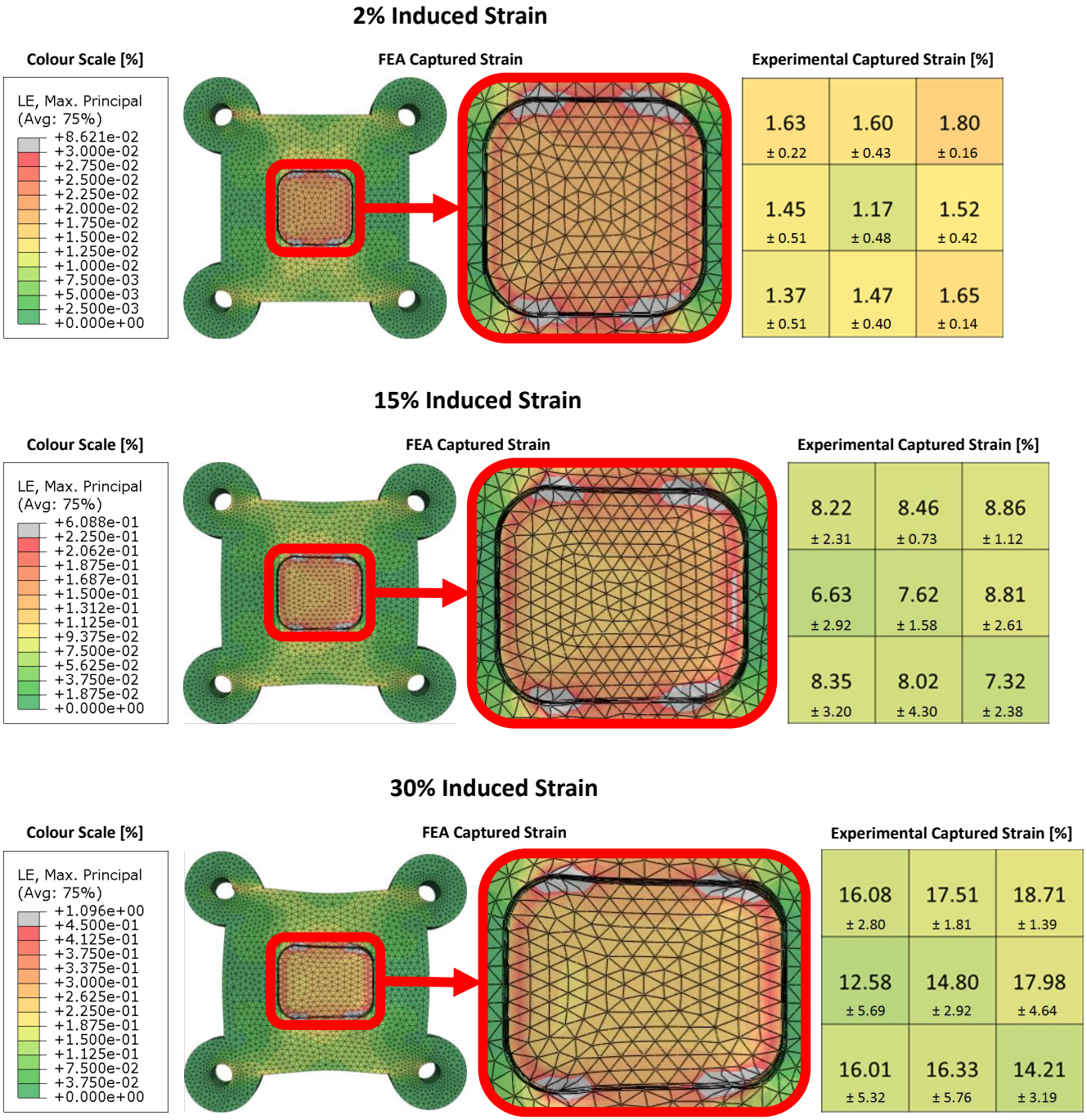

Figure 73: Comparison between FEA and practical experimentation of 10 mm x 10 mm membrane experiencing 2%, 15% and 30% induced strain

3.4.4 Discussion of Finite Element Models and Predictions

Table 5 shows the computational and experimental average strain output values of all PDMS membrane types at each induced strain. The average captured strain output of the FEA was calculated by averaging the node selection of the cell culture area of the model as seen in Figure 57.

Although the results between the two modes of investigation do not correspond, from the colour distribution of the following figures that display the results of the FEA and experimentation, Figure 71, Figure 72 and Figure 73, it can be seen that there is a correlation in relative strain distribution between the strain results of FEA and practical experimentation.

Table 5: Average strain output of computational models and experimental models of various types of PDMS membranes

Induced Strain [%]	**Average Strain Output [%]**					
	FEA PDMS Membrane Model			**Practical Experimentation Results**		
	20 mm x 20 mm	**20 mm x 20 mm with Dividers**	**10 mm x 10 mm**	**20 mm x 20 mm**	**20 mm x 20 mm with Dividers**	**10 mm x 10 mm**
2.00	2.10	2.15	2.06	1.87 ± 0.20	2.17 ± 0.55	1.52 ± 0.18
5.00	5.20	5.31	5.14	4.70 ± 0.32	4.40 ± 0.89	3.20 ± 0.29
10.00	10.16	10.38	10.09	9.33 ± 0.74	7.84 ± 0.86	5.57 ± 0.58
15.00	14.89	15.22	14.80	13.95 ± 0.97	10.85 ± 1.96	8.03 ± 0.73
20.00	19.41	19.83	19.29	18.53 ± 1.31	14.74 ± 1.76	10.53 ± 1.15
25.00	23.69	24.23	23.57	23.08 ± 1.62	18.17 ± 2.60	13.03 ± 1.44
30.00	27.82	28.45	27.73	27.55 ± 2.01	21.51 ± 2.87	16.02 ± 1.93

Using the data in Table 5, the absolute and relative difference between the FEA models and practical experimentation results were calculated and tabulated in Table 6. The relative difference in reference to the practical experimentation of Table 6 presents the percentage error for the ease of comparison between the FEA models and experimental results and is calculated by:

$$Relative\ difference = \frac{FEA\ experimentation\ -\ Practical\ experimentation}{Practical\ experimentation}$$

Table 6: Absolute and relative difference between FEA model and practical experimentation results

Induced Strain [%]	Absolute Difference between FEA Model and Practical Experimentation Results [% strain]			Relative Difference between FEA Model and Practical Experimentation Results [% difference]		
	20 mm x 20 mm	20 mm x 20 mm with Dividers	10 mm x 10 mm	20 mm x 20 mm	20 mm x 20 mm with Dividers	10 mm x 10 mm
2%	0.23	-0.01	0.54	12.2	-0.6	35.7
5%	0.49	0.91	1.95	10.5	20.8	60.9
10%	0.83	2.54	4.52	8.9	32.4	81.2
15%	0.94	4.36	6.77	6.8	40.2	84.3
20%	0.88	5.08	8.76	4.7	34.5	83.2
25%	0.60	6.07	10.54	2.6	33.4	80.9
30%	0.26	6.94	11.70	1.0	32.3	73.0

Table 5 indicates that for the 20 mm x 20 mm membranes, the FEA values correspond with experimental data. Table 6 illustrates that the absolute difference is less than 1% strain between the FEA and experimental results of the 20 mm x 20 mm PDMS membrane for all levels of induced strain. Thus, larger strains result in a smaller percentage error. The percentage error for the 20 mm x 20 mm PDMS membrane between the FEA and experimental results is low, thus validating the computational model of this membrane type.

In the models of the 20 mm x 20 mm PDMS membrane with dividers and 10 mm x 10 mm PDMS membrane, the differences between the FEA and experimental results is larger than that of the 20 mm x 20 mm membrane. It is observed in Table 6 that an increase in absolute difference leads to an increase in relative difference of the models of the 20 mm x 20 mm with dividers and 10 mm x 10 mm with the increase in induced strain; whereas the models of the 20 mm x 20 mm without the dividers demonstrate a constant absolute difference which leads to a decreasing relative difference between FEA and experimentation with the increase in induced strain.

From the Table 6, it can be deduced that agreements between the FEA and experimental models of the 20 mm x 20 mm with dividers and 10 mm x 10 mm requires improvements, as they show high values in relative difference. As mentioned in 3.3.1, by improving the attachment between the device to the membrane, the experimental accuracy will improve. Further, numerical model revisions may also need to be explored. Due to the device-membrane attachment problems with the experimental model of the 10 mm x 10 mm PDMS membrane as mentioned above, the computational model validation process was not conclusive as the incorrect attachment technique was not represented in the current FEA models.

4 Conclusion and Recommendations

4.1 Conclusion

From the analysis and discussion of the results, the designed device satisfies the objectives of this project of:

1. Developing a device and fixtures required for the three different load types: tension, compression and shear.

2. Manufacturing and assembly of the device.

3. Performing tension load experiments with live microscopy imaging.

4. Characterising the strain fields on the PDMS membranes with non-biological markers.

5. Generation of FEA computational models of the different types of PDMS membranes.

Strain uniformity was present in all three types of PDMS membrane types. The device was most successful with the 20 mm x 20 mm PDMS membrane type. From the analysis of the experimentation, the 20 mm x 20 mm PDMS membrane type showed close correlation to the ideal strain output. But, in the instance of the 10 mm x 10 mm PDMS membrane, to obtain a desirable strain output, the clamping mechanism is required to be improved.

From the analysis procedure of the practical experimentation results, the 20 mm x 20 mm PDMS membrane results demonstrates effective clamping which resulted in the FEA simulation matching the experimentation results. The 10 mm x 10 mm PDMS membrane presented with less effective clamping which resulted in the non-correlating results of FEA.

The variabilities of the clamping of the PDMS membranes were not simulated in the FEA software, therefore the FEA results did not match the practical experimentation results. The major reason for the discrepancy in strain data results between the two modes of FEA and experimentation is the effectiveness of clamping. The FEA models were input with boundary conditions that clamped the PDMS membrane effectively, whilst in the experimentation, it was discovered that the PDMS membrane was not clamped effectively due to the weak point in the design. The FEA models would most probably match the practical experimentation results once the clamping technique of the PDMS substrate is improved of the device.

4.2 Recommendations

As discussed in Section 3.3, the effectiveness of the device-membrane system can be improved by adjusting the clamping mechanism. During the tightening of the nut, there is no even compression of the substrate which causes the clamp to tilt. The tilting of the clamp causes the grappling part of the clamp to only partially grapple the edge of the PDMS membrane as seen in Figure 68. It is suggested to lock the nut to the certain height position till it cannot tighten any further. Other suggestions included larger washers to distribute the area of compression evenly along the PDMS membrane during the tightening of the nut.

A redesign of the 10 mm x 10 mm PDMS membrane is recommended to reduce the material amount of the walls. By reducing the material amount of the walls of the PDMS membrane, more strain energy is focused on the 10 mm x 10 mm cell culture area. Thus, the strain output should match the intended strain input value. It is recommended that the redesign be similar to the 20 mm x 20 mm membrane and scaled down by a factor of 2. A redesign of the 10 mm x 10 mm membrane would also require a redesign of **Tension Module A** and **Tension Module B** of the tension loading system of the device, displayed in Figure 29.

To obtain more accurate FEA simulations, more data to describe the PDMS material are required. This requires different types of mechanical characterisation of the material. These different types of experiments include: planar tension tests, uniaxial compression tests, equibiaxial tension tests and confined compression tests. Ideally, various forms of testing rigs are essential to conduct accurate testing. In the scope of this project the various tests were not conducted as the equipment necessary was unavailable. Additional data information enables more complex hyperelastic material models to be selected.

By introducing a control feedback system, the need for a fixed compensation factor is eliminated as the controller will adjust the linear actuator system until the desired strain Is reached. A strain feedback system requires the addition of electrical system design components and incorporates software imaging methods to detect cellular shapes and obtain its strain characteristics. This feedback back control system is illustrated in Figure 74. The imaging system detects the difference between the strain output and user input. If a difference is detected the linear motor will actuate to accommodate the differences.

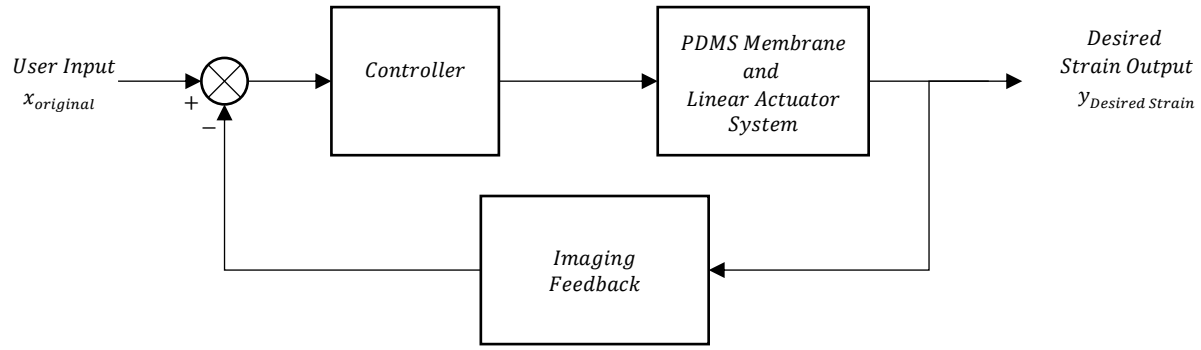

Figure 74: Recommended closed-loop control system

With the current membrane thickness of 1 mm, the maximum possible magnification possible in inverted microscope is 10x. To achieve higher magnifications with inverted microscopes, the Microscopy Division of UCT recommends reducing the thickness of the PDMS membranes to a similar

thickness of that of the typical coverslip. Typical biological microscope objectives are designed for the use of 0.17mm coverslips which have a low refractive index. By reducing the thickness of the membrane, the refractivity from the microscope light source is decreased. By reducing the refractive index, it allows for higher strength objectives to function with the PDMS membranes and to obtain clearer details of the cell itself and its activities. This decrease to the thickness of the PDMS membranes requires assessment in terms of sufficient structural integrity for the loading/stretching, and feasibility of moulding technique.

Currently the device is limited to the use for inverted microscopes. The designed device is compatible with the Zeiss Axiovert 200M, an inverted fluorescence microscope and the Zeiss LSM 510 confocal microscope. Further design is required for the compatibility of upright microscopy.

5 References

Ahearne, M., Y. Yang and K.-K. Liu (2008). "Mechanical Characterisation of Hydrogels for Tissue Engineering Applications." Topics in Tissue Engineering **4**.

Anseth, K. S., C. N. Bowman and L. Brannon-Peppas (1996). "Mechanical properties of hydrogels and their experimental determination." Biomaterials **17**(17): 1647-1657.

Banes, A. J., J. Gilbert, D. Taylor and O. Monbureau (1985). "A new vacuum-operated stress-providing instrument that applies static or variable duration cyclic tension or compression to cells in vitro." Journal of Cell Science(75): 35-42.

Bausch, A. R. and K. Kroy (2006). "A bottom-up approach to cell mechanics." Nature Physics **2**(4): 231-238.

Bonakdar, N., J. Luczak, L. Lautscham, M. Czonstke, T. M. Koch, A. Mainka, T. Jungbauer, W. H. Goldmann, R. Schroder and B. Fabry (2012). "Biomechanical characterization of a desminopathy in primary human myoblasts." Biochem Biophys Res Commun **419**(4): 703-7.

Brazil, D. P. and B. A. Hemmings (2001). "Ten years of protein kinase B signalling: a hard Akt to follow." TRENDS in Biochemical Sciences **26**(11): 657 - 664.

Brown, Keiko Ookawa and J. Y. Wong (2005). "Evaluation of polydimethylsiloxane scaffolds with physiologically-relevant elastic moduli: interplay of substrate mechanics and surface chemistry effects on vascular smooth muscle cell response." Biomaterials **26**(16): 3123-9.

Chien, S. (2007). "Mechanotransduction and endothelial cell homeostasis: the wisdom of the cell." Am J Physiol Heart Circ Physiol **292**(3): H1209-24.

Chiu, J. J. and S. Chien (2011). "Effects of disturbed flow on vascular endothelium: pathophysiological basis and clinical perspectives." Physiol Rev **91**(1): 327-87.

Dalrymple, T., J. Choi and K. Miller (2007). Elastomer Rate-dependence: A Testing and Material Modeling Methodology. The Fall 172nd Technical Meeting of the Rubber Division of the American Chemical Society, Inc. Cleveland, OH.

Diani, J., B. Fayolle and P. Gilormini (2009). "A review on the Mullins effect." European Polymer Journal **45**(3): 601-612.

Faust, U., N. Hampe, W. Rubner, N. Kirchgessner, S. Safran, B. Hoffmann and R. Merkel (2011). "Cyclic stress at mHz frequencies aligns fibroblasts in direction of zero strain." PLoS One **6**(12): e28963.

Griffith, L. G. (2002). "Emerging Design Principles in Biomaterials and Scaffolds for Tissue Engineering." Annals of the New York Academy of Sciences **961**: 83-95.

Hoh, J. H. and P. K. Hansma (1992). "Atomic force microscopy for high-resolution imaging in cell biology." Trends in Cell Biology **2**(7): 208-213.

Jacobs, C. R., H. Huang and R. Y. Kwon (2012). Introduction to Cell Mechanics and Mechanobiology, Garland Science.

Janmey, P. A. and C. A. McCulloch (2007). "Cell mechanics: integrating cell responses to mechanical stimuli." Annu Rev Biomed Eng **9**: 1-34.

Johnston, I. D., D. K. McCluskey, C. K. L. Tan and M. C. Tracey (2014). "Mechanical characterization of bulk Sylgard 184 for microfluidics and microengineering." Journal of Micromechanics and Microengineering **24**(3): 035017.

Kamble, H., M. J. Barton, M. Jun, S. Park and N. T. Nguyen (2016). "Cell stretching devices as research tools: engineering and biological considerations." Lab Chip.

Khanafer, K., A. Duprey, M. Schlicht and R. Berguer (2009). "Effects of strain rate, mixing ratio, and stress-strain definition on the mechanical behavior of the polydimethylsiloxane (PDMS) material as related to its biological applications." Biomed Microdevices **11**(2): 503-8.

Kim, B., S. B. Lee, J. Lee, S. Cho, H. Park, S. Yeom and S. H. Park (2012). "A comparison among Neo-Hookean model, Mooney-Rivlin model, and Ogden model for chloroprene rubber." International Journal of Precision Engineering and Manufacturing **13**(5): 759-764.

Kim, T. K., J. K. Kim and O. C. Jeong (2011). "Measurement of nonlinear mechanical properties of PDMS elastomer." Microelectronic Engineering **88**(8): 1982-1985.
Kohn, J. C., D. W. Zhou, F. Bordeleau, A. L. Zhou, B. N. Mason, M. J. Mitchell, M. R. King and C. A. Reinhart-King (2015). "Cooperative effects of matrix stiffness and fluid shear stress on endothelial cell behavior." Biophys J **108**(3): 471-8.
Konstantopoulos., K., S. Kukreti. and L. V. McIntire. (1998). "Biomechanics of cell interactions in shear fields." Advanced Drug Delivery Reviews **3**(33): 141-164.
Krishnan, R., C. Y. Park, Y. C. Lin, J. Mead, R. T. Jaspers, X. Trepat, G. Lenormand, D. Tambe, A. V. Smolensky, A. H. Knoll, J. P. Butler and J. J. Fredberg (2009). "Reinforcement versus fluidization in cytoskeletal mechanoresponsiveness." PLoS One **4**(5): e5486.
Li, S. T., Y. Liu, Q. Zhou, R. F. Lue, L. Song, S. W. Dong, P. Guo and B. Kopjar (2014). "A novel axial-stress bioreactor system combined with a substance exchanger for tissue engineering of 3D constructs." Tissue Eng Part C Methods **20**(3): 205-14.
Liu, M., J. Sun and Q. Chen (2009). "Influences of heating temperature on mechanical properties of polydimethylsiloxane." Sensors and Actuators A: Physical **151**(1): 42-45.
Mann, J. M., R. H. Lam, S. Weng, Y. Sun and J. Fu (2012). "A silicone-based stretchable micropost array membrane for monitoring live-cell subcellular cytoskeletal response." Lab Chip **12**(4): 731-40.
MSC.SoftwareCorporation (2010). Nonlinear Finite Element Analysis of Elastomers.
Mullins, L. (1969). "Softening of Rubber by Deformation." Rubber Chemistry and Technology **42**(1): 339-362.
Naruse, K., T. Yamada and M. Sokabe (1998). "Involvement of SA channels in orienting response of cultured endothelial cells to cyclic stretch." The American journal of physiology **274**: H1532-H1538.
Neuman, K. C. and A. Nagy (2008). "Single-molecule force spectroscopy: optical tweezers, magnetic tweezers and atomic force microscopy." Nat Methods **5**(6): 491-505.
Normand, V., D. L. Lootens, E. Amici, K. P. Plucknett and P. Aymard (2000). "New Insight into Agarose Gel Mechanical Properties." Biomacromolecules **1**(4): 730-738.
OLYMPUS. (2012). "Comparing Confocal and Widefield Fluorescence Microscopy." Microscopy Resource Center Retrieved 29 August, 2016, from http://www.olympusmicro.com/primer/java/confocalvswidefield/index.html.
Oyen, M. L. (2013). "Mechanical characterisation of hydrogel materials." International Materials Reviews **59**(1): 44-59.
Peeters, E. A., C. W. Oomens, C. V. Bouten, D. L. Bader and F. P. Baaijens (2005). "Mechanical and failure properties of single attached cells under compression." J Biomech **38**(8): 1685-93.
Peeters, E. A. G., C. V. C. Bouten, C. W. J. Oomens and F. P. T. Baaijens (2003). "Monitoring the biomechanical response of individual cells under compression: A new compression device." Medical and Biological Engineering and Computing **41**(4): 498-503.
PhysicsCentral. (2016). "Optical Tweezers." Retrieved Seprember, 2016, from http://physicscentral.com/explore/action/tweezers.cfm.
Qu, H. and P. Gao (2010). "The effect of square wave stretching on proliferation of lung adenocarcinoma cells and squamous carcinoma of tongue cells." Proceedings - 2010 3rd International Conference on Biomedical Engineering and Informatics, BMEI 2010 **5**(Bmei): 2122-2124.
Rheosys. (2011). "A Basic Introduction to Viscometers & Viscometry." Retrieved 02 February, 2017.
Robert J. Pelham Jr. and Y.-L. Wang (1997). "Cell locomotion and focal adhesions are regulated by substrate flexibility." Cell Biology **94**: 13661-13665.
Roos, W. H. (2011). How to Perform a Nanoindentation Experiment on a Virus. Single Molecule Analysis: Methods and Protocols. E. J. G. Peterman and G. J. L. Wuite. Totowa, NJ, Humana Press**:** 251-264.
Schneider, F., T. Fellner, J. Wilde and U. Wallrabe (2008). "Mechanical properties of silicones for MEMS." Journal of Micromechanics and Microengineering **18**(6): 065008.

Seliktar, D. (2012). "Designing Cell-Compatible Hydrogels for Biomedical Applications." Science.

Semwogerere, D. and E. R. Weeks (2005). "Confocal Microscopy." Encyclopedia of Biomaterials and Biomedical Engineering: 1–10.

Shao, Y., X. Tan, R. Novitski, M. Muqaddam, P. List, L. Williamson, J. Fu and A. P. Liu (2013). "Uniaxial cell stretching device for live-cell imaging of mechanosensitive cellular functions." Rev Sci Instrum **84**(11): 114304.

Sophie L. Peterson, Anthony McDonald, Paul L. Gourley and D. Y. Sasaki (2004). "Poly(dimethylsiloxane) thin films as biocompatible coatings for microfluidic devices: Cell culture and flow studies with glial cells." Journal of Biomedical Materials Research **72A**(1): 10-18.

Strex. (2017). "Cell Stretching System." Retrieved 10 December 2017, 2017, from https://strexcell.com/cell-stretching-system/stretch-patterns/.

Surekha. (2016). "Human Cell – Properties, Diagram, Parts, Pictures, Structure." DISEASES PICTURES Retrieved 10 December 2017, 2017, from http://diseasespictures.com/human-cell-functions-diagram-parts-pictures-structure/.

Takeda, H., K. Komori, N. Nishikimi, Y. Nimura, M. Sokabe and K. Naruse (2006). "Bi-phasic activation of eNOS in response to uni-axial cyclic stretch is mediated by differential mechanisms in BAECs." Life Sci **79**(3): 233-9.

Tamiello, C., A. B. Buskermolen, F. P. Baaijens, J. L. Broers and C. V. Bouten (2016). "Heading in the Right Direction: Understanding Cellular Orientation Responses to Complex Biophysical Environments." Cell Mol Bioeng **9**: 12-37.

Thangawng, A. L., R. S. Ruoff, M. A. Swartz and M. R. Glucksberg (2007). "An ultra-thin PDMS membrane as a bio/micro–nano interface: fabrication and characterization." Biomed Microdevices.

Tremblay, D., S. Chagnon-Lessard, M. Mirzaei, A. E. Pelling and M. Godin (2014). "A microscale anisotropic biaxial cell stretching device for applications in mechanobiology." Biotechnol Lett **36**(3): 657-65.

Unal, M., Y. Alapan, H. Jia, A. G. Varga, K. Angelino, M. Aslan, I. Sayin, C. Han, Y. Jiang, Z. Zhang and U. A. Gurkan (2014). "Micro and Nano-scale Technologies for Cell Mechanics." Nanobiomedicine: 1.

Ursekar, C. P., S. K. Teo, H. Hirata, I. Harada, K. H. Chiam and Y. Sawada (2014). "Design and construction of an equibiaxial cell stretching system that is improved for biochemical analysis." PLoS One **9**(3): e90665.

Wu, H. W., T. Kuhn and V. T. Moy (1998). "Mechanical properties of L929 cells measured by atomic force microscopy: effects of anticytoskeletal drugs and membrane crosslinking." Scanning **20**(5): 389-397.

6 Appendix

6.1 Appendix A – Microscope Captured Images of Practical Experimentation

6.1.1 20 mm x 20 mm PDMS Membrane

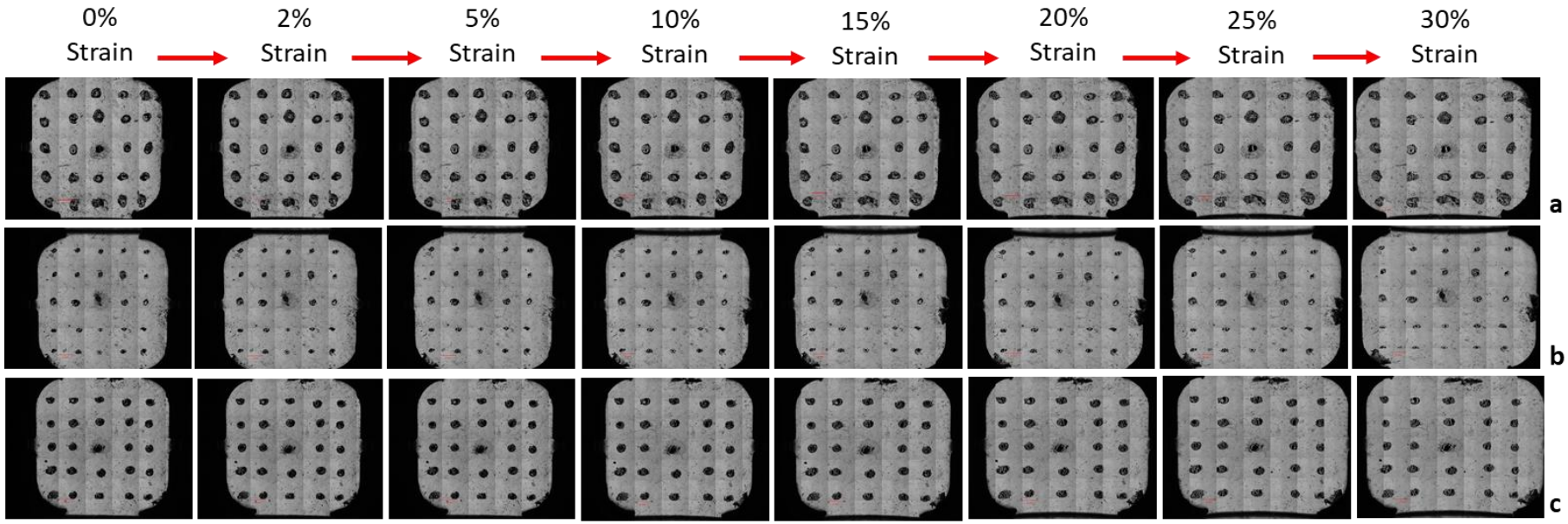

Figure 75: Captured images of 20 mm x 20 mm PDMS membrane with 5 x 5 matrix of non-biological markers at 0%, 2%, 5%, 10%, 15%, 20%, 25% and 30% strain of: (a) Specimen 1, (b) Specimen 2 and (c) Specimen 3

6.1.2 20 mm x 20 mm PDMS Membrane with Dividers

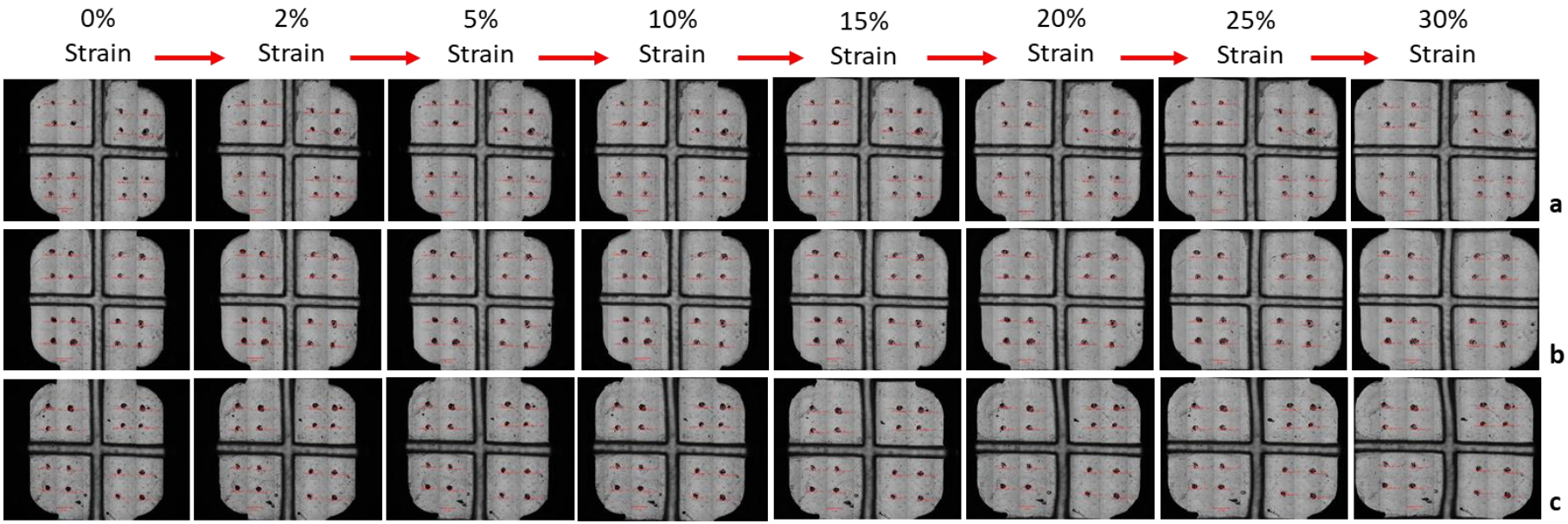

Figure 76: Captured images of 20 mm x 20 mm PDMS membrane with dividers with 2 x 2 matrix of non-biological markers in each quadrant at 0%, 2%, 5%, 10%, 15%, 20%, 25% and 30% strain of: (a) Specimen 1, (b) Specimen 2 and (c) Specimen 3

6.1.3 10 mm x 10 mm PDMS Membrane

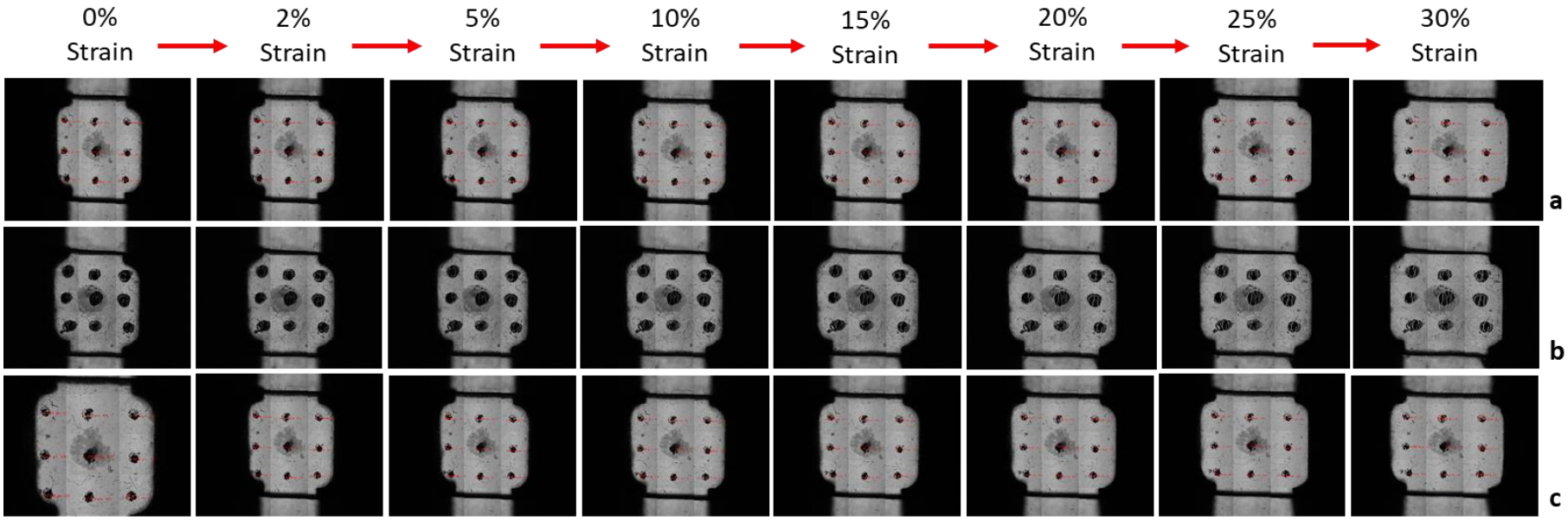

Figure 77: Captured images of 10 mm x 10 mm PDMS membrane with 3 x 3 matrix of non-biological markers at 0%, 2%, 5%, 10%, 15%, 20%, 25% and 30% strain of: (a) Specimen 1, (b) Specimen 2 and (c) Specimen 3

6.2 Appendix B – Comparative Results between FEA and Experimentation

6.2.1 20 mm x 20 mm PDMS Membrane

2% Induced Strain

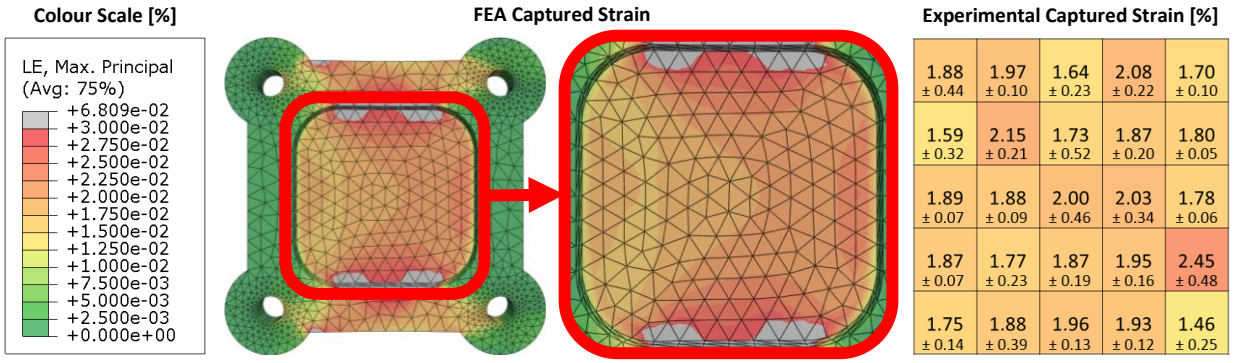

Figure 78: Comparison between FEA and practical experimentation of 20 mm x 20 mm membrane experiencing 2% induced strain

5% Induced Strain

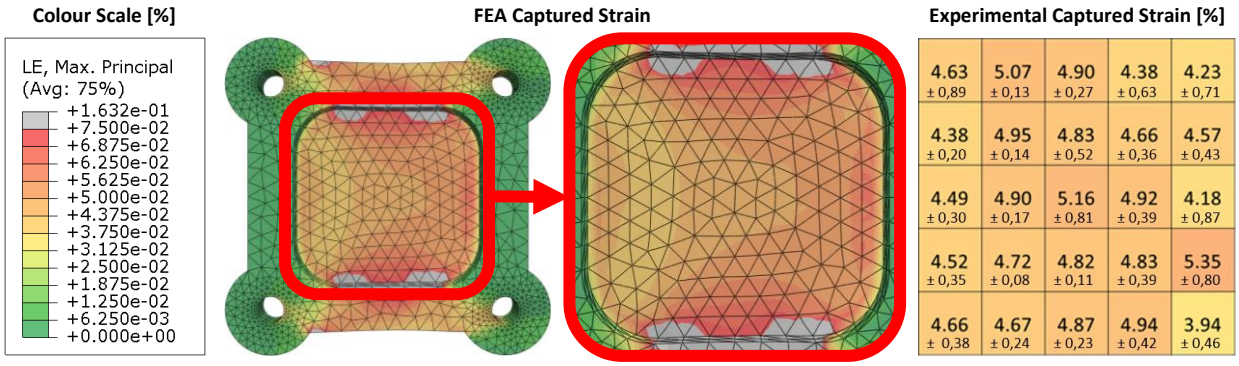

Figure 79: Comparison between FEA and practical experimentation of 20 mm x 20 mm membrane experiencing 5% induced strain

10% Induced Strain

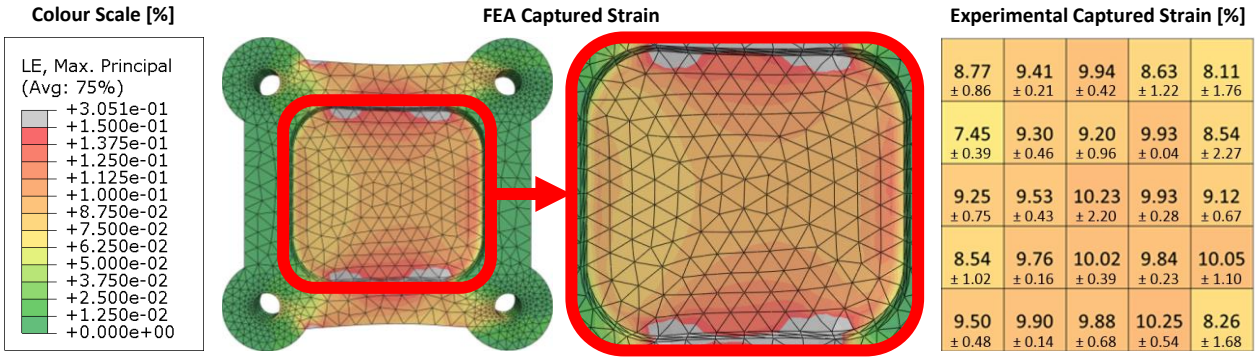

Figure 80: Comparison between FEA and practical experimentation of 20 mm x 20 mm membrane experiencing 10% induced strain

15% Induced Strain

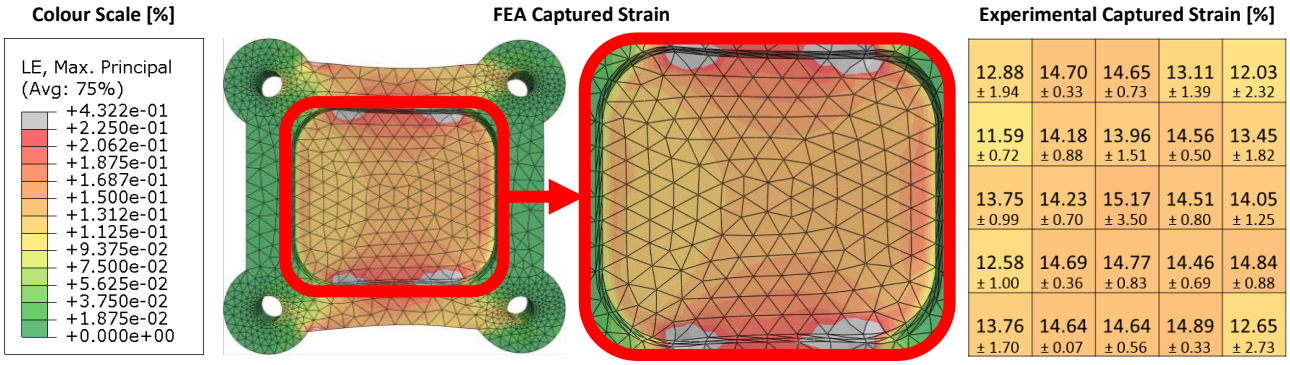

Figure 81: Comparison between FEA and practical experimentation of 20 mm x 20 mm membrane experiencing 15% induced strain

20% Induced Strain

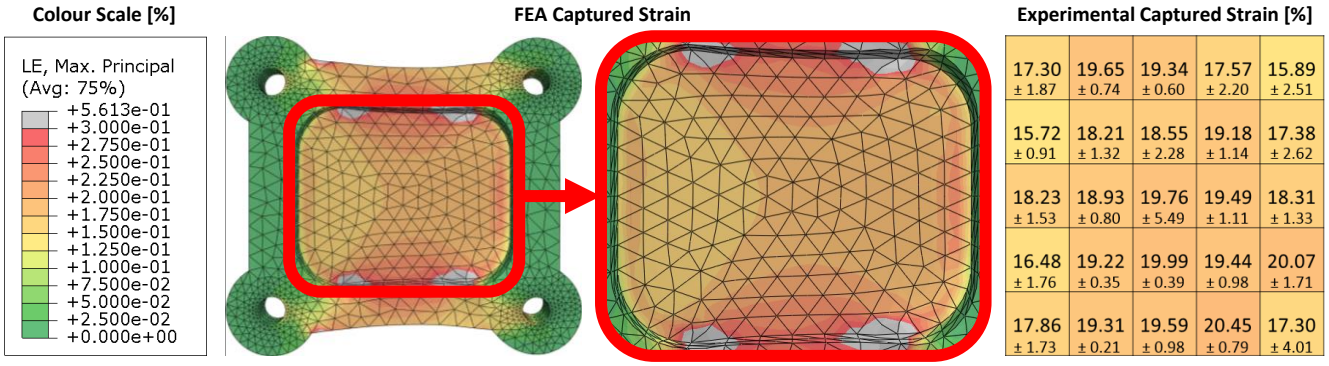

Figure 82: Comparison between FEA and practical experimentation of 20 mm x 20 mm membrane experiencing 20% induced strain

25% Induced Strain

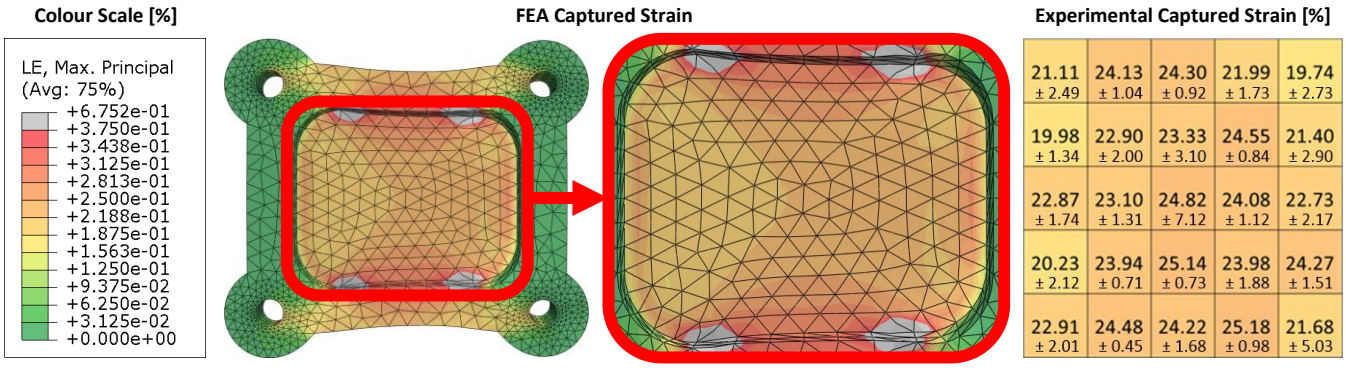

Figure 83: Comparison between FEA and practical experimentation of 20 mm x 20 mm membrane experiencing 25% induced strain

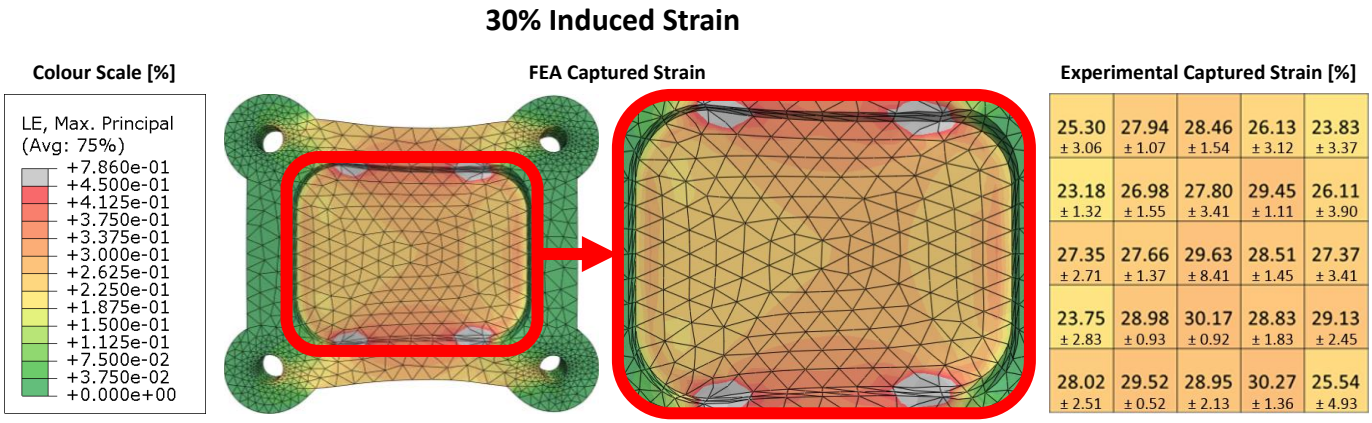

Figure 84: Comparison between FEA and practical experimentation of 20 mm x 20 mm membrane experiencing 30% induced strain

6.2.2 20 mm x 20 mm PDMS Membrane with Dividers

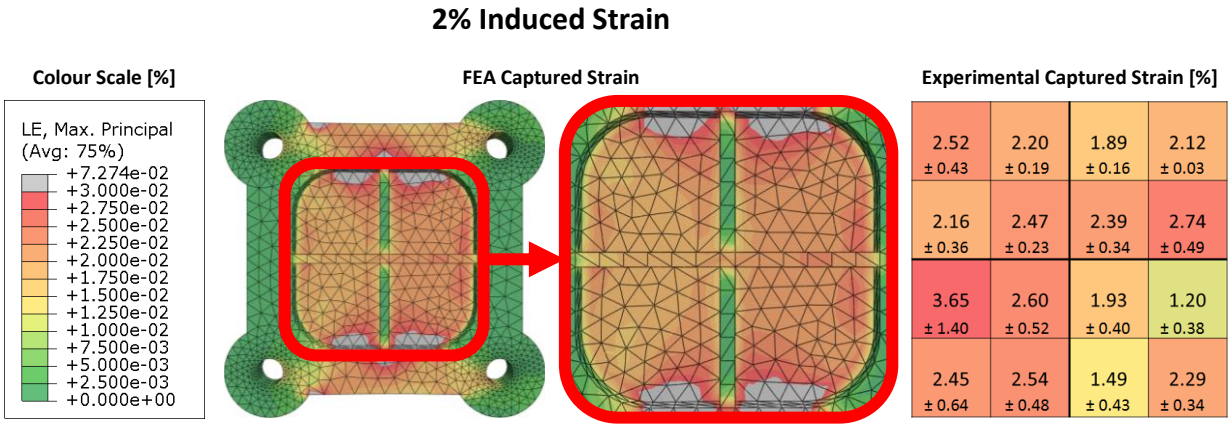

Figure 85: Comparison between FEA and practical experimentation of 20 mm x 20 mm membrane with dividers experiencing 2% induced strain

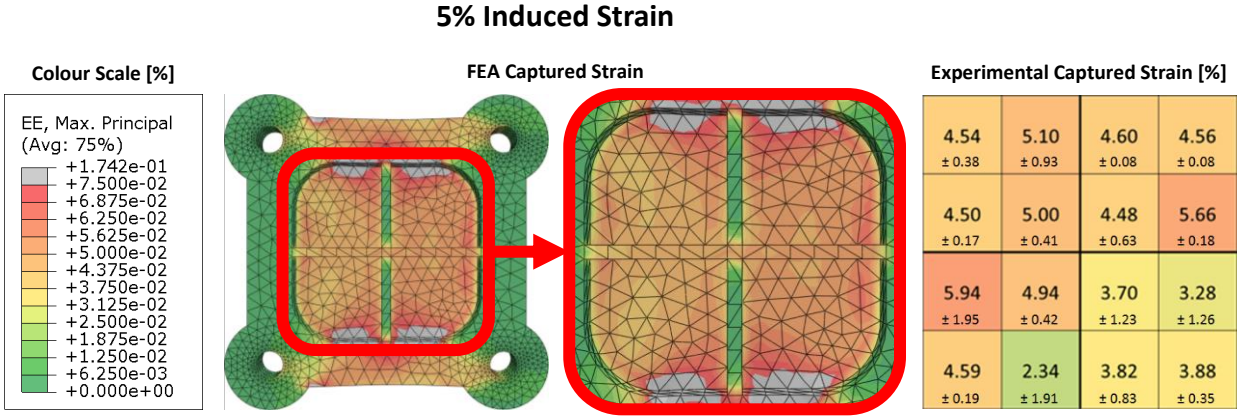

Figure 86: Comparison between FEA and practical experimentation of 20 mm x 20 mm membrane with dividers experiencing 5% induced strain

10% Induced Strain

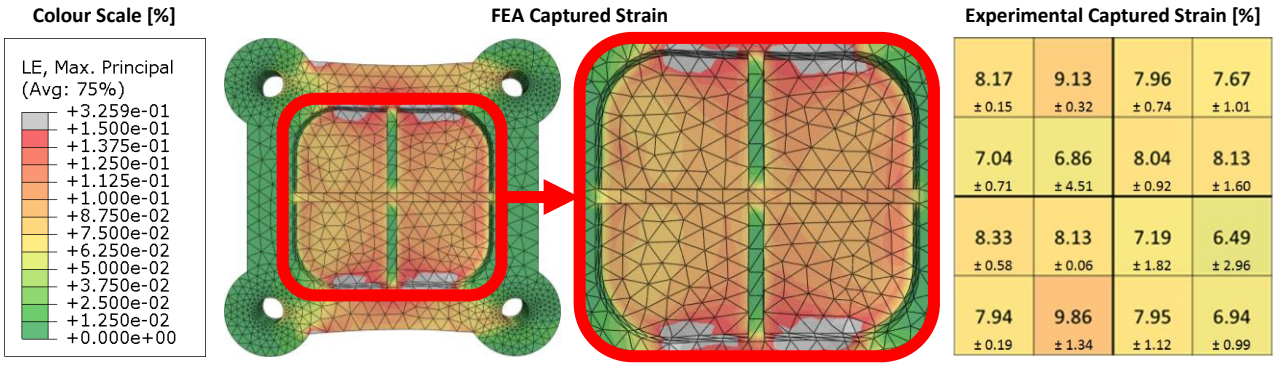

Figure 87: Comparison between FEA and practical experimentation of 20 mm x 20 mm membrane with dividers experiencing 10% induced strain

15% Induced Strain

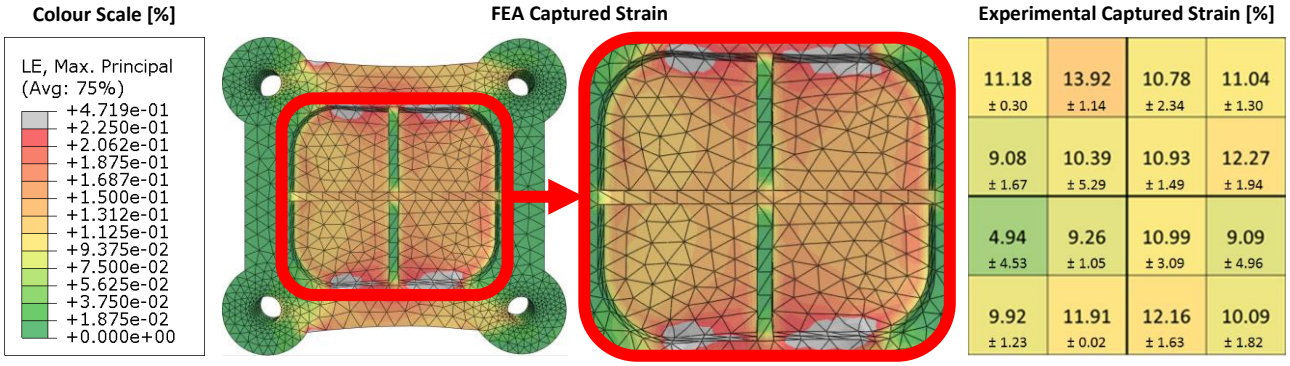

Figure 88: Comparison between FEA and practical experimentation of 20 mm x 20 mm membrane with dividers experiencing 15% induced strain

20% Induced Strain

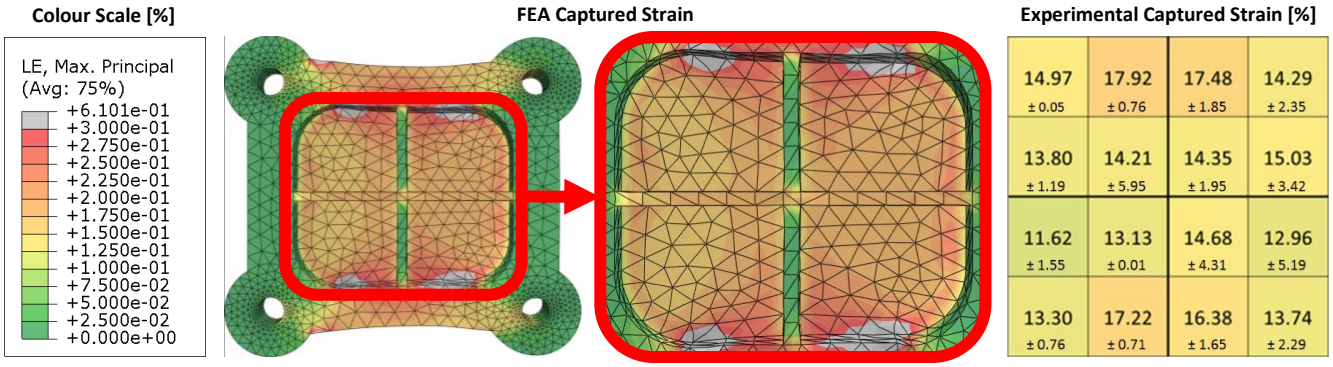

Figure 89: Comparison between FEA and practical experimentation of 20 mm x 20 mm membrane with dividers experiencing 20% induced strain

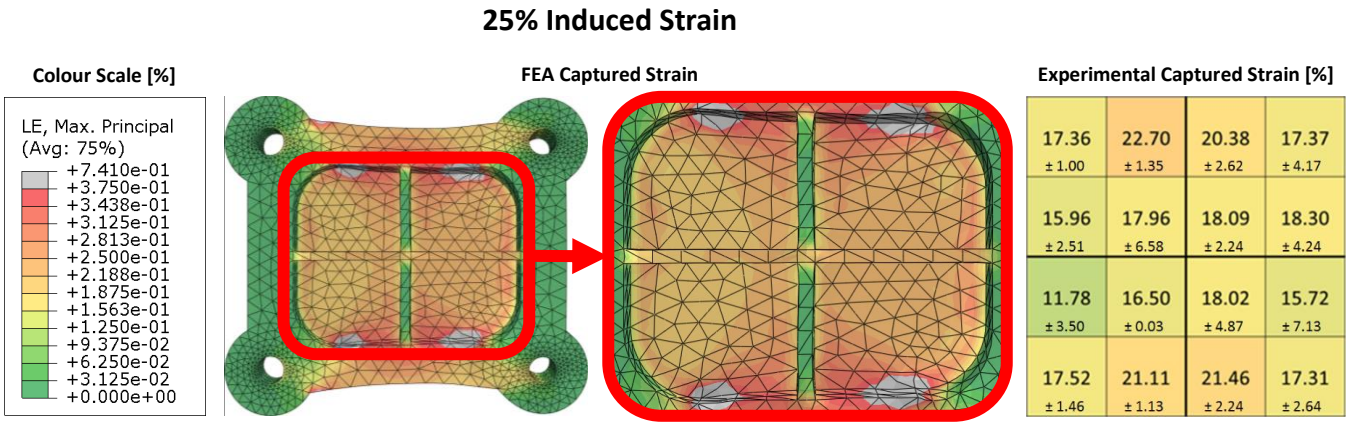

Figure 90: Comparison between FEA and practical experimentation of 20 mm x 20 mm membrane with dividers experiencing 25% induced strain

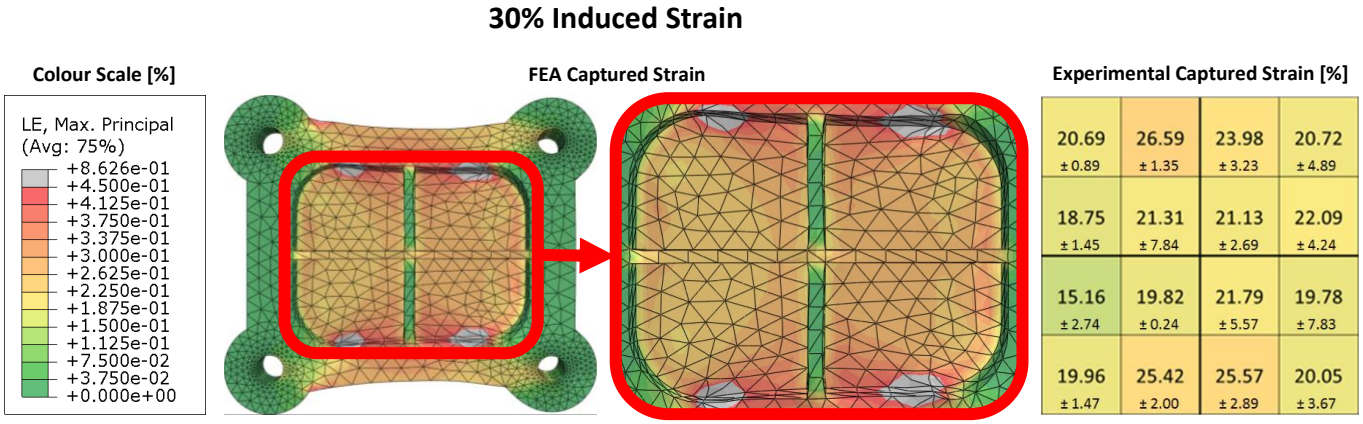

Figure 91: Comparison between FEA and practical experimentation of 20 mm x 20 mm membrane with dividers experiencing 30% induced strain

6.2.3 10 mm x 10 mm PDMS Membrane

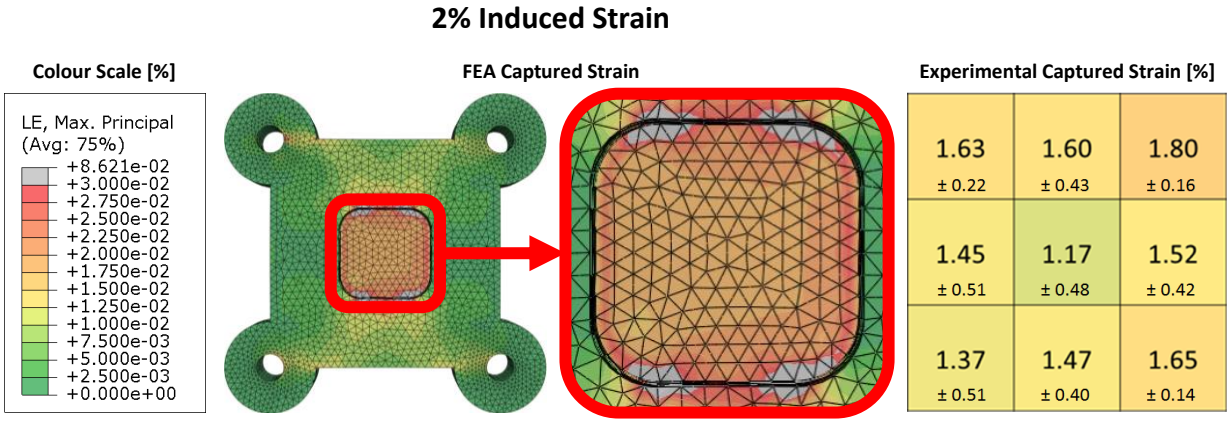

Figure 92: Comparison between FEA and practical experimentation of 10 mm x 10 mm membrane experiencing 2% induced strain

5% Induced Strain

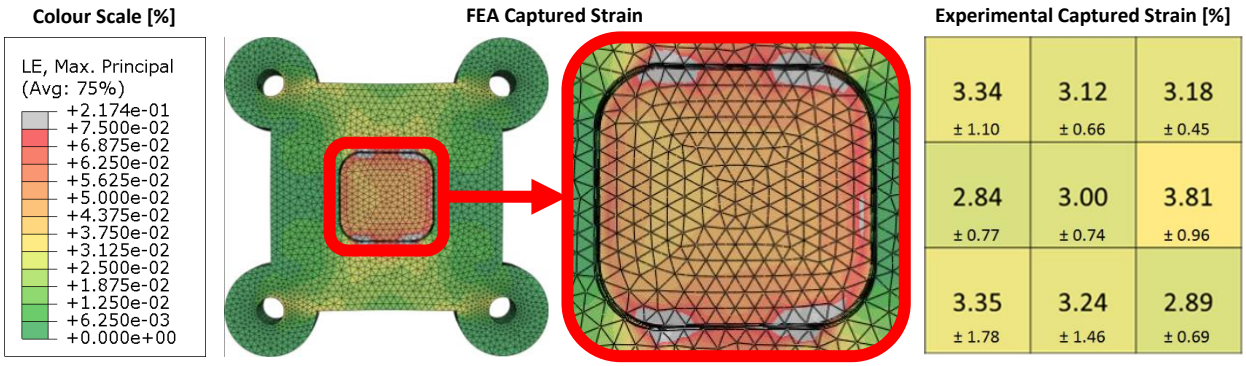

Figure 93: Comparison between FEA and practical experimentation of 10 mm x 10 mm membrane experiencing 5% induced strain

10% Induced Strain

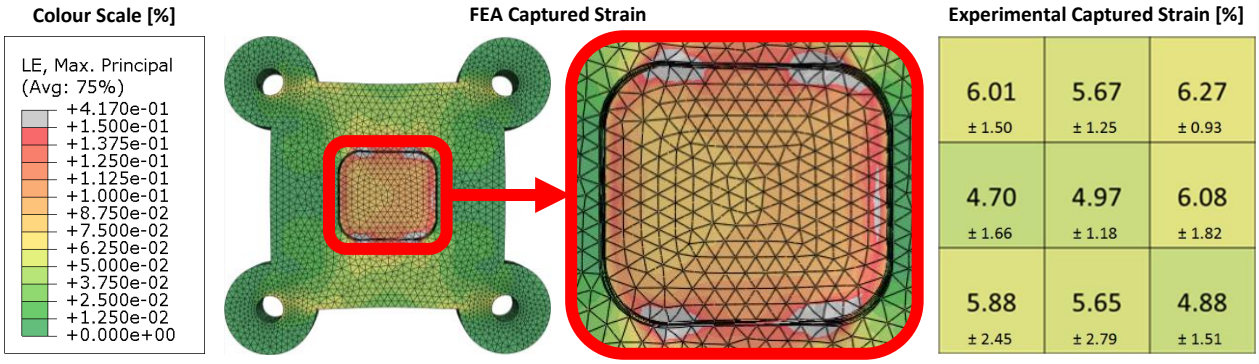

Figure 94: Comparison between FEA and practical experimentation of 10 mm x 10 mm membrane experiencing 10% induced strain

15% Induced Strain

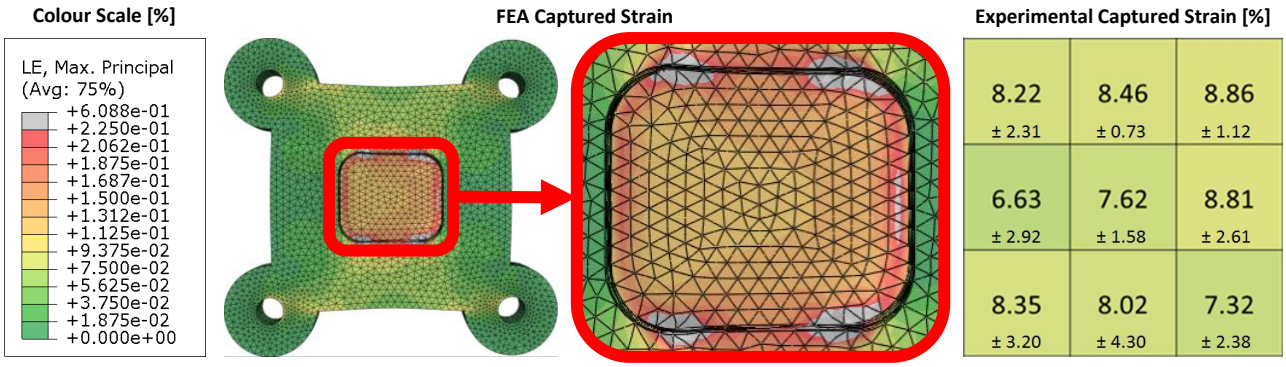

Figure 95: Comparison between FEA and practical experimentation of 10 mm x 10 mm membrane experiencing 15% induced strain

20% Induced Strain

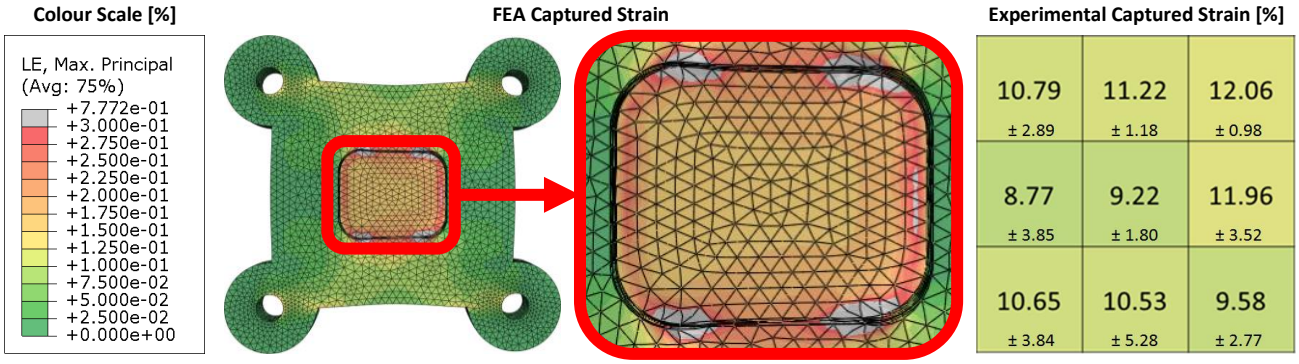

Figure 96: Comparison between FEA and practical experimentation of 10 mm x 10 mm membrane experiencing 20% induced strain

25% Induced Strain

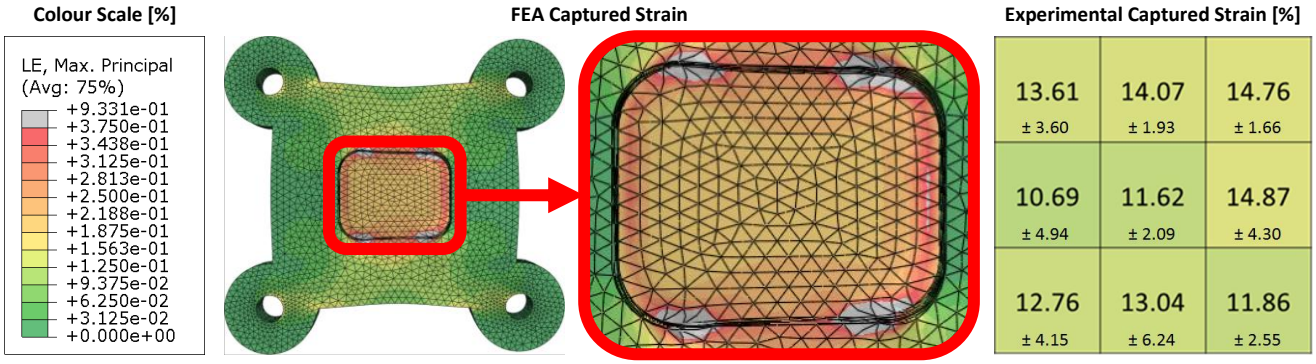

Figure 97: Comparison between FEA and practical experimentation of 10 mm x 10 mm membrane experiencing 25% induced strain

30% Induced Strain

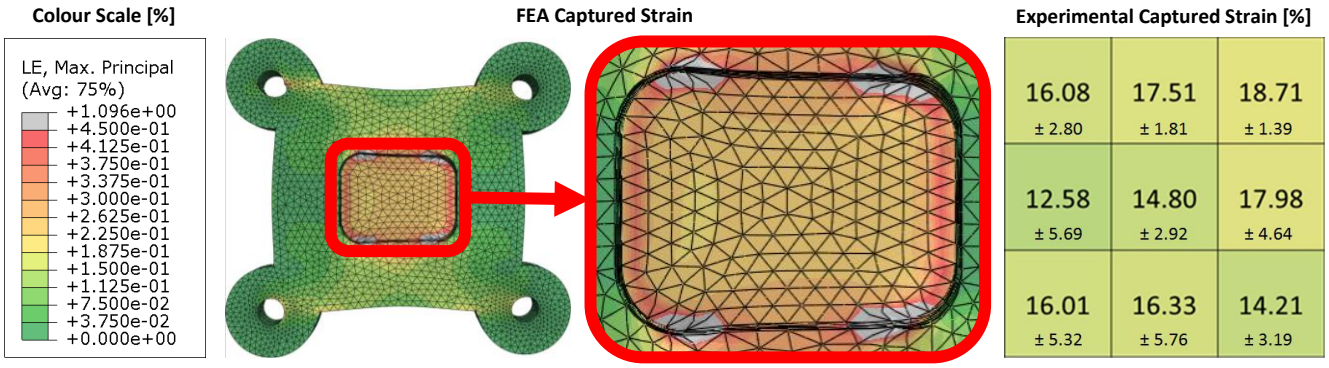

Figure 98: Comparison between FEA and practical experimentation of 10 mm x 10 mm membrane experiencing 30% induced strain